

INFORMATION TO USERS

This manuscript has been reproduced from the microfilm master. UMI films the text directly from the original or copy submitted. Thus, some thesis and dissertation copies are in typewriter face, while others may be from any type of computer printer.

The quality of this reproduction is dependent upon the quality of the copy submitted. Broken or indistinct print, colored or poor quality illustrations and photographs, print bleedthrough, substandard margins, and improper alignment can adversely affect reproduction.

In the unlikely event that the author did not send UMI a complete manuscript and there are missing pages, these will be noted. Also, if unauthorized copyright material had to be removed, a note will indicate the deletion.

Oversize materials (e.g., maps, drawings, charts) are reproduced by sectioning the original, beginning at the upper left-hand corner and continuing from left to right in equal sections with small overlaps.

ProQuest Information and Learning
300 North Zeeb Road, Ann Arbor, MI 48106-1346 USA
800-521-0600



**Ductile Fracture Mechanics: Modeling, Experiments,
and Computational Simulation**

By:

TONYA LYNN EMERSON
B.S. (California Polytechnic State University, San Luis Obispo, 1991)
M.S. (Stanford University, 1993)

DISSERTATION

Submitted in the partial satisfaction of the requirements for the degree of

DOCTORATE OF PHILOSOPHY

in

Civil and Environmental Engineering

in the

OFFICE OF GRADUATE STUDIES

of the

UNIVERSITY OF CALIFORNIA

DAVIS

Approved:

Mark M. Rall
Michael Kip
John Blodden

Committee in Charge
2002

UMI Number: 3065238



UMI Microform 3065238

Copyright 2002 by ProQuest Information and Learning Company.
All rights reserved. This microform edition is protected against
unauthorized copying under Title 17, United States Code.

ProQuest Information and Learning Company
300 North Zeeb Road
P.O. Box 1346
Ann Arbor, MI 48106-1346

Acknowledgements

Whew! It's Phinally Done. After completing this I can honestly say it is the hardest thing I have ever done. It would also be fair to say that without the support and assistance of some key players, I would not be at this point.

First and foremost, I need to thank my advisor Dr. Mark Rashid. He personifies the definition of mentor and friend. Not only is he an exemplary teacher but a brilliant researcher as well. Dr. Rashid's support and guidance were an important catalyst to the completion of my doctorate. My sincerest thanks.

I would also like to thank the rest of my dissertation committee, Dr. Mike Hill and Dr. John Bolander. Both offered continual support and assistance, even stepping up as surrogate advisors while Dr. Rashid was on sabbatical. Special thanks to Dr. Hill for his time and help with the aluminum tensile tests.

Daret Kehlet deserves much gratitude for his friendship and assistance throughout the process. I can't thank him enough for his help machining the tensile test specimens. If it weren't for our 'Procrastination Through Conversation' sessions I don't think I would have made it sanely to this point. (Of course I might have made it a little sooner.)

The entire Civil Engineering department, especially the office staff, created a very supportive atmosphere that made a big difference in completing the degree. When things

were crazy and hectic I could always count on the CE office to make me feel like family and help me quickly take care of any administrative problems.

I also need to thank Eric Steffler and the Idaho National Engineering and Environmental Laboratories. Specifically I would like to thank the INEEL for their support and the use of their facilities during my three summers in Idaho. My experience at the INEEL would not have been so positive had it not been for my mentor there, Dr. Eric Steffler. Dr. Steffler deserves much thanks for his part in bringing me to the INEEL and even more thanks for being such a good friend and adviser.

It goes without saying that I am very grateful for the love and support of my family. Succeed or fail, they are on my side. I am especially appreciative of my Mom who I could always count on to lend a sympathetic ear.

Finally, I want to thank Alan Nilsson. I know this hasn't been easy on you. Thank you for sticking by me and being my best friend. Coming home to you and Sid every night made it all bearable.

Ductile Fracture Mechanics: Modeling, Experiments, and Computational Simulation

Abstract

Accurately modeling ductile fracture behavior of metals is a necessary but difficult task. Recently, a new theoretical framework, the Exclusion Region, ER, theory, for modeling ductile fracture, along with a numerical method, the Arbitrary Local Mesh Replacement method, to accommodate crack advance in a finite element mesh, have been developed and show significant promise in advancing the accurate prediction of elastic-plastic fracture. This model was previously implemented in the two-dimensional finite element code FEFRAC in a linear version and a fully nonlinear version. The ER theory has already shown accurate results in the linear FEFRAC version. However, for the ER theory to be a useful modeling tool for inelastic materials, material constants for ductile materials to support the ER theory must be determined.

The present research attempts to determine material constants for a ductile material to validate the ER theory. To this end, a model-driven full matrix experimental program of fracture tests was completed using 2024 Al specimens in both symmetric and unsymmetric three-point bend configurations. Using the load, CMOD, and crack length experimental data, comparisons to these same values as determined by the finite element

implementation of the ER theory were made for the purpose of calibrating the proposed material constants of the Exclusion Region theory. During this process, it was determined that the 2024 Al's behavior in the near-tip region is not indicative of typical ductile fracture behavior. This resulted in the lack of applicability of conventional local constitutive models for ductile behavior. As this research's goal was to show the applicability of the ER theory and not to develop a new constitutive model, model calibration continued with experimental data collected from other researchers for three-point bend specimens of Inconel 718.

The ER theory successfully modeled the load vs. CMOD behavior of the Inconel 718 fracture specimens. Initial ranges of appropriate magnitudes for fracture-related material constants are suggested for the Inconel 718. This modeling work provides a richer understanding of the applicability of the various stress- and deformation-based separation criteria used in conjunction with the ER theoretical framework to accurately model ductile fracture.

Table of Contents

Chapter 1 - Introduction	1
1.1 Opening	1
1.2 Historical Development.....	2
1.3 Previous Work in Non-Linear Fracture Mechanics	4
1.4 Scope of The Present Work.....	13
Chapter 2 – Theoretical Framework	15
2.1 Introduction	15
2.2 The Exclusion Region Theory	16
2.2.a Displacement Field and Equilibrium	17
2.2.b Development of the Separation Criterion	21
2.3 Computational Implementation of the Exclusion Region Theory	24
2.3.a The Arbitrary Local Mesh Replacement Algorithm	25
2.3.b Material State Remapping	32
Chapter 3 – Experimental Data.....	38
3.1 Introduction	38
3.2 Three Point Bend Tests of 2024 Aluminum	39
3.3 Determination of Material Properties of 2024 Aluminum.....	45
3.4 Inconel 718 Data	50

Chapter 4 – Computational Modeling	52
4.1 Introduction	52
4.2 Determination of the Separation Function.....	53
4.2.a. Forced-Based Separation Function	53
4.2.b. Deformation-Based Separation Criterion.....	56
4.3 Computer Simulation.....	59
4.3.a Modeling the 2024 Aluminum.....	61
4.3.b Modeling the Inconel 718.....	68
4.4 Fitting the Material Parameters.....	71
4.4.a Load vs. CMOD Comparisons.....	72
4.4.b Comparison of Computer Simulated Crack Lengths to Experimental Data	82
4.5 Application of the Material Parameters to Plane Stress.....	85
4.6 A Possible Indicator of Unique Φ_c and ER radius values	88
Chapter 5 – Conclusion	91
5.1 Observations and Conclusions.....	91
5.2 Suggested Directions of Further Work	94
Bibliography	97
Appendix A - Load vs. CMOD Curves	102
Figure A.1 – Aluminum 2024, SYM test.....	103
Figure A.2 – Aluminum 2024, SYMA test.....	103
Figure A.3 – Aluminum 2024, A-18 test.....	103

Figure A.4 – Aluminum 2024, B-18 test	103
Figure A.5 – Aluminum 2024, C-18 test.....	106
Figure A.6 – Aluminum 2024, D-18 test	106
Figure A.7 – Inconel 718 with $\Phi_c = 0.075$, $c_o = 19.61$ mm	107
Figure A.8 – Inconel 718 with $\Phi_c = 0.080$, $c_o = 19.61$ mm.....	107
Figure A.9 – Inconel 718 with $\Phi_c = 0.085$, $c_o = 19.61$ mm.....	108
Figure A.10 – Inconel 718 with $a = 0.0254$ mm, $c_o = 19.61$ mm.....	108
Figure A.11 – Inconel 718 with $a = 0.0508$ mm, $c_o = 19.61$ mm.....	106
Figure A.12 – Inconel 718 with $a = 0.0635$ mm, $c_o = 19.61$ mm.....	106
Figure A.13 – Inconel 718 c_o comparison, with $a = 0.0635$ mm &	
$\Phi_c = 0.065$	109
Figure A.14 – Inconel 718 c_o comparison, with $a = 0.0508$ mm &	
$\Phi_c = 0.07$	109
Figure A.15 – Inconel 718 c_o comparison, with $a = 0.0381$ mm &	
$\Phi_c = 0.08$	110
Figure A.16 – Inconel 718 c_o comparison, with $a = 0.0254$ mm &	
$\Phi_c = 0.085$	110
Appendix B – Supplemental Aluminum 2024 Material Information.....	111
Figure B.1 – Aluminum 2024, Material Data Sheet	112
Figure B.2 – Aluminum 2024, SEM Electron Backscatter Plot.....	113
Appendix C – Aluminum 2024 Fracture Specimen Photographs	114
Figure C.1 – A typical SYM fracture specimen.....	115

Figure C.2 – Typical crack path angle of A-18 specimens	115
Figure C.3 – Typical crack path angle of C-18 specimens	115
Figure C.4 – A typical SYMA thin fracture specimen	116
Figure C.5 – Typical B-18 thin specimen	116
Figure C.6 – Typical C-18 thin specimen	116
Appendix D – Inconel 718, Comparison of Mesh Size	117
Figure D.1 – Comparison of fine, standard and coarse meshes for Inconel 718 finite element mesh refinement verification.	118

List of Figures

Figure 2.1 – Volume of material surrounding the separation front that has been excluded from the conventional description of the continuum problem, the Exclusion Region	16
Figure 2.2 – The Exclusion Region in two dimensions.....	18
Figure 2.3 – Normal and shearing forces (F_n and F_s) on the ER boundary	21
Figure 2.4 – Evolution of patch mesh during non self-similar crack growth.....	28
Figure 2.5 – Three components of the ALMR method: background mesh, patch mesh, and new free surfaces.....	28
Figure 2.6 – Resolved geometry of a partial element for the determination of integration points.....	30
Figure 2.7 – Tributary regions of old and new integration points as determined by Voronoi tessellation	35
Figure 3.1 – Sample geometry for 2024 Al test specimens.....	39
Figure 3.2 –Sample A-18-2 during test with notches for roller supports and crosshead	41
Figure 3.3 – 2024 Al testing apparatus: the Instron 1325	41
Figure 3.4 – 2024 Al elastic unloading curves for the determination of incremental crack length at each unloading per ASTM standard E 1820	44
Figure 3.5 – 2024 Al uniaxial tension test specimen geometry.....	46
Figure 3.6 – Load vs. strain curves for 2024 Al uniaxial tension tests	46

Figure 3.7 – Engineering stress vs. strain curve for 2024 Al uniaxial tension Test #1	46
Figure 3.8 – 2024 Al true stress vs. logarithmic plastic strain curve for the determination of the power-law hardening parameters.....	49
Figure 3.9 – Inconel 718 – Load vs. CMOD data for 3-point bend specimen fracture test..	51
Figure 3.10 - Inconel 718, True stress vs. plastic log strain plot for the determination of the parameters for power-law hardening model.	51
Figure 4.1 - Separation function versus load parameter curve for the traction –based separation criterion.....	55
Figure 4.2 - Separation function versus load parameter curve for the deformation-based separation criterion.....	58
Figure 4.3 – Node locations of the general framework of the finite element mesh for the symmetric Inconel 718 specimens	62
Figure 4.4 – The effect of mesh refinement on load vs. CMOD curves for 2024 Aluminum SYM model.....	64
Figure 4.5 – Results of initial computer simulations of 2024 Aluminum showing unrealistically high peak loads.....	64
Figure 4.6 – Effect of lowering Φ_c on the P vs. CMOD curve for 2024 Aluminum with a constant at 0.08 mm	65
Figure 4.7 – Load versus CMOD curves for various values of Φ_c and the ER radius, a, for modeling the 2024 Aluminum SYM case	66
Figure 4.8 - Load vs. CMOD curves for 2024 Aluminum computer simulations with unrealistically low yield stress values.....	66

Figure 4.9 - Node locations of the general framework of the finite element mesh for the symmetric Inconel 718 specimens	69
Figure 4.10 - The effect of mesh refinement on load vs. CMOD curves for Inconel 718....	71
Figure 4.11 – Variations in the computed Inconel load vs. CMOD curves for varying Φ_c and a values with $c_o = 19.61$ mm.....	72
Figure 4.12 - (a) The effects of varying Φ_c on load vs. CMOD plots for Inconel – 718 with $c_o = 0.772$ mm and $a = 0.0381$ mm (b) The effects of varying a on load vs. CMOD plots for Inconel – 718 with $c_o = 0.772$ mm and $\Phi_c = 0.07$.....	74
Figure 4.13 - Comparison of the Inconel 718 experimental results to the computational load vs. CMOD curves for the four shown Φ_c and the ER radius combinations postulated to give the best fit results.....	80
Figure 4.14 - Comparison of load vs. CMOD curves for simulations with the initial crack lengths at $c_o = 19.18$ mm and $c_o = 19.61$ mm.....	82
Figure 4.15 - Experimental load vs. crack length curve for Inconel 718.....	83
Figure 4.16 – (a) Comparison of computer simulated load vs. crack length curves with $c_o = 19.18$ mm to experimental results (b) Comparison of CMOD vs. crack length curves with $c_o = 19.18$ mm to experimental results.....	84
Figure 4.17 – Comparison of plane stress computation results for load vs. CMOD curves to Inconel 718 experimental data.....	87
Figure 4.18 – Trends in the Pmax vs. crack length at Pmax for Inconel 718 with $c_o = 19.61$ mm	89

Figure 4.19 - Comparison of load vs. CMOD for $\Phi_c = 0.07$ with $a = 0.0508$ mm and $\Phi_c = 0.08$ with $a = 0.0381$ mm with $c_o = 19.61$ mm to experimental data.....	93
Figure A.1 – Aluminum 2024, SYM test	103
Figure A.2 – Aluminum 2024, SYMA test	103
Figure A.3 – Aluminum 2024, A-18 test.....	104
Figure A.4 – Aluminum 2024, B-18 test.....	104
Figure A.5 – Aluminum 2024, C-18 test.....	105
Figure A.6 – Aluminum 2024, D-18 test.....	105
Figure A.7 – Inconel 718 with $\Phi_c = 0.075$, $c_o = 19.61$ mm	106
Figure A.8 – Inconel 718 with $\Phi_c = 0.080$, $c_o = 19.61$ mm	106
Figure A.9 – Inconel 718 with $\Phi_c = 0.085$, $c_o = 19.61$ mm	107
Figure A.10 – Inconel 718 with $a = 0.0254$ mm, $c_o = 19.61$ mm	107
Figure A.11 – Inconel 718 with $a = 0.0508$ mm, $c_o = 19.61$ mm	108
Figure A.12 – Inconel 718 with $a = 0.0635$ mm, $c_o = 19.61$ mm	108
Figure A.13 – Inconel 718 c_o comparison, with $a = 0.0635$ mm & $\Phi_c = 0.065$.....	109
Figure A.14 – Inconel 718 c_o comparison, with $a = 0.0508$ mm& $\Phi_c = 0.07$.....	109
Figure A.15 – Inconel 718 c_o comparison, with $a = 0.0381$ mm & $\Phi_c = 0.08$.....	110
Figure A.16 – Inconel 718 c_o comparison, with $a = 0.0254$ mm & $\Phi_c = 0.085$.....	110
Figure B.1 – Aluminum 2024, Material Data Sheet.....	112
Figure B.2 – Aluminum 2024, SEM Electron Backscatter Plot.....	113
Figure C.1 – A typical SYM fracture specimen	115
Figure C.2 – Typical crack path angle of A-18 specimens	115

Figure C.3 – Typical crack path angle of C-18 specimens	115
Figure C.4 – A typical SYMA thin fracture specimen.....	116
Figure C.5 – Typical B-18 thin specimen	116
Figure C.6 – Typical C-18 thin specimen	116
Figure D.1 – Comparison of fine, standard and coarse meshes for Inconel 718 finite element mesh refinement verification	118

List of Tables

Table 3.1 – Geometry and loading data for Aluminum test specimens	40
Table 3.2 – Comparison of measured and calculated initial crack lengths, Aluminum 2024, SYM specimens	45
Table 4.1 - Coordinates of the general framework of the finite element mesh for the symmetric 2024 Aluminum specimens.....	62
Table 4.2 - Coordinates of the general framework of the finite element mesh for the symmetric Inconel 718 specimens.....	69
Table 4.3 - The influence of Φ_c on computational loads and crack lengths with $c_0 =$ 19.61 mm	76
Table 4.4 - The influence of a on computational loads and crack lengths with $c_0 = 19.61$ mm	76
Table 4.5 – Variations in P_{fracture} and P_{max} for the four best-fit Φ_c and ER radius combinations	81

Chapter 1 - Introduction

1.1 Opening

The observation of cracks forming in materials is not a recent one. In the time of early humans, fractures in stones were a useful flaw of which to take advantage. They were the weaknesses that allowed humans to first shape tools and later form the large stone pieces used in structures both great and small (Cotterell and Kaminga 1990). However, as materials available for developing tools and structures changed, weaknesses caused by cracks were no longer something to utilize but rather something to avoid. The development of iron and steel was a major component in improving how we designed and fabricated our world. The industrial revolution, which could not have occurred without the availability of these metals, brought significant advances in machinery and infrastructure. Suddenly engineers had materials with higher strengths, higher ductilities, and low weights that provided the ideal properties for building longer span bridges, larger and lighter storage tanks, taller buildings, and more powerful steam engines. These materials had well understood ultimate and yield stresses and designers used care to engineer structures well below these limits using factors of safety as high as ten (Anderson 1995). However, catastrophic failures due to fracture still occurred. These unexplained failures led to the initiation of a new field of research, which finally, in the 1950's, gained the now familiar name of fracture mechanics.

1.2 Historical Development

Fracture mechanics is the study of the behavior of bodies containing cracks. Primarily, the field is concerned with whether or not an existing crack will propagate, and if it does, whether or not it grows stably as well as the direction of its propagation. The study of fracture in ductile materials is a relatively young field that only came into prominence after the 1940s and 1950s. Historically, there has been an understanding of linear-elastic fracture mechanics since the early 1920's when A. A. Griffith developed his energy criterion for modeling crack growth in brittle materials such as glass (Griffith 1920). Griffith found that by including the surface energy associated with crack formation, the "theorem of minimum potential energy" can be extended to predict the breaking loads of elastic solids. Griffith postulated that the energy expended in the formation of traction free surfaces is derived from the strain energy released in the entire elastic solid, and that this expended energy in a hypothetical crack extension was a useful measure of the conditions required for crack propagation (Griffith 1920).

While this work was a major breakthrough in the prediction and modeling of fracture behavior, it was limited to isotropic elastic materials. At the structural level, the crystals of crystalline metals are anisotropic and are not accurately modeled by this theory (Griffith 1920). Further, to simply relate surface energy to separation energy is physically unsatisfying, because energy is also dissipated by plastic work in the bulk of the material during crack growth in all materials except purely elastic – i.e. "perfectly brittle" - materials. Thus, Griffith's theory is invalid in the presence of any significant bulk plasticity. A final limitation to this breakthrough is the requirement that the crack

path be known *a priori* due to symmetry. Any asymmetry due to loading, geometry, or anisotropy invalidates this theory.

For thirty years after Griffith's work was published, a small number of researchers continued looking for ways to extend his work with little success, and the field of fracture mechanics stagnated. Then, in the 1940's and 1950's, a number of catastrophic failures of metal structures and machinery occurred, including the well-documented Liberty Ship failures and the De Havelind Comet aircraft failures. These unfortunate incidents led to a resurgence in the study of fracture mechanics, and in the late 1950's the next significant contribution to the field was made. Dr. G. R. Irwin of the Naval Research Laboratory expanded Griffith's theory to include fracture in metals under conditions of small scale yielding – i.e. where yielding is confined to a zone that is small when compared to the specimen or crack dimensions. Irwin's modified theory assumes the crack extension requires a constant rate of inelastic dissipation during crack extension (Rossmannith 1997). To support his theory, Irwin introduced the parameter G , which can be interpreted as a "crack extension driving force" (Irwin 1956). G is defined as "the strain energy loss rate associated with extension of the fracture accompanied only by plastic strains local to the crack surfaces" (Irwin 1957). As the previous quote illustrates, Irwin recognized that the primary contribution to G at fracture is bulk plasticity near the crack tip, with only small or negligible contribution from the surface energy, in contrast to Griffith's theory. Irwin then utilized G along with Westergaard's (1939) semi-inverse procedures to determine expressions for the elastic stresses and strains near the leading edge of a crack with brittle behavior.

Along with the Strain Energy Loss Rate, G , today referred to as the Strain Energy Release Rate, Irwin introduced the Stress Intensity Factor, K , which is proportional to the square root of G in the case of self-similar crack growth. K is determined as the multiplier on the first term of the asymptotic expansion of the elastic solution for the stress as the crack tip is approached. Both G and K provide useful measures in the analysis of crack growth under conditions of small-scale yielding. Extensive experimental studies have provided critical values of both these parameters for different engineering materials, making them useful design tools in linear-elastic fracture mechanics. The critical value of K , i.e. K_c , is typically given as a material property that measures the fracture toughness of a material. However, to actually be a meaningful property, both variables require that any plasticity occurring in the near tip region occur over a range significantly smaller than the crack length. If this condition is met, G_c and K_c are useful measures of fracture toughness for materials, and are therefore useful for fracture resistant design. If, on the other hand, yielding occurs over a non-negligible (but still small) distance, the first term in the asymptotic expansion of the elastic stress field does not necessarily dominate. In this case, the second term is sometimes considered in formulating a fracture criterion. In particular, the contribution of the second term to the stress directly ahead of and acting in the direction of the crack is referred to as the T stress. In the case of high-confining stresses, the T stress is sometimes included in the definition of a fracture parameter.

1.3 Previous Work in Non-Linear Fracture Mechanics

In the case of ductile fracture of metals, the large size of the plastic zone renders both G

and K inapplicable. This fact left researchers in search of a tool for modeling inelastic fracture behavior. A significant step in completing this search was achieved in 1968 when J. R. Rice introduced the *J*-integral (Rice 1968). The *J*-integral is an extension of Irwin's theory to include non-linear elastic behavior. For a linear elastic material, Rice's formula produces Irwin's parameter, G. The *J*-integral is based on a deformation theory of plasticity as opposed to an incremental, or flow, theory. The "deformation theory" is simply nonlinear elasticity with a stress-strain curve that resembles that of an elastic-plastic material upon loading. Upon unloading, the deformation theory behaves elastically – a conspicuous departure from the real behavior. Although the *J*-integral is not based on the flow theory of plasticity, it has been widely embraced by the fracture community as a criterion for elastic-plastic fracture. Under very specific geometric and loading conditions, the *J*-integral is able to effectively model crack growth in the presence of moderate amounts of plasticity. "However, the deformation theory of plasticity upon which the strict definition of *J* rests imposes severe limits on the amount of crack extension in metals which can be uniquely characterized by the *J*-integral. The plastic wake behind the growing tip and the strongly non-proportional loading of material ahead of the tip effectively invalidate *J* as a unique descriptor of the immediate near-tip fields" (Newman and Dodds 1997). Due to the *J*-integral's inability to offer geometry independent values of fracture toughness for elastic-plastic fracture, researchers have continued developing alternatives and extensions to this method.

In the search for improved methods, one area that has received significant attention is the expansion of the *J*-integral to include the effects of constraint. Constraint characterizes

the three dimensional effects of the material surrounding the crack tip. Gradients in the strain field can limit the ability of the material at the crack front to deform, which can cause a tri-axial stress state. While, constraint is primarily a function of specimen thickness, it is also influenced by loading and has recently been shown to be a function of residual stress and thermal loading (Hill and Panontin 2002). As known from materials science, hydrostatic stresses in ductile materials can greatly affect the material's behavior. If the specimen in question is in a pure hydrostatic stress state, then the effective (i.e. von Mises) stress of the material is zero, and conventional theories of plasticity predict a factor of safety against yield rising to infinity. However, it is also well known that hydrostatic stresses in ductile materials promote void growth and coalescence, which lead to fracture.

The influence on fracture, of the above described constraint effects, is seen in the comparison of thick fracture specimens to thin fracture specimens, i.e. plane strain vs. plane stress conditions. In the thin case, which corresponds approximately to the plane stress idealization, the transverse normal stress, σ_{zz} , is zero. The maximum shear stress criterion predicts the material will yield along shear planes at a stress equal to the maximum shear stress at yield in a uniaxial tension test. This leads to the 45 degree shear lips seen in ductile fracture, and the entire crack surface may be along 45 degree shear planes. However, in the case of thick specimens, a transverse stress, σ_{zz} , is generated due to the near plane strain conditions, and a hydrostatic stress state is developed, which promotes fracture. The fracture at the specimen surfaces will occur on shear planes as in thin specimens, however with the thicker material, extending the fracture surface along

45 degree shear planes through the thickness is no longer possible and a flat fracture surface will result over most of the specimen thickness (Dowling 1999).

Early in the history of fracture research, the effect of constraint on the crack path and on crack growth stability was observed. Therefore, it seems logical that researchers began supplementing the *J*-integral with constraint parameters as a means to improve the accuracy and applicability of *J* as a fracture criterion. As stated previously, the *J*-integral is capable of accurately characterizing the material state at the tip of the crack for limited geometries. For specimens with a significant amount of material surrounding the crack tip, i.e. high constraint conditions where the majority of the crack surface remains flat, it has been asserted that the *J*-integral is applicable as a single characterizing parameter of the crack-tip field (O'Dowd & Shih 1992). However, since all fracture conditions are not under high constraint, work on two-parameter methods emerged and is still receiving attention as a means to model ductile crack growth, specifically in the case of low constraint.

Of the two-parameter theories, Henry & Luxmoore (1997) point out that the *J-T* and the *J-Q* models are well established. The *J-T* theory is based on the elastic T stress parameter introduced by Larsson & Carlsson (1973) and Rice (1974) and has seen development by Hancock and colleagues (Al-Ani & Hancock 1991, Betegón & Hancock 1991, Du & Hancock 1991). The *J-Q* theory was proposed by O'Dowd and Shih (1992) where Q can be defined as a triaxiality parameter and is equal to the ratio of the difference between the current hydrostatic mean stress, σ_m , and the hydrostatic mean

stress at small scale yielding, $(\sigma_m)_{SSY;T=0}$, to the yield stress, σ_y . A negative value of Q indicates the hydrostatic stress state is lower than a reference value, and a condition of low triaxiality exists. This situation may be connected to a loss of J dominance. A positive value of Q indicates a higher hydrostatic stress state than the reference condition, which leads to high constraint effects and J dominated conditions. Therefore, as the plastic flow progresses from small scale yielding to fully yielded conditions, the Q value provides a measure of the evolution of constraint (O'Dowd & Shih 1992, Henry & Luxmoore 1997).

While these two-parameter models are an improvement to the J -integral approach, they have had only limited success in modeling experimental results. This may be due to a key similarity that exists among all the methods mentioned above; i.e. they are all macroscopic models, whereas fracture initiation in ductile materials ultimately is controlled by microscopic events. Accordingly, current work in fracture is moving toward micromechanical models of the crack initiation and propagation process.

Crack growth in ductile materials has been observed to occur under a process that includes void nucleation, followed by void growth and finally void coalescence. Therefore, many present day researchers are attempting to model this process as a means of characterizing fracture behavior, and are utilizing the work of Gurson (1977) on void growth in ductile metals. Assuming that a porous material may be represented as a continuum, the Gurson model characterizes the plastic flow of the material by homogenizing the effects of voids. The Gurson model reduces to J_2 flow theory in the

absence of microscopic voids. Otherwise, void growth occurs in response to plastic flow in the presence of hydrostatic tension. In fracture-mechanics applications of the Gurson model, a failure criterion, based on a critical void volume fraction, is introduced. A limitation of the Gurson model in this context is the inability of the model to account for necking between individual voids in the final stages of coalescence.

Tvergaard (1982) and Tvergaard and Needleman (1984) subsequently modified the Gurson model to better calibrate it to experimental data. These modifications greatly improved the ability of the Gurson model to characterize plastic flow in the early stages of the ductile fracture process, but they did not address the limitations of the Gurson model with respect to necking instability between voids, which leads to the final stages of ductile fracture (Anderson 1995). Further, the calibrations were all completed under ideal laboratory conditions, and some researchers (Zhang, et al. 1999) have expressed their difficulty in determining the physical meaning of some of the model coefficients, which can lead to difficulties in actual applications.

While some research has been undertaken which addresses the limitations of the Gurson model by including necking (Thomason 1985, 1998 and Komori 1999), the majority of the current research continues to build on Gurson's work to create ductile fracture models which account for void growth and coalescence. Promising work has been presented by Xia and Shih (1995a), which has been built upon by other researchers in, for example, dynamic fracture (Koppenhoefer and Dodds 1998) and ductile tearing in part-through cracks (Gao et al. 1998).

An example of the damage-based approach to fracture is the work of Xia and Shih (1995a, 1995b, & 1996), who authored a series of papers introducing a computational “cell model” for modeling ductile fracture. In this model, the formation of the new free surfaces is the result of the attainment of a critical level of damage in a thin material layer. As observed by the authors, many ductile metals display a planar fracture process zone on the order of one to two void spacings in thickness. In this model, Xia and Shih idealize this fracture process zone with a single row of finite elements that are characterized by the Gurson-Tvergaard model, with initial volume fraction f_o . To achieve this, the authors use Gurson’s relation for dilatant plasticity to model the progressive damage in the voided row, while the remaining background material is modeled with conventional J_2 plasticity. This approach inherently inserts a length scale into the model: the thickness, D , of the row of Gurson elements. The authors postulate that this value has a microstructural basis, as it is related to the thickness of the “process zone.”

Xia and Shih’s work has shown potential in predicting specimen behavior for materials that can be modeled with a consistent void size. However, research by several authors suggests that cell models with a single void size are inadequate for many materials and conditions. In the case of materials containing two distinct sizes of voids, Brocks et al. (1996) found that the single internal variable for void volume fraction, f , is insufficient for characterizing the fracture process. Further, Zhang et al. (1999) states that the growth of void volume is largely dependent upon the void size and void spacing. Their research found that “Calculations using cell models containing two voids give very different

results about the stable and unstable growth of voids that are strongly dependent on the configuration of the cell model."

Although Xia and Shih (1995a) state that their "computational model shows considerable promise as a predictive tool in nonlinear fracture mechanics analysis", cell models, whether they use a single-size void or multiple-size voids, remain limited to symmetric conditions. In fact, cell models require that the finite element mesh contain a row or rows of voided cells on the presumed crack path. The crack path must therefore be known from symmetry *a priori*. Real world fracture conditions rarely conform to such ideal symmetric conditions: A more generally applicable predictive method must have the ability to predict a non-self-similar crack path.

Another micromechanical model is the stress modified critical (plastic) strain criterion, SMCS. This method departs from continuum void growth and recognizes that ductile fracture initiation is a function of the stress and the deformation state near the crack tip. Specifically, if the equivalent plastic strain at a particular distance from the crack tip exceeds a defined critical plastic strain, fracture initiation is predicted to occur. Mackenzie et al. (1977) proposed that the critical plastic strain is a function of the "triaxiality ratio" – i.e. the ratio between the hydrostatic stress and the von Mises stress at a given point. Recent work by Panontin and Sheppard (1995) and Panontin and Hill (1996) has verified the applicability of SMCS to ductile fracture initiation in high-toughness steels, with later work (Hill and Panontin 2002) applying the method to high strength aluminum alloys. Although the value of the critical plastic strain varies at each

step of the analysis and therefore does not provide a material constant for fracture toughness, this method still offers a physically meaningful approach to fracture initiation, as the fracture criterion is not limited in its validity to a specific geometry or loading condition. Extension of this theory beyond ductile fracture initiation to include ductile tearing still needs to be explored.

Additional research to model fracture at the micromechanical level has led to the development of cohesive zone models with various cohesive laws. These theories build upon the theories of Dugdale (1960) and Barrenblatt (1962). Cohesive models present crack growth as a gradual process where cohesive forces, determined by a traction-separation law – a relation between cohesive surface traction and displacement separation - resist the separation that takes place across evolving separation surfaces. Recent works (Camacho and Ortiz 1996, de-Andrés, et al 1999, Needleman 1992, Siegmund and Brocks 2000) model this process as irreversible, and quantify the separation or fracture energy along with the cohesive strength of the material. In ductile fracture, where void nucleation, growth, and coalescence occur, the cohesive zone law is taken as a uniaxial representation of the mechanical behavior of the ductile fracture process (Siegmund and Brocks 2000).

While cohesive zone models are appealing from a physical behavior standpoint, the current research has some limitations. In terms of numerical modeling, as with the cell models, application of this theory in finite elements requires the user to predefine the location of the cohesive zone, thus limiting the crack path to pre-existing element facets.

An additional limitation found in this method is discussed in the work of de-Andrés et al. (1999), which extends the work of Camacho and Ortiz (1996). de-Andrés et al. (1999) use the J -integral to establish a link between the critical energy release rate, G_c , and the cohesive law. G_c is found under conditions of nonlinear elasticity and then the theory is applied to elastic-plastic crack growth. As discussed previously, the J -integral is extremely limited in its application, so Siegmund and Brocks (2000) take a slightly different approach by utilizing the energy dissipation rate, R , which is the sum of the plastic dissipation rate and the energy required to separate two surfaces. In their paper, R is found from experimentally derived J - Δa curves, and any implication that this theory is based on deformation theory is negated as the J - Δa curves were derived from experiment. However, since J - Δa curves can only be derived under very specific geometric conditions, the authors are still potentially limited in the scope of their theory. In fact, Siegmund and Brocks (2000) concluded that due to the effect of triaxiality on the micromechanisms of void growth and coalescence, “the cohesive zone parameters for ductile tearing, cohesive strength and energy are predicted to be generally dependent on the amount of crack growth, specimen geometry and size.” Hence, they are not truly material parameters.

1.4 Scope of the Present Work

Although significant work, as discussed above, has gone into modeling non-linear crack growth, the need still exists for a general modeling framework for ductile fracture under arbitrary conditions of geometry, loading, and crack path. This overall modeling framework should retain its applicability in the presence of linear elastic, non-linear

elastic, or elastic-plastic fracture. A fixed, geometry independent parameter or parameters that identify the critical conditions under which crack growth will occur should be a part of the framework.

The scope of this work is to develop such parameters for a ductile material to support a new framework for modeling ductile fracture. To develop these material constants, a model-driven experimental program of fracture tests was completed using 2024 Al specimens in both symmetric and unsymmetric three-point bend configurations. Using the aforementioned framework, along with a specialized finite element code developed to support this theory, computer simulations were run with the intention of calibrating the model parameters using experimental load vs. crack mouth opening displacement (CMOD) data collected from the aluminum testing. Additional experimental data was also used to calibrate model parameters for Inconel 718.

The following chapters present a detailed account of the fracture model, its numerical implementation, and the results of the calibration study. Chapter 2 presents the Exclusion Region, ER, theory, a new theoretical framework for modeling fracture, and FEFrac, the finite element code written to support this theory. Details of the experimental program and data reduction for both the aluminum and Inconel data are presented in Chapter 3. Computer simulations are explained in depth in Chapter 4, along with the results of these computer simulations. Chapter 5 presents conclusions regarding this work and possible directions for future research.

Chapter 2 – Theoretical Framework

2.1 Introduction

The development of a general modeling framework for ductile crack growth under arbitrary geometry, loading, and crack path conditions begins with a reassessment of the applicability of conventional continuum mechanics. A fundamental hypothesis of classical continuum mechanics is locality, which assumes that the deformation experienced in a sufficiently small material neighborhood is continuous and uniform. The physical relevance of the local constitutive model depends on this hypothesis. During fracture, material points that lie in the path of surface separation suffer discontinuous and non-uniform displacement fields. In these small material neighborhoods, the locality hypothesis of classical continuum mechanics is no longer valid. This violation of the locality hypothesis suggests that the classical constitutive theory must be modified or expanded by some means to accommodate fracture, generating a need for an extension to the standard boundary-value problem.

This need has instigated the development of a modeling framework for fracture called the Exclusion Region, ER, theory (Rashid 1997). The ER theory is a modification of the standard boundary-value problem of continuum mechanics in the immediate neighborhood of the surface separation to create a generalized constitutive model. The mechanics of the ER theory are enriched to embrace the formation of new free surfaces

as part of the problem solution. The basic premise of the Exclusion Region theory is that crack growth occurs when the material state in a small region at the crack tip becomes critical in a certain sense.

The theory was developed in a three-dimensional framework. To solve both linear and non-linear fracture mechanics problems, it has been implemented in previous research in a two-dimensional framework in the finite element code, FEFrac. The development of the theory and a discussion of separation criteria are presented in Section 2.2. The theory's implementation in the finite element code, FEFrac, is discussed in Section 2.3.

2.2 The Exclusion Region Theory

In the Exclusion Region theory, the standard boundary value problem of continuum mechanics is modified to allow for richer kinematics in a small material neighborhood containing the crack tip. For example, consider a three-dimensional continuum body in an undeformed reference configuration, and containing a space curve, Γ , representing the potential separation front. The curve Γ may advance through the body, leaving in its wake a pair of new free surfaces that are subsequently subject to boundary conditions.

A portion of Γ is shown in Figure 2.1. In the ER theory, a small volume of material, L_0 ,

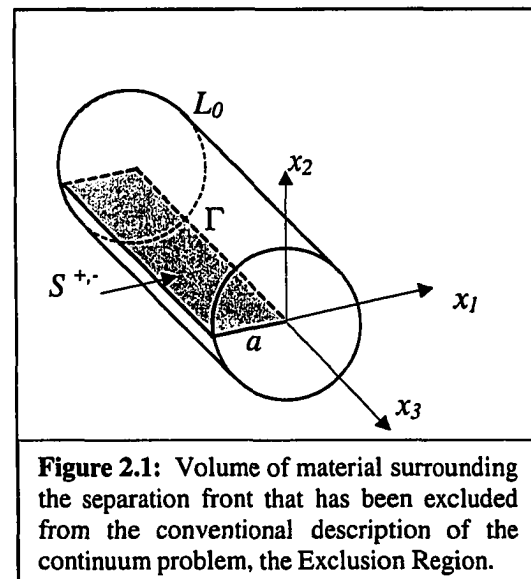


Figure 2.1: Volume of material surrounding the separation front that has been excluded from the conventional description of the continuum problem, the Exclusion Region.

surrounding the separation front, Γ , is “excluded” from the conventional description of

the continuum problem, in the sense that neither the bulk constitutive model nor the local equilibrium equations are enforced within it. However, the points on the ER boundary, ∂L_O , obey the local constitutive model. This region, the “Exclusion Region” (ER), is in principle not limited to a circular-section, tube-like shape, but was chosen as such for definiteness and convenience of the formulation.

Within the ER, a *generalized constitutive model* that includes the kinematics of separation is derived based on the local constitutive model of the bulk continuum. The generalized form must embrace a general displacement distribution on ∂L_O that can suffer a jump at the new free surfaces. It should be noted that if the displacement distribution on ∂L_O departs from linearity, the scale-invariance of the resulting constitutive model is lost (Rashid 1996). With the loss of scale-invariance, the radius of the ER, a , is seen as a parameter in the generalized constitutive model and introduces a length scale in the fracture model. On the other hand, if the displacement distribution does not suffer a jump at the new free surfaces and ∂L_O is subject to a linear displacement distribution, the generalized constitutive model reduces to the local one.

2.2.a Displacement Field and Equilibrium

To develop the generalized constitutive model mentioned above, an assumed displacement field is defined such that a jump in the displacement is admitted across the separation surfaces $S^{+/-}$ (Figure 2.1). In the two-dimensional theory, the following form of this displacement field is used (Figure 2.2):

$$\mathbf{u}(r, \theta) = (r/a)\hat{\mathbf{u}}(\theta) + (1 - r/a)\mathbf{g} - (r/a)(1 - r/a)v\mathbf{m} \quad (\text{EQ 2.1})$$

In the above equation, r is the radial distance from the crack tip, a is the ER radius, \mathbf{m} is the tangent vector shown in Figure 2.2 and \mathbf{g} and v are defined below. The equation is presented as the simplest form possible that allows for satisfaction of the following kinematic requirements:

- (1) At $r = a$, $\mathbf{u}(a, \theta) = \hat{\mathbf{u}}(\theta)$, where $\hat{\mathbf{u}}(\theta)$ is the arbitrary displacement distribution on the ER boundary, ∂L_O , from the bulk continuum.
- (2) At $r = 0$, the displacement, $\mathbf{u}(r, \theta)$, takes the value of the material displacement at the crack tip, \mathbf{g} .
- (3) The displacement field, $\mathbf{u}(r, \theta)$, must lead to a traction distribution, $\mathbf{t}(\theta)$, on ∂L_O that enforces overall force and moment equilibrium on the ER boundary, ∂L_O , regardless of $\hat{\mathbf{u}}(\theta)$. The displacement field must therefore contain three adjustable parameters (\mathbf{g} , v) that are to be set so that overall force and moment equilibrium of the ER is realized. The parameter v relates to a "twisting" component of the displacement field.
- (4) The displacement field, $\mathbf{u}(r, \theta)$, must admit a jump across the pair of new free surfaces in L_O at $\theta = \bar{\theta}$ if the imposed boundary displacement $\hat{\mathbf{u}}(\theta)$ exhibits such a jump.

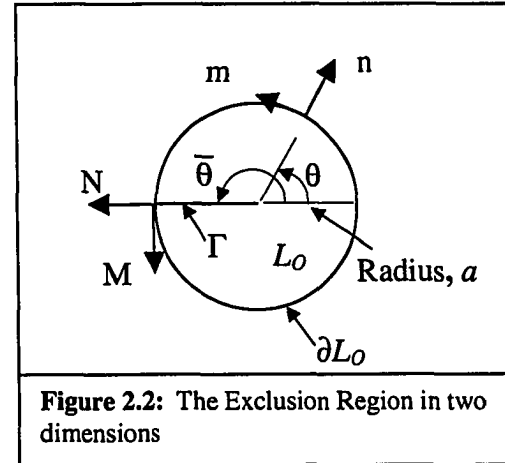


Figure 2.2: The Exclusion Region in two dimensions

The first two terms in EQ 2.1 define a linear variation in the displacement from the crack tip displacement \mathbf{g} at $r=0$ to the arbitrary boundary displacement at $r = a$. The third term includes v , a twisting parameter that leads to shearing deformations, which is crucial for enforcing moment equilibrium on the ER boundary. The values of the parameters \mathbf{g} and v are determined such that the contact forces acting on the ER boundary result in overall moment and force equilibrium of the ER. The process of determining the values of \mathbf{g} and v begins with the evaluation of the deformation gradient of EQ 2.1 at $r = a$. The local constitutive model that applies to the bulk continuum is then used to determine the stress on the boundary of the ER, using this ER-boundary deformation gradient as input. Finally, this traction distribution is used with the equilibrium equations on the ER boundary to determine the appropriate values of \mathbf{g} and v . The force and moment equilibrium equations of the Exclusion Region are expressed as:

$$\int_{-\pi}^{\pi} \hat{\mathbf{t}} d\theta = \mathbf{0}, \quad \int_{-\pi}^{\pi} \hat{\mathbf{t}} \cdot \mathbf{m} d\theta = 0 \quad (\text{EQ 2.2})$$

where \mathbf{m} is the tangent vector as shown in Figure 2.2

It should be noted that in the case of isotropic linear elasticity, the above equations decouple such that the two components of the parameter \mathbf{g} are determined from the force equilibrium equations exclusively, whereas the value of v is derived directly from moment equilibrium. Therefore, in this case \mathbf{g} and v can be eliminated, and EQ 2.1 reduces to a function of $\hat{\mathbf{u}}(\theta)$. This leads to a generalized constitutive equation where the traction on the ER boundary, $\hat{\mathbf{t}}(\theta)$, is found explicitly as a functional of the displacement on the ER boundary $\hat{\mathbf{u}}(\theta)$. This generalized constitutive model for the ER region is seen

to represent a traction distribution corresponding to an arbitrary and possibly discontinuous displacement on the ER boundary. In the absence of surface separation, with an imposed displacement $\hat{u}(\theta)$ corresponding to a constant deformation gradient, the above described functional reduces to a *function* of the displacement gradient, and the generalized constitutive model is equivalent to the local constitutive model of classical continuum mechanics. This is why it is referred to as a generalized model, as it reduces to the local model but still allows for a jump in the displacement distribution. It bears mentioning that the decoupling of EQ 2.2 and the elimination of g and v from EQ 2.1 can only be completed in closed form for isotropic linearly elastic materials. In the case of nonlinear material models, the decoupling and elimination of g and v must be carried out incrementally and iteratively before determining the generalized constitutive equation.

The displacement field defined by EQ 2.1 is not intended to represent some asymptotic displacement solution in the ER for a conventional boundary value problem. Rather, it is the basis for the development of the generalized constitutive model. The purpose of the displacement field is to characterize the near-tip material state by allowing for a jump in the displacement field at the new free surfaces ($\theta = \bar{\theta}$), and by providing a displacement gradient on the ER boundary. It is this displacement gradient that leads to a traction distribution on the ER boundary that is in overall moment and force equilibrium.

As stated earlier, the ER theory does not attempt to determine the stress and strain state “exactly” at the crack tip, i.e. as predicted by the conventional continuum theory. Its goal is to characterize the intensity of the material state in a region near the separation front,

so that a physically meaningful separation criterion can be defined. This is conceptually similar to the stress-intensity-based crack-advance criterion of conventional linearly elastic fracture mechanics. However, the ER theory does not rely on an asymptotic solution, nor on any particular constitutive model. Indeed, a broad range of constitutive models can be applied to the bulk continuum in the ER theory. In this way, the ER theory provides a basis for a fracture analysis that is driven by the local stress and deformation states in the vicinity of the crack tip, and, in this respect, is similar to recently developed micromechanical fracture models (Panontin and Sheppard 1995, Hill and Panontin 2002).

2.2.b Development of the Separation Criterion

With a generalized constitutive model in hand that allows for the characterization of the material state in the near tip region, the development of potential separation criteria was possible. As mentioned in Chapter 1, the goal of the present research is to develop a fixed, geometry-independent model that identifies the critical conditions under which crack growth occurs in ductile metals. In the case of ductile metals, where microvoid coalescence at the crack front is the usual mode of rupture, it seems reasonable that this separation criterion be based on a measure of deformation at the crack tip to correlate with observed experimental behavior. (Final results of the presented work indicated it would be more appropriate to include a measure of stress as well, see Chapter 4, Section 5). Further, in a fracture

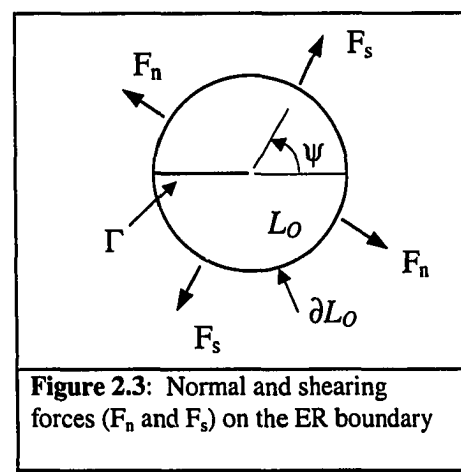


Figure 2.3: Normal and shearing forces (F_n and F_s) on the ER boundary

model that allows for surface separation along an arbitrary crack path, the separation criterion should be capable of determining the most likely direction of advance. Corresponding to the above requirements, surface separation can then be assumed to occur if the critical state at the crack tip, as defined by a direction-dependent *separation function*, meets the following constraint:

$$\Phi(\psi) = \Phi_c \quad (\text{EQ 2.3})$$

where ψ is the angle of advance that maximizes Φ , as shown in Figure 2.3. $\Phi(\psi)$ is the separation function that represents the material state at the crack tip. In the present research, $\Phi(\psi)$ is taken to be a function of the plastic strain, ϵ_p , within the ER as described in detail below. The direction dependence of Φ is taken to relate to the normal-opening forces F_n (Figure 2.3). Finally, Φ_c is postulated to be a geometry independent material parameter defining the critical state at which crack growth will occur.

The material state at the crack tip as it relates to fracture, is defined by the separation function Φ as a function of ψ , which is herein taken to be:

$$\Phi(\psi) = \frac{1}{A} \int_{ER} \epsilon_p dA \cdot \left(\frac{\langle F_n(\psi) \rangle}{F_{n_{MAX}}} \right) \quad (\text{EQ 2.4})$$

Here A is the area of the ER, and $F_n(\psi)$ is the resolved normal force on the surface of the ER boundary in a direction perpendicular to the candidate direction of advance ψ (Figure 2.3). For each value of ψ , F_n is found as:

$$F_n = \int_{\theta}^{\bar{\theta}+\psi} \hat{\mathbf{t}}(\theta) \cdot \hat{\mathbf{m}} d\theta \quad (\text{EQ 2.5})$$

where $\hat{\mathbf{t}}(\theta)$ is the traction on the ER boundary and $\hat{\mathbf{m}} = (-\sin \psi, \cos \psi)$. As shown in

Figure 2.2, $\bar{\theta}$ denotes the location of the new free surfaces. $F_{n_{MAX}}$ is the maximum value of $F_n(\psi)$ for $-\pi \leq \psi \leq \pi$.

The first term in EQ 2.4 determines the average value of the equivalent plastic strain within the ER. The second term represents the direction-dependence of $\Phi(\psi)$, and leads to a direction of advance perpendicular to the maximum opening force on the ER boundary, as would be expected in Mode I fracture. In the second term, F_n is normalized to a maximum value of 1 when $F_n(\psi) = F_{n_{MAX}}$. A plot of $F_n(\psi)/F_{n_{MAX}}$ against ψ , would result in a bell shaped curve that drops rapidly from its maximum value of one to zero as the candidate direction of advance moves away from the direction that maximizes the normal force. The Macaulay brackets, $\langle \rangle$, in EQ 2.4 are used to render the separation function insensitive to compressive stresses near the crack tip.

The above fracture criterion is used to determine whether or not the material state near the crack tip is such that the crack will extend, and, if it does, in what direction. As stated, comparison of the value of the separation function, Φ , to a critical value, Φ_c , governs crack extension. The value of Φ_c is postulated to be a material property, and the calibration of this value for a ductile material is attempted in the present research. It should be noted that “material property” is meant to imply a single number that characterizes the critical state for propagation, independent of the amount of crack growth that has already occurred. A fracture criterion based on a material property provides a distinct advantage over other approaches to ductile fracture, as discussed in Chapter 1, that are geometry dependent. The separation function described herein is just

an example of one possible choice. Many others could be defined, depending on the material.

2.3 Computational Implementation of the Exclusion Region Theory

The ER theory has been implemented in FEFRAC, a two-dimensional, finite-element based research code that is capable of modeling arbitrary crack paths and finite deformations in planar bodies. The code incorporates the Arbitrary Local Mesh Replacement (ALMR) algorithm (Rashid 1998), which addresses the changing topology of the domain in the presence of crack growth by incorporating a separate, regenerating mesh that remains centered over the Exclusion Region - i.e. the crack tip (Figures 2.4 and 2.5). The ALMR method provides a robust, efficient algorithm for addressing the significant challenge of modeling the moving discontinuities encountered in crack propagation along arbitrary paths. Complete details of the ALMR algorithm are presented later in this chapter.

FEFRAC is capable of modeling crack growth in the setting of both linear-elastic and non-linear bulk material response. To achieve this versatility in material response modeling, multiple constitutive models have been incorporated into the finite element code including linear elasticity, J_2 flow theory of plasticity with power-law hardening, and Tvergaard-Gurson dilatant plasticity. The separation criterion, as a function of the candidate direction of advance, discussed earlier in this chapter, is embedded in the FEFRAC framework, which allows the code to automatically determine, at each load step, whether an existing crack will propagate and, if so, in what direction.

In the development of FEFRAC, two significant challenges in finite element modeling of arbitrary crack growth in a ductile material were addressed: (1) how to account for the evolving geometry of the domain during crack extension, and (2) accurate remapping of the material state properties if crack extension and, hence, mesh regeneration occurs.

2.3.a The Arbitrary Local Mesh Replacement Algorithm

Initial work, which continues today, in addressing the evolution of the geometry dealt with crack paths that are known *a priori* due to symmetry. In this case, the computational challenges corresponding to the evolving topology are significantly reduced. Methods exist which allow for nodal release along element boundaries, or "nodal relaxation", as in the commercial finite element code ABAQUS, such that special discretization is not required (Malluck and King 1978, Wilsius, et al. 2000, Trädegård, et al. 1998). In a similar manner, cell models (see citations in Chapter 1), which are limited to symmetric conditions, use a thin layer of damaging material to model void coalescence. Correspondingly, the finite element mesh contains a row or rows of finite elements capable of sustaining void growth on the presumed crack path. The above methods have proved successful in the presence of a known crack path. However, if a crack is allowed to grow along an arbitrary path within a meshed domain, the resulting new free surfaces are likely to split existing elements, generally requiring complete or partial remeshing of the domain.

To address this need, Wawrzynek, et al., (1989) and Bittencourt et al. (1996) of the

Cornell Fracture Group have developed methods utilized in the linear elastic finite element code FRANC2D that performs local remeshing around the propagating crack. The work of Bittencourt et al. (1996) extended the code to provide quasi-automatic simulation of arbitrary crack growth. The remeshing scheme requires the removal of elements in the vicinity of the propagating crack. With the goal of generating a comparatively fine mesh around the crack, these elements are replaced by significantly smaller triangular or rectangular elements using recursive spatial decomposition.

The eXtended Finite Element Method (XFEM) for linearly elastic crack growth similarly attempts to refine the analysis in the neighborhood of the extending crack (Moës, et al. 1999, Dolbow, et al. 2001). However, this work takes a different approach and requires no remeshing. The crack is represented independent of the mesh with the application of an enriched discontinuous displacement field. Specifically, nodes of elements split by the crack, with the exception of elements containing crack tips, are enhanced with discontinuous functions. In the case of a crack tip, the affected element nodes are enriched with asymptotic near-tip functions. In this method, the refinement occurs in the numerical integration of the weak form, where elements, which are cut by the crack, are subdivided into subpolygons. The integration of the weak form is then carried out over the subpolygons instead of simply the element itself. Thus, the analysis is refined at the locations of the discontinuous fields.

Other work has been pursued that eliminates the difficulties of finite element mesh generation in the presence of arbitrary crack growth. A specific example is the element-

free Galerkin (EFG) method, which belongs to a family of so-called meshless methods (Belytschko, et al. 1994, 1995). The EFG method uses only nodal points and surfaces to formulate the discrete model over which the variational problem is solved. This method has the distinct advantages that no remeshing is necessary after crack growth, and adaptive refinement of the nodal points is straightforward. The EFG method is similar to finite element methods in that significant refinement of the nodes in the vicinity of the crack is required for an accurate characterization of the material state at the crack tip. Without adequate refinement, stresses determined by the method tend to be oscillatory and, as with finite element methods, achieving adequate refinement can be cumbersome and computationally expensive. To address this, later work was undertaken (Fleming et al. 1997) to enrich the EFG method by incorporating asymptotic near-tip fields in the trial functions of the Galerkin formulation. However, work has yet to be completed to extend the EFG method into non-linear fracture mechanics.

The approach used in the present research was motivated by a desire to avoid the algorithmic complexities of automatic quadrilateral mesh refinement, while at the same time providing a consistent, highly refined discretization in the near-tip region. The Arbitrary Local Mesh Replacement, ALMR, method (Rashid 1998) utilizes two meshes: the “background mesh,” which fills the entire domain, and the “patch mesh,” a small circular mesh consisting of annular rings of elements that is centered at the crack tip and is regenerated automatically on each step of crack advance (Figure 2.4). Elements in the background mesh that are completely covered by the patch mesh during a specific crack growth increment are eliminated from the overall finite element analysis. Instead, the

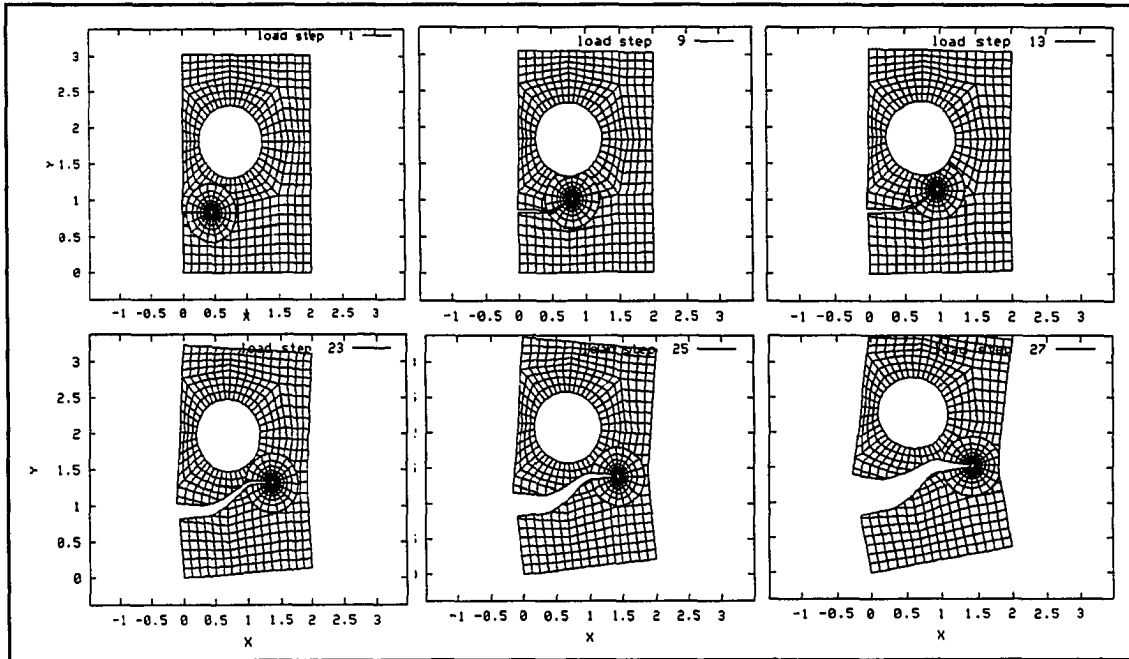


Figure 2.4: Evolution of patch mesh during non-self-similar crack growth

elements in the patch mesh are used to form the displacement interpolant inside the patch.

A key feature of this method is that crack faces are allowed to intersect the mesh at any location, such that they are not required to coincide with element boundaries in either the patch or background mesh (Figure 2.5).

Two important computational issues must be addressed with this method: (1) compatibility between the background and the patch meshes, and (2) numerical integration on the partial elements that are formed at the interface between the patch and background meshes, and in elements split by new free surfaces. To address

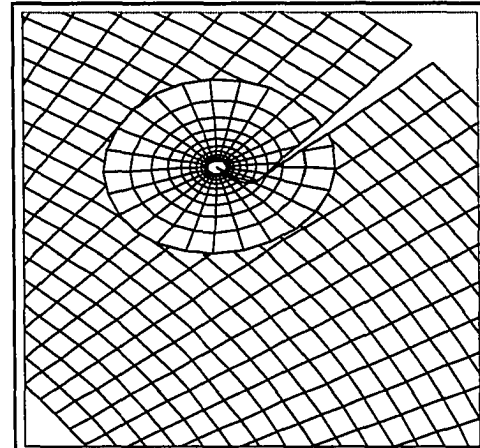


Figure 2.5: Three components of the ALMR method: background mesh, patch mesh, and new free surfaces

the first issue, a weak form of compatibility is enforced on the interface between the background mesh and the patch mesh. Specifically, the standard finite element

equilibrium equations are appended with the following weak statement of compatibility:

$$\int_I (\mathbf{u}^+ - \mathbf{u}^-) \psi_a ds = \mathbf{0}, \quad a = 1, \dots, NG \quad (\text{EQ 2.6})$$

where I is the interface between the patch and background mesh. $\mathbf{u}^{+/-}$ represent the approximate displacement solutions evaluated on I as derived from the patch mesh and background mesh respectively. ψ_a represents one-dimensional finite-element basis functions defined in relation to the nodes on I , and NG is the number of nodes on the patch boundary.

To ensure the enforcement of displacement compatibility, an equal and opposite traction distribution must be applied to either side of the patch-background interface. The traction interpolant is given as:

$$\begin{aligned} \mathbf{p}^+ &= \sum_{a=1}^{NG} \mathbf{p}_a \psi_a \text{ on } I^+ \\ \mathbf{p}^- &= -\mathbf{p}^+ \text{ on } I^- \end{aligned} \quad (\text{EQ 2.7})$$

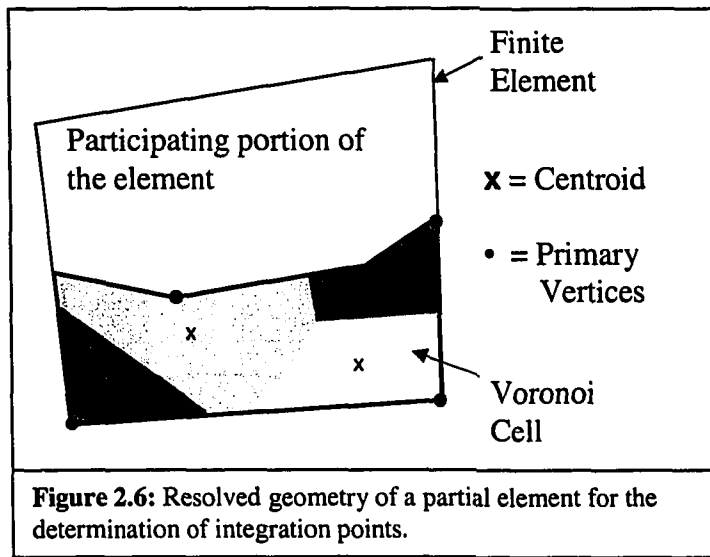
where \mathbf{p}^+ is the traction acting on the boundary of the patch, P , and \mathbf{p}^- is the equal and opposite traction acting on $B \setminus P$ (i.e. the body with the patch P excluded). The nodal values of \mathbf{p}_a will be determined such that EQ 2.6 is satisfied for all nodes on I .

The introduction of the unknown nodal tractions \mathbf{p}_a requires a modification to the weak-form equilibrium equations. Using a total-Lagrangian framework, in which the mesh discretizes the undeformed initial configuration, the weak-form equations are given as:

$$\begin{aligned} \int_{B \setminus P} \mathbf{P} \nabla \Phi_a da - \int_{\partial_i B} \mathbf{p} \Phi_a ds - \int_{I^-} \mathbf{p}^- \Phi_a ds &= \mathbf{0}, \quad a = 1, \dots, NB \\ \int_P \mathbf{P} \nabla \bar{\Phi}_a da - \int_{I^+} \mathbf{p}^+ \bar{\Phi}_a da &= \mathbf{0}, \quad a = 1, \dots, NP \end{aligned} \quad (\text{EQ 2.8})$$

where \mathbf{P} is the first Piola-Kirchhoff stress, \mathbf{p} is the traction boundary condition on the external boundary of the body, and Φ_a is the finite-element basis function associated with node a . NB and NP are the numbers of nodes in the background and patch meshes respectively. I^+ is the interface I taken as part of the patch, and I^- , correspondingly, is I taken as part of $B \setminus P$. Taken together, EQ 2.7 and EQ 2.8 constitute a complete system of equations governing the values of $\mathbf{u}^{+/-}$ and \mathbf{p}_a , such that both equilibrium and patch/boundary compatibility are weakly enforced.

Attention is now turned to the integration of the partial elements. As mentioned previously, regenerating the patch mesh, along with the new free surfaces, can result in "partial elements" on which weak-form integrals must be evaluated. To do so, the geometry must first be resolved such that locations for the integration points can be determined. Once the integration points are established, the associated weights must be assigned.



With regard to setting the integration point locations (Figure 2.6), an algorithm selects four primary vertices that are well distributed on the partial element boundary. Voronoi tessellation is applied to establish the area, within the partial element, that is nearest to

each of the primary vertices. The centroid of each resulting area, or Voronoi cell, is then determined. The four centroids are the locations of the four integration points used for the element's integration rule.

To complete the integration rule, the weights for the integration points must be determined. The method for determining the weights is based on the idea that if a polynomial is fit to the integration point data and then analytically integrated, the resulting integral will be a linear combination of the integration-point data whose coefficients are the weights. However, determining a unique polynomial of minimum order that fits the data is not possible in general. Therefore, the present method fits a higher order polynomial to the integration point data. The polynomial is reduced to remove any indeterminacy by minimizing the mean-square magnitude of its gradient over the element. This important step smoothes the fitting function while ensuring a fit to the data. Finally, the resulting polynomial is integrated *exactly* over the partial element using the divergence theorem to convert the area integral to a line integral over the partial element's boundary. The weights are then determined as the coefficients of the integral of the final polynomial, and the integration rule is complete.

With the computational challenges of enforcing compatibility between the background and patch mesh boundaries and the integration of partial elements resolved, the ALMR method has been seen to be very effective in modeling both linear elastic and elastic-plastic fracture problems (Rashid and Roy 1999). Its ability to provide a consistent mesh environment with arbitrarily high resolution in the angular direction makes this algorithm

ideal for resolving the large gradients in the material stress state associated with the near-tip region. Finally, although the ALMR algorithm was developed in support of the ER theory, it is equally applicable to other characterizations of fracture.

2.3.b Material State Remapping

Within the framework of the ALMR algorithm, the patch mesh is regenerated at each step of crack growth to insure that the center of the patch remains coincident with the extending crack tip. When mesh regeneration occurs in a finite element analysis such as the ALMR algorithm, new integration points are established that correspond to the new mesh. However, the material state information is known only at the integration points of the prior mesh. The finite element method itself does not have an indigenous means of extending the information at integration points to the entire domain. As a result, mesh regeneration in the ALMR method, and in finite elements in general, creates a significant challenge in accurately maintaining the character of the state variables as the analysis proceeds through multiple load steps.

In finite elements, remapping is conventionally achieved using a technique that involves both extrapolation and interpolation techniques. There is no “right” way to approach remapping and any scheme will inherently have inaccuracies. Further, there is no absolute standard of accuracy by which to measure the effectiveness of a remapping technique. However, there are features that a remapping algorithm should possess (Rashid 2002) as described below:

Self-Consistency. The material state values should remain constant if remapped

between identical old and new meshes. Further, a material state value that is constant throughout the entire mesh should remain constant when mapped between different meshes.

Locality. The material state at a new-mesh integration point should be contingent only on the state at those old-mesh integration points that lie within the immediate vicinity of the new point. Further, the old-mesh integration points should be “topologically connected” to the new-mesh integration point that depends on them, such that external boundaries or internal material interfaces are not able to transfer information.

Preservation of Discontinuities. If the material state of the old mesh exhibits discontinuities due to an internal mesh boundary, such as crack faces or a material interface, the remapping procedure should preserve this discontinuity in the new-mesh material state.

Freedom from Excessive Smoothing. Large gradients can occur in the near-tip region. The remapping scheme should maintain these gradients without excessive smoothing. While an exact definition of excessive smoothing is difficult to define, compliance with the first three features typically provides for freedom from excessive smoothing without additional provisions in the remapping scheme.

Freedom from Spurious Local Extrema. Regardless of the constitutive model,

this is obviously a desirable trait. However, it has greater significance in the case of plasticity models with no rate dependence or weak rate dependence, where falsely large values of stress could result in violation of the yield criterion (rate-independent plasticity) or extremely large plastic strain rates (weak rate dependence).

Potential to Incorporate Constraints. Remapped values should still meet the constraints, such as the equilibrium equations or yield criteria, that the old-mesh integration points satisfied. Failure to do so could result in overall deterioration of accuracy.

Remapping schemes do exist that satisfy some of the above features. The most common method used today is a general remapping procedure that first develops C^0 continuous state fields by extrapolation of the state variables at the integration points to the nodes of the old mesh (Peric, et al. 1996). These fields are averaged at the nodes of the old mesh to realize a continuous field using the old-mesh basis functions. Interpolation at the new-mesh integration points then yields the material state values on the new mesh. Considering the desirable features described above, this method demonstrates locality but it lacks the important feature of self-consistency (Rashid 2002).

The present research uses a remapping technique (Rashid 2002) that displays both locality and self-consistency, and is free of spurious local extrema. In this method, integration point values on both the new and old meshes are used to define the fields over

the entire domain. Specifically, the state variables of interest are defined as constant in the tributary region of each integration point (Figure 2.7). For example, let \bar{T}_k ($k = 1, \dots, \bar{K}$), where \bar{K} is the set of all old-mesh integration points, represent a set of state variables (e.g. a component of the Cauchy stress, or the current flow stress) for the old mesh, and T_k ($k = 1, \dots, K$) represent the corresponding unknown values on the new mesh. The resulting piecewise constant state fields may then be defined as

$$T(\mathbf{x}) = \sum_{k=1}^K T^k \zeta_k(\mathbf{x}), \quad \bar{T}(\mathbf{x}) = \sum_{k=1}^{\bar{K}} \bar{T}^k \bar{\zeta}_k(\mathbf{x}), \quad (\text{EQ 2.9})$$

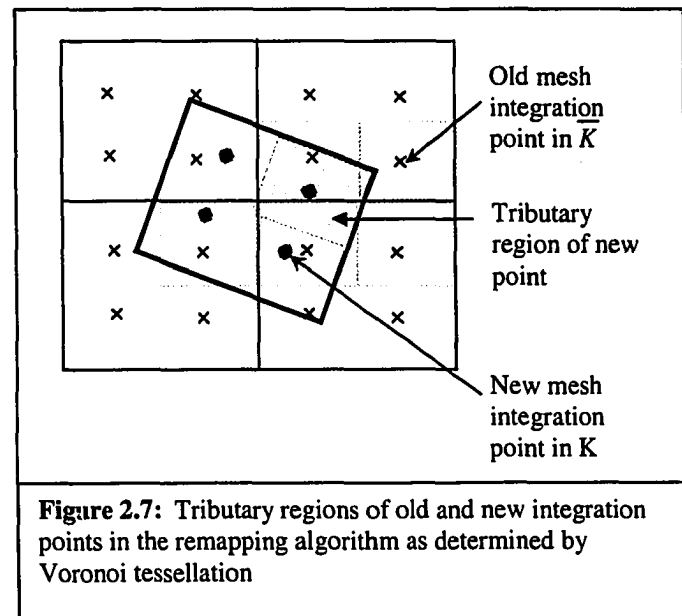


Figure 2.7: Tributary regions of old and new integration points in the remapping algorithm as determined by Voronoi tessellation

where $\mathbf{x} \in B$ and B is the reference configuration of the body. Here, ζ_k and $\bar{\zeta}_k$ are *indicator functions* such that

$$\zeta_k(\mathbf{x}) = 1, \quad \mathbf{x} \in \omega_k \quad \text{and} \quad \bar{\zeta}_k(\mathbf{x}) = 1, \quad \mathbf{x} \in \bar{\omega}_k \quad (\text{EQ 2.10})$$

$$= 0, \quad \mathbf{x} \notin \omega_k \quad = 0, \quad \mathbf{x} \notin \bar{\omega}_k$$

where ω_k and $\bar{\omega}_k$ are the tributary regions for integration points k in the new mesh and old mesh, respectively. ω_k and $\bar{\omega}_k$ are simply the transformation, under the element's isoparametric mapping, of the Voronoi tessellation of the parent element with respect to integration point k , i.e. it consists of all points in the element that are closer to interior point k than to any other interior point (Rashid 2002).

The remapping procedure itself is based on the variational enforcement of equality between the old and new material state fields. This is equivalent to least-squares minimization of the difference between new- and old-mesh fields, such that:

$$\int_B [T(\mathbf{x}) - \bar{T}(\mathbf{x})]^2 d\mathbf{v} \quad (\text{EQ 2.11})$$

is a minimum. Substitution of EQ 2.9 into EQ 2.11 and carrying out the minimization leads to:

$$T^k = \frac{1}{|\omega_k|} \sum_{l=1}^K \bar{T}^l \int_B \zeta_k \bar{\zeta}_l d\mathbf{v} \quad (\text{EQ 2.12})$$

where it becomes apparent that the new mesh values are computed directly from the old mesh values without the necessity of solving a large system of algebraic equations.

$|\omega_k|$ is the area of the tributary region ω_k . The integral in the above equation simply represents the area of overlap of the old-mesh and the new-mesh tributary regions. This allows the above equation to be rewritten as:

$$T^k = \frac{1}{|\omega_k|} \sum_{l \in A_k} V_{kl} \bar{T}^l \quad (\text{EQ 2.13})$$

where

$$V_{kl} = \int_{\omega_k} \bar{\zeta}_l d\mathbf{v}$$

which represents the area of the intersection between ω_k and $\bar{\omega}_l$. A_k is the set of all old-mesh integration point tributary regions, shown in Figure 2.7, that may have non-zero intersections with the new-mesh tributary region ω_k (Rashid 2002).

While the above development shows that this method is indeed local, the challenge of

determining the area of the intersections of these convex tributary regions still remains. It should be noted that the exact geometries of the intersections are not required, only their magnitudes. With this in mind, Rashid (2002) has developed a method that approximates the magnitude of the area of the intersection, or the *area partition*, V_{kl} , with a high degree of accuracy while still remaining a computationally efficient approach. However, in this research, an exact calculation based on the geometric intersections is utilized in the code FEFRAC.

FEFRAC's many features, including the ALMR algorithm, the robust remapping scheme, and the multiple constitutive models, have led to a proven finite element framework for modeling crack propagation (Rashid 1998, Rashid and Roy 1999). With the incorporation of the Exclusion Region theory into the FEFRAC framework, the code has the potential to provide a robust tool for predicting crack growth along arbitrary crack paths in both linear elastic and elasto-plastic conditions. To accomplish this, the critical value for the presumed separation criterion must be determined, along with the fracture model's length scale: the radius of the ER. Again, these values are both postulated to be material properties. The following chapters detail work completed to this end.

Chapter 3 – Experimental Data

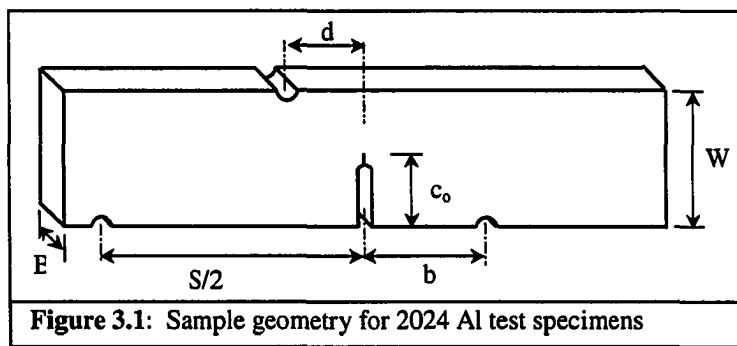
3.1 Introduction

An experimental program was undertaken in order to verify and calibrate the Exclusion Region fracture theory. A review of the literature on fracture experimentation reveals the common thread of experiments complying with ASTM standard E 1820 - 99 for fracture tests of metallic materials. These standards were established to allow researchers to interpret and present their experimental results in terms of the J -integral. As mentioned previously, the J -integral constitutes a suitable indicator of the material state at the crack tip if the specimen geometry is within a very limited geometric range that allows for high constraint conditions to develop at the crack tip. As such, ASTM standard E 1820 - 99 requires specimen geometries to lie within a very narrow range, and requires that crack growth occur along a self-similar path, limiting the geometry and loading to symmetric conditions. The objective of the test method presented in ASTM standard E 1820 – 99 is to determine fracture toughness versus crack extension, J -vs- c , curves with the purpose of deriving a material fracture toughness based on the J -Integral (where c is used to denote crack length and a is reserved for the Exclusion Region radius). With this objective, the standard is focusing on the connection between the experiment and the J -vs- c format of data presentation. As such, the issue of transferability of the results to "real-world" geometry and load conditions is rendered secondary.

3.2 Three Point Bend Tests of 2024 Aluminum

It has been proposed that the Exclusion Region theory is not limited in its applicability to specific geometries and constraint conditions. Therefore, any attempts to derive material parameters for use with the ER theory must demonstrate an independence from geometry and mode of crack growth. To this end, a program of fracture tests was carried out using 2024 Aluminum samples in the standard 3-point bend (TPB) specimen configuration. Initial experiments were conducted that did follow ASTM E 1820 - 99 requirements for specimen geometry, loading rate and initial crack lengths. These tests were completed to establish a baseline with known fracture behavior. To explore non-symmetric loading, which led to curved crack paths, variations in the support and load application locations were made. Previous work by Galvez, et al (1996) on crack trajectories under mixed-mode loading for the brittle material Polymethylmethacrylate, PPMA, or Plexiglas, was used as a reference in determining possible loading geometries. Details of these variations are given later in this section. In addition, specimens of less than half the standard thickness were also tested to allow for the investigation of constraint effects. All tests were completed at the Idaho National Engineering and Environmental Laboratories (INEEL), in Idaho Falls, ID during the summer of 2000.

The 3-point bend specimens used in this research were machined and fatigue pre-cracked according to ASTM standard E 1820 by earlier



researchers at the INEEL labs. To complete the proposed program of fracture tests, a number of the existing specimens were modified to allow for mixed-mode loading. The basic geometry of the original specimens was $W = 50.8$ mm, $B = 25.4$ mm, and $S = 200$ mm with a pre-crack depth, c_0 , of 25.5 mm (Figure 3.1). Table 3.1 identifies the modifications to the original geometry for the different variations of the test configurations. The three SYM tests identify the three tests completed with the original specimens, which followed the exact ASTM standards with symmetric loading. The A-18 series and the C-18 series both represent modifications to the SYM geometry by applying unsymmetric load and support conditions in an effort to achieve non-self-similar crack growth. Three additional sets of tests, also defined in Table 3.1, were carried out on specimens of similar geometry to those described above with the exception that the specimen thickness was reduced to 11.18 mm to study the effects of constraint. The

Specimen	c_0 , mm*	b, mm*	d, mm*	B, mm*	Load Rate mm/min	Max load for initial elastic loading cycles, kN
SYM2	25.5	100	0	25.4	0.25	14.0
SYM3	25.5	100	0	25.4	0.50	14.0
SYM4	25.5	100	0	25.4	0.50	14.0
A-18-2	25.5	20	18	25.4	0.25	20.0
A-18-3	25.5	20	18	25.4	0.25	20.0
A-18-4	25.5	20	18	25.4	0.30	30.0
C-18-1	25.5	30	18	25.4	0.25	25.0
C-18-2	25.5	30	18	25.4	0.25	25.0
C-18-3	25.5	30	18	25.4	0.30	25.0
SYM A1	25.5	100	0	11.18	0.30	7.0
SYM A2	25.5	100	0	11.18	0.50	7.0
B-18-1	25.5	20	18	11.18	0.30	10.0
B-18-2	25.5	20	18	11.18	0.35	18.0
B-18-3	25.5	20	18	11.18	0.35	18.0
D-18-1	25.5	30	18	11.18	0.30	10.0
D-18-2	25.5	30	18	11.18	0.30	16.0
D-18-3	25.5	30	18	11.18	0.30	16.0

* See Figure 3.1 for identification of each dimension label.

Table 3.1: Geometry and Loading Data for Each Specimen

SYM A series represents the symmetric load case, while the B-18 and D-18 series have unsymmetric load and support conditions.

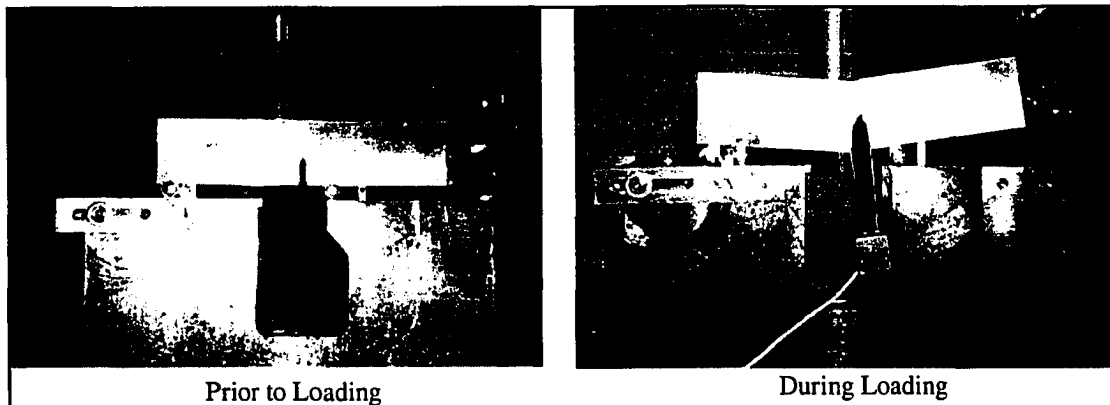


Figure 3.2. Sample A-18-2 during test with notches for roller supports and crosshead.

Notching the specimens at the location of the roller supports and the loading head was an important component of the test specimen preparation (Figure 3.1). In unsymmetric specimens without these notches, the potential exists for sliding of the roller supports, changing the support locations and therefore the test configuration. Notching the specimens at the locations of the supports and loading head insures the points of application remain constant during the test (Figure 3.2). This improves test consistency and allows for accurate representation of the support and load locations within the finite element model.

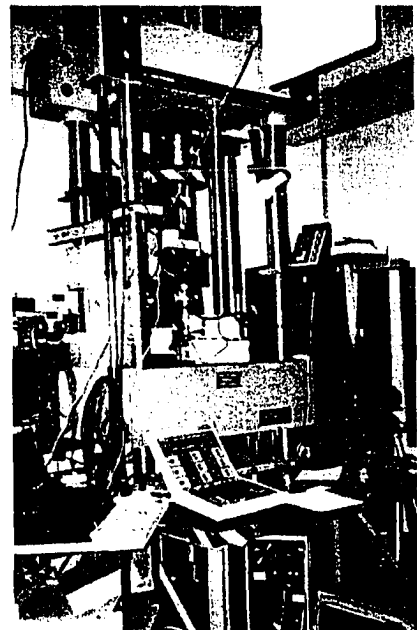


Figure 3.3: 2024 Al testing apparatus: the Instron 1325

The fracture tests were carried out on an Instron Servohydraulic Frame Model 1325 with a ServoHydraulic Control and Signal Conditioning System Model 8500 (Figure 3.3). The

load cell used was an Instron Load Cell Model 2518-100 with a 50 kN capacity in a servohydraulic system and a minimum factory specified accuracy of +/- 0.25% of the full scale capacity (actual measured accuracy is 0.1%). CMOD was measured with an Epsilon Technologies clip gage, Model 3541-005M-010M- LT, #E80753. This model has an accuracy of +/- 0.12% according to factory calibration records dated May 1999.

Although only one set of specimens, the SYM set, met the geometry and loading requirements of the ASTM standard, the fracture tests for all the specimens were carried out in accordance to the ASTM standard E 1820 – 99 guidelines for estimating crack extension using the elastic compliance method describe later in this section. These guidelines require unloading/reloading cycles at specific intervals to allow for crack extension estimates at numerous points during the test. The first five unloading/reloading cycles are required to occur at the same maximum load, which must be well within the elastic range. These initial cycles are used to collect data to estimate the initial crack length. The ASTM standard E 1820 – 99 requires the peak load for these initial cycles to fall within 50% to 100% of the maximum allowed fatigue pre-crack load, P_f . P_f , in turn, is found in accordance to ASTM E 1820 Annex A1.3.2 as

$$P_f = \frac{0.5Bb_o^2\sigma_Y}{S} \quad (\text{EQ 3.1})$$

where σ_Y is the average of σ_{yield} and σ_{ult} and $b_o = (W - c_o)$; c_o is the depth of the fatigue pre-crack. For the SYM tests, P_f is calculated to be 15.6 kN using typical values of $\sigma_{yield} = 310$ MPa and $\sigma_{ult} = 470$ MPa for 2024-T351 Aluminum. Uniaxial tension tests completed after the fracture tests showed these assumed stress values are low for this material. The experimentally derived ultimate and yield stresses, discussed in Section

3.3, result in a corrected $P_f = 19.3$ kN. As can be seen in Table 1, the maximum load reached in the five initial unloading/reloading cycles for the SYM tests is 14 kN, which is within the ASTM recommended range of 50% to 100% of the corrected P_f . For the remaining specimen geometries, which fell outside the ASTM standards, estimates were made for the appropriate maximum load of the initial unloading cycles that would keep the specimen response well inside the elastic range. If the initial estimate resulted in a maximum cyclic load that occurred within the lower half of the elastic range, the maximum load was increased for remaining tests of the same geometry. All tests were completed under crosshead displacement control. The unloading/reloading cycles for each test, as defined in Table 3.1, can be seen in the load vs. CMOD plots shown in Appendix A, Figures A.1 – A.6.

After completion of the SYM tests, the elastic compliance method, as defined in ASTM E 1820 Annex A.1.4.3, was used to estimate the crack length, c_i , at each unloading cycle. The compliance C - i.e. the inverse of the slope of the unloading cycle - was found as the slope of a linear trend line fit to a plot of each unloading cycle. Using the following equations the approximate corresponding crack length was determined:

$$c_i/W = [0.999748 - 3.9504u + 2.9821u^2 - 3.21408u^3 + 51.5164u^4 - 113.031u^5] \quad (\text{EQ 3.2})$$

where:

$$u = \frac{1}{\left[\frac{B_e W E' C_i}{S/4} \right]^{1/2} + 1} \quad (\text{EQ 3.3})$$

C_i = Compliance for each unloading cycle, $E' = E/(1 - v^2)$, and $B_e = B$ for a specimen without side grooves.

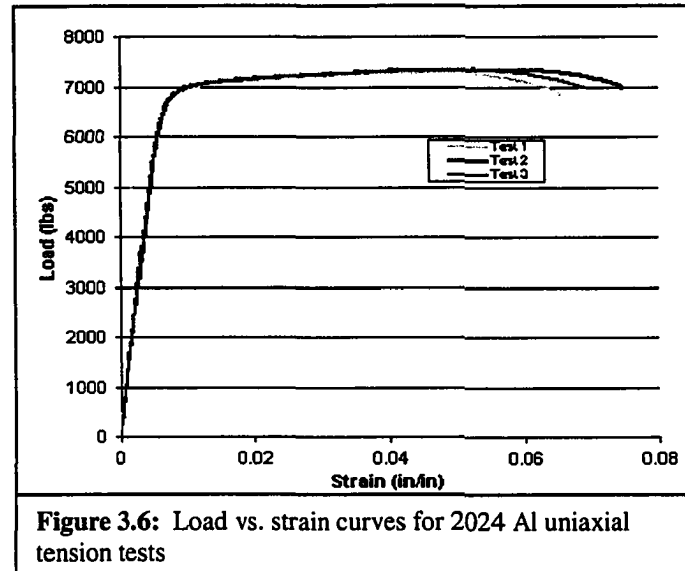
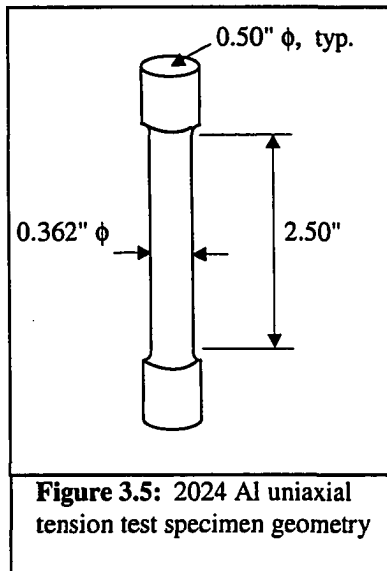
An example of the determination of the crack lengths for the SYM3 test is shown in Figure 3.4. Note the crack length in the early unloading cycles, where the material is still elastic. They vary slightly from the target 25.5 mm designated as the initial fatigue crack length. Using the elastic compliance method described above, an estimate of the initial crack length was determined from the first five unloading and reloading cycles. The estimated initial crack lengths for each SYM specimen were compared with the average initial crack length found from physical measurements (Table 3.2). The physical measurements were made, under magnification, with calipers at nine equally spaced points centered at the centerline and extending to 0.005 W from the surface per ASTM standard E 1820 – 99. In comparing the elastic compliance method estimates to the physical measurements, the greatest discrepancy can be seen in test specimen SYM3, where the percent difference between estimated and measured crack length is 1.08%. Initial crack length estimates were not made for other test configurations as the empirical ASTM equations are only valid for the SYM geometry and loading.

Specimen	Measured Initial Crack Length (mm)	Compliance Estimated Initial Crack Length (mm)	Percent Difference, %
SYM2	25.42	25.56	0.54%
SYM3	25.41	25.14	1.08%
SYM4	25.00	24.83	0.69%

Table 3.2: Comparison of measured and calculated initial crack lengths.

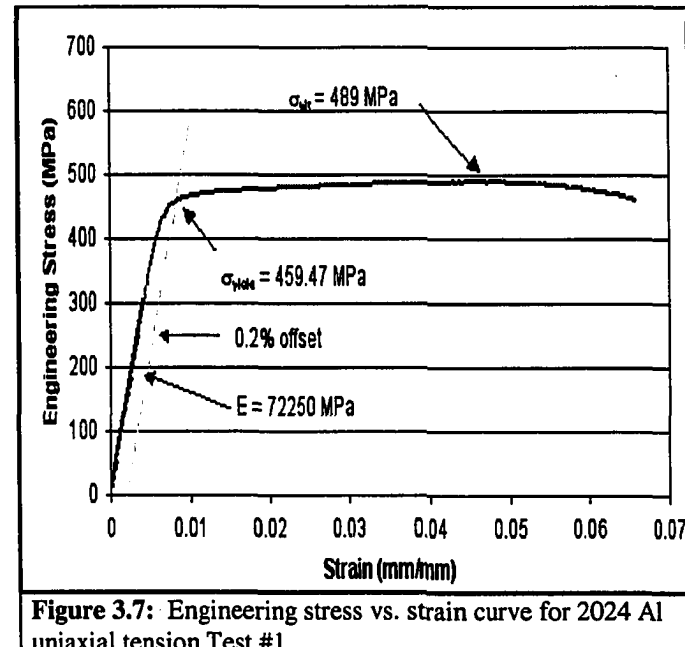
3.3 Determination of Material Properties of 2024 Aluminum

As mentioned previously, the fracture tests were completed with 2024 Aluminum TBP specimens previously prepared by researchers at the INEEL. Records kept at the INEEL indicate the bars were formed from sawed and milled 2024-T351 Aluminum plate with



no coating. Material properties and chemical composition as provided by the supplier are presented in Appendix B, Figure B.1. At the time of the fracture experiments, remaining plate stock was machined into crude TPB specimens for use in calibrating the test setup and data collection equipment. One of these specimens was later used to verify the material properties of the 2024 Al.

Four half-inch diameter rods were machined from a remaining half of the fractured crude specimen. The center two and one-half inches of length were then reduced down to 0.362 inches in diameter (Figure 3.5). Using a two-inch extensometer and an Instron



testing machine, load versus extension data was collected for the uniaxial specimens. Three tests were completed that provided consistent load versus strain plots (Figure 3.6).

The experimental data was converted to SI units and a stress versus strain curve was generated to determine the bulk material properties (Figure 3.7). The aluminum was determined to have a yield strength at 0.2% offset of 459 MPa, an ultimate strength of 489 MPa and a modulus of elasticity of 72,250 MPa. Poisson's ratio was assumed to be 0.33.

As mentioned previously, the yield and ultimate strength found in the tension tests were higher than those typically found in 2024 -T351 aluminum, with $\sigma_{yield} \approx 310$ MPa (45 ksi) and $\sigma_{ult} \approx 455$ MPa (66 ksi) as provided by the material supplier (Appendix B, Figure B.1). This discrepancy in the material properties led to the completion of additional classification tests. The first was a HRB Rockwell hardness test completed on a 0.625" diameter round bar milled from the same fractured specimen as the tension tests. The Rockwell Hardness Number was determined to be 80, including the 2 point correction required when using a round bar with the diameter = 0.625". Using the ASTM standard E 140 – 97 for Hardness conversion tables, this value was converted to a Brinell Hardness Number of 128. The Brinell Hardness Number for 2024-T351 is 120, while 2024-T81 and 2024-T851 have a Brinell Hardness Number of 128 (Reynolds Metal Co. 1965).

The material was also scanned in a scanning electron microscope, SEM. Using electron backscatter, the basic chemical composition of the material surface was determined. The SEM results (Appendix B, Figure B.2) indicate that, in addition to aluminum, the material contains copper, iron and manganese. Returning to the material data sheet for

the aluminum samples (Appendix B, Figure B.1), 2024 Al contains, in order of highest maximum concentrations after aluminum: copper, magnesium, manganese, and iron and silicon in equal percents. There are additional elements in trace amounts. As the maximum percent of silicon is only 0.5% and there is no minimum percent required, it is not unrealistic for it to not appear in a surface backscatter test. However, on the material data sheet magnesium is shown to occur in higher concentrations than both iron and manganese. As such, its presence, which was missing as indicated above, should be indicated by the surface backscatter test.

One possible explanation for the material property discrepancies would be heat treatment. If the material was heat-treated in the past, it is possible that the magnesium particles are 'trapped' under the surface with other species, which would explain their absence in the SEM results. Heat treatment would also account for the Brinell Hardness values corresponding to the heat-treated tempers, T81 and T851. Finally, σ_{yield} equals 400 MPa and σ_{ult} equals 455 MPa for T851 temper and, for the T81 temper, σ_{yield} equals 450 MPa and σ_{ult} equals 485 MPa, which corresponds directly with experimental results.

Although it is important to classify the material tested, calibration of the theoretical model with the experimental fracture tests only requires the fracture data and the values of the material properties found for the fractured material. The name assigned these material properties will not change the results of the computational model calibration.

Therefore, although uncertainties lie in the exact classification of the temper of the 2024

aluminum, the fracture data is still useful for calibration of the postulated material parameters for the Exclusion Region theory. As such, a true stress vs. logarithmic plastic strain plot was generated from the uniaxial test data for the aluminum. This was required to determine the material parameters for the power-law hardening model used in the J_2 plastic flow theory implemented in FEFRAC. The true stress was found as:

$$\sigma_{\text{True}} = \sigma_{\text{Engr}}(1 + \varepsilon) \quad (\text{EQ 3.4})$$

where ε is the experimentally measured strain and σ_{Engr} is the corresponding engineering stress found as the load divided by the original cross-sectional area. The logarithmic plastic stain was found as

$$\varepsilon_p = \ln(1 + \varepsilon) - \frac{\sigma_{\text{Engr}}}{E} \quad (\text{EQ 3.5})$$

The true stress versus logarithmic plastic strain plot was used to determine the parameters for a power-law hardening model, where:

$$\sigma_y = \sigma_{y_0} \left(1 + \frac{\varepsilon}{\bar{\varepsilon}} \right)^n \quad (\text{EQ 3.6})$$

Here $\bar{\varepsilon}$ is the reference plastic strain and n is the hardening exponent. σ_{y_0} is comparable to the yield stress of the material but is subject to fitting along with $\bar{\varepsilon}$ and n , such that the curve generated by σ_y and its corresponding strain values, ε , provide the best fit to the experimental true stress vs. logarithmic

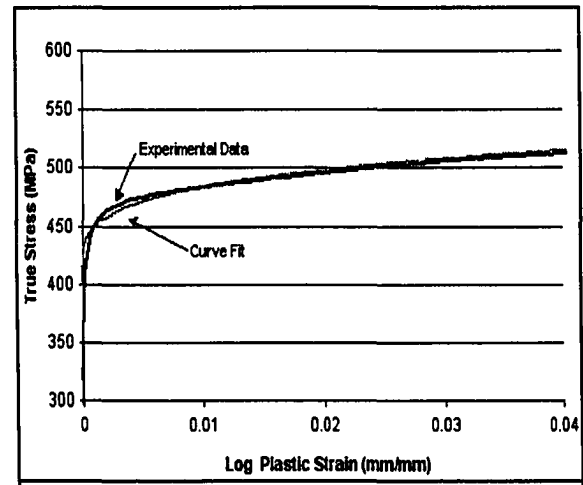


Figure 3.8: 2024 Al true stress vs. logarithmic plastic strain curve for the determination of the power-law hardening parameters

plastic strain plot (Figure 3.8). For the above curve fit to the 2024 Al data, $\bar{\varepsilon}$ equals 9.0,

n equals 0.23, and σ_{Y_0} equals 400 MPa.

3.4 Inconel 718 Data

Additional calibrations for the ER theory were completed using experimental data from fracture tests on Inconel 718 provided by Dr. Mike Hill of UC Davis. The tests completed were symmetric three-point bend specimens meeting ASTM standard E 1820 – 99. The test fixture span, S, was 152.4 mm (6 inches). The width, B, and the initial crack length, a, were 19.05 mm (0.75 inches). The specimen height, W, was 38.1 mm (1.5 inches) (Figure 3.1) (Hill and Panontin 2002).

The material properties were reported by Hill and Panontin (2002) as 219 GPa for the modulus of elasticity, E, Poisson ratio of 0.306 and a yield stress of 1036 MPa. However, difficulties in matching the slope of experimental fracture data in the elastic range prompted questions regarding the modulus of elasticity value. A review of material handbooks resulted in a modified value of the modulus of elasticity of 205.5 GPa (Everhart 1971, Lynch 1975).

Hill (2002) provided load vs. CMOD fracture data with unloading cycles as seen in Figure 3.9. Using the elastic compliance method described in Section 3.2, incremental crack lengths were determined from the unloading cycles. Using a modulus of elasticity of 205.5 GPa, the initial crack length, as estimated per ASTM E – 1820 – 99 standards, was 19.18 mm, a 0.66% error from the reported 19.05 mm initial crack length (Hill and Panontin 2002).

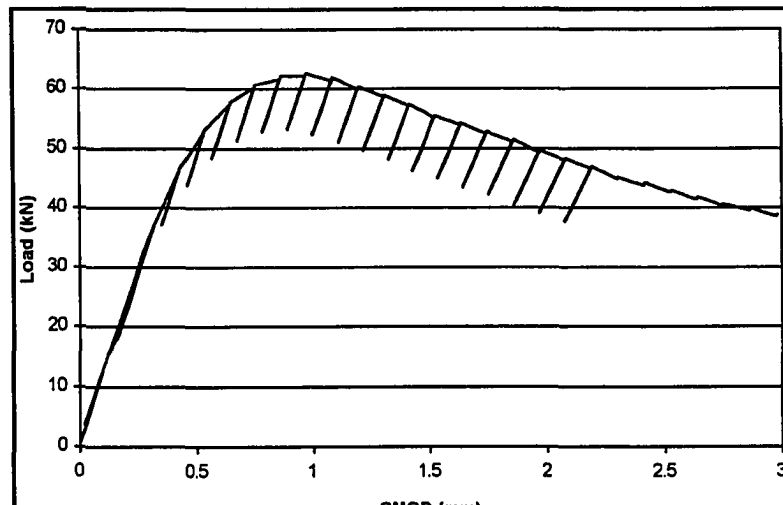


Figure 3.9: Inconel 718 – Load vs. CMOD data for 3-point bend specimen fracture test

Using waisted tensile specimens, the authors developed data points for a true stress vs. logarithmic plastic strain plot. Using this data, parameters for the power-law hardening model were found as discussed in Section 3.3 (Figure 3.10). For the Inconel 718, with a σ_{Y_0} of 1036 MPa, $\bar{\epsilon}$ was found as 0.52 and n was set to 0.72. These Inconel experimental results, along with the 2024 Al, were used to calibrate the model parameters for the ER fracture theory.

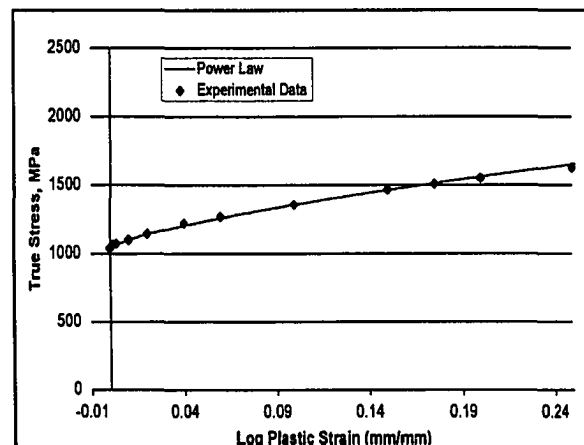


Figure 3.10: Inconel 718, True Stress vs. Plastic Log Strain plot for the determination of the parameters for power-law hardening model.

Chapter 4 – Computational Modeling

4.1 Introduction

Chapter 2 described in detail the Exclusion Region fracture theory and its implementation in FEFRAC. Previous work has shown this theory as capable of modeling the linear elastic fracture process (Rashid 1997). The following chapter presents work completed in an effort to establish the theory's ability to accurately model ductile crack growth. The collection of the experimental data described in Chapter 3 allowed for the generation of finite element models for computer simulations in FEFRAC. Using the experimental data for the load, P , crack mouth opening displacement, CMOD, and crack length, c , comparisons to these same values, as determined by the finite element implementation of the ER theory, were made with the intent of calibrating the critical separation function value, Φ_c , and the Exclusion Region radius, a , both described in detail in Chapter 2. This process was carried out for both Inconel 718 and 2024 Aluminum.

The first step in modeling the ductile crack growth experiments was determining an appropriate separation function for ductile crack growth. Therefore, prior to detailing the finite element models used to calibrate the ER theory, a discussion of the development of the separation function presented in Chapter 2 is given.

4.2 Determination of the Separation Function.

As discussed previously, the ER theory represents an attempt to characterize the near-tip environment on the premise that conditions of stress and deformation close to the crack tip are what cause the crack to extend. The primary question, then, is which is a better indicator of the near-tip conditions that lead to crack growth: the attainment of a certain crack-tip stress state or the attainment of a certain crack-tip deformation state? In an attempt to explore this question, a few different candidate separation functions were formulated and their suitability for modeling near-tip conditions in ductile materials was evaluated.

4.2.a. Forced-Based Separation Function

At the onset of the computer modeling of the 2024 Aluminum, a force-based separation function, which was initially developed for the linear-elastic version of FEFrac (Rashid 1997), was used. In this separation function, the critical state at the crack tip is assumed to relate to the maximum normal and shearing forces acting on the boundary of the Exclusion Region as follows (see Figure 2.3):

$$\Phi(\Psi) = \frac{1}{a} \left[\langle F_n \rangle^2 + \beta F_s^2 \right]^{1/2} \quad (\text{EQ 4.1})$$

Here a is the ER radius and β is a material parameter, which varies between 0 and 1. The role of β is to set the sensitivity of the fracture process to shearing along the direction of the crack. F_n and F_s are the normal and shearing forces on the surface of the ER boundary due to the tractions acting on this surface and are found as:

$$F_n = \int_{\bar{\theta}}^{\bar{\theta} + \psi} \mathbf{t}(\theta) \cdot \hat{\mathbf{m}} d\theta, \quad F_s = \int_{\bar{\theta}}^{\bar{\theta} + \psi} \mathbf{t}(\theta) \cdot \hat{\mathbf{n}} d\theta \quad (\text{EQ 4.2})$$

In the above equations, $\hat{\mathbf{n}} = (\cos \psi, \sin \psi)$ and $\hat{\mathbf{m}} = (-\sin \psi, \cos \psi)$, where ψ is the candidate direction of advance (Figure 2.2 and 2.3). F_n and F_s , the normal- and shear-opening forces, act in relation to this candidate direction.

To investigate the prospects of this formulation as a ductile fracture criterion, a finite element analysis was carried out on a compact tension geometry with $\beta = 0$ for straight ahead crack growth and the critical value Φ_c of the separation function set high enough to prevent the crack from extending. The resulting values of the separation function determined at each load step were plotted against the load parameter, which in this case was proportional to the applied load (Figure 4.1). From this plot, the following observations can be made:

- (1) Initially the value of the separation function, which essentially indicates the force on the ER under EQ 4.1, increases linearly with the increasing load parameter. This continues until the load parameter equals 0.1, which is approximately 25% of the load parameter at which the maximum value of the separation function occurs.
- (2) After the initial linear section, the slope dramatically decreases such that the magnitude of the separation function experiences a very small increase as the load parameter increases. This transition from steep to shallow slope is associated with the onset of extensive plastic deformation around the crack tip.

- (3) The separation function continues increasing, with respect to the load parameter, at this shallow slope until the maximum value of the separation function is reached at a load parameter of approximately 0.4. The presence of a maximum appears to relate to greatly accelerated blunting at large loads.
- (4) After reaching its peak, the value of the separation function drops steeply with increasing load.

A critical value for the separation function chosen from the steep-sloped section noted in Observation 1, leads to only small amounts of plastic deformation preceding crack extension, which is not consistent with typical ductile fracture

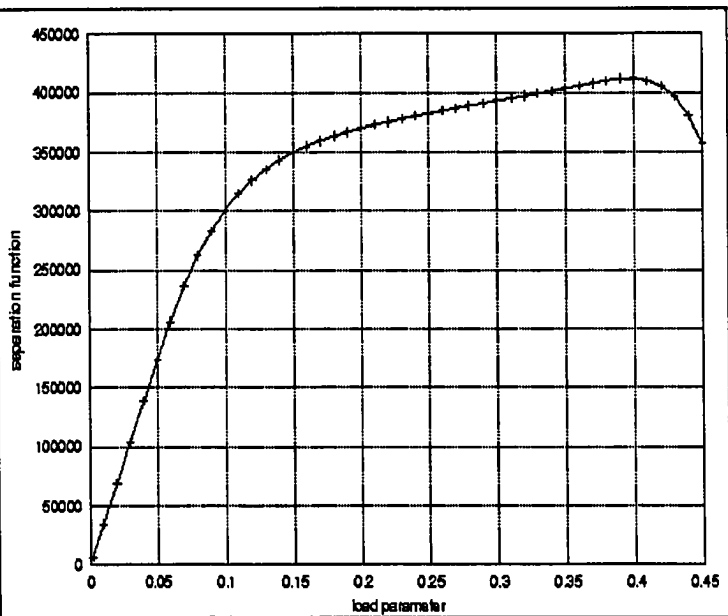


Figure 4.1: Separation function versus load parameter curve for the traction-based separation criterion.

behavior. On the other hand, taking the separation criterion from the narrow range of the shallow-sloped curve (from 330,000 to 400,000) results in large amounts of plasticity prior to crack extension. However, from Figure 4.1 it is clear that this force-based separation function requires only small changes in the value of Φ_c to move the critical state from one of low plasticity to high plasticity. If EQ 4.1 represented a suitable model of ductile fracture, sensitivity of this type would not be expected.

To further investigate the validity of this force-based separation function, the critical load criterion was set near the maximum value on the curve in Figure 4.1, and the crack was allowed to extend. From the results of the finite element analysis for the compact tension geometry, a J versus crack length, c , curve was calculated from the ASTM Test Method E 1737 procedure for experimentally determining J -vs- c using simulation output for load, crack length, and displacement. While large amounts of plastic deformation occurred prior to crack growth, the analysis resulted in an initial negative slope on the J -vs- c curve. This indicated that, although significant deformation occurred prior to the initial crack extension, only relatively small amounts of additional plastic deformation, anywhere in the body, were required for further crack growth, which is at odds with typical ductile fracture experimental observations. Therefore, it was concluded that a deformation-based separation criterion would be better suited to model ductile fracture in the Exclusion Region framework.

4.2.b. Deformation-Based Separation Criterion

The first attempt at a deformation-based separation criterion involved the use of the average deformation gradient within the ER. By determining the area average within the ER of the deformation gradient corresponding to EQ 2.1, a tensorial measure of the deformation of the ER can be obtained. For use in this research, the deformation gradient was found for the special case of planar geometry. For this condition, the area average of the deformation gradient within the ER surface is found as:

$$\bar{\mathbf{F}} = \int_{0}^{\pi} \int_{-\pi}^{\pi} \left(1 + \frac{\partial \mathbf{u}}{\partial \mathbf{X}} \right) r d\theta dr = 1 + \frac{1}{\pi a} \int_{-\pi}^{\pi} \hat{\mathbf{u}} \otimes \mathbf{n} d\theta \quad (\text{EQ 4.3})$$

where $\mathbf{n} = \cos\theta \mathbf{x}_1 + \sin\theta \mathbf{x}_2$ is the outward unit normal to the surface $r = a$ (see Figures 2.1 and 2.2) and \mathbf{u} is the displacement field in the ER as defined in EQ 2.1. In EQ 4.3, the divergence theorem was used to convert the area integral to a boundary integral that involved only the displacement on the boundary. As mentioned above, with the deformation gradient, a tensorial measure of the deformation of the ER is available. A separation criterion was then postulated using the average ER deformation gradient $\bar{\mathbf{F}}$ as follows:

$$\Phi(\psi) = \langle \mathbf{M} \cdot \bar{\mathbf{F}}^T \bar{\mathbf{F}} \mathbf{M} - 1 \rangle \langle \cos \psi \rangle^2 [1 + b(\det \bar{\mathbf{F}} - 1)] + \beta \mathbf{M} \cdot \bar{\mathbf{F}}^T \bar{\mathbf{F}} \mathbf{N} \quad (\text{EQ 4.4})$$

where $\mathbf{M} = -\sin \psi \mathbf{x}_1 + \cos \psi \mathbf{x}_2$, $\mathbf{N} = \cos \psi \mathbf{x}_1 + \sin \psi \mathbf{x}_2$, and ψ is the angle defining the candidate direction of advance. The first term in EQ 4.4 involves a measure of stretching normal to the direction of advance, while the second term is a measure of shear relative to the same direction. Macauley brackets are used to negate any effect on crack growth of compression normal to the crack surfaces, as is physically required. β is a material parameter intended to reflect the sensitivity of the material to shearing stresses in Mode 2 type separation. Including the determinant of the deformation gradient, $\bar{\mathbf{F}}$, allows the separation parameter to account for sensitivity to volumetric deformation, as occurs during void growth.

To study the behavior of the deformation-based criterion, an analysis was completed with an unrealistically high critical value of the separation criterion. As shown in the resulting plot of the separation function vs. load parameter (Figure 4.2), the initial slope is shallow, indicating initial behavior that is essentially elastic. As plasticity commences, the slope increases and the crack tip blunts. As the present separation function is based on a

measure of deformation, its value increases rapidly, as would be expected, rather than decreasing as seen in the force-based criterion. Finally, a crack-growth analysis was completed with the critical value for the separation function set at 0.1, which resulted in a rising J -vs- c ,

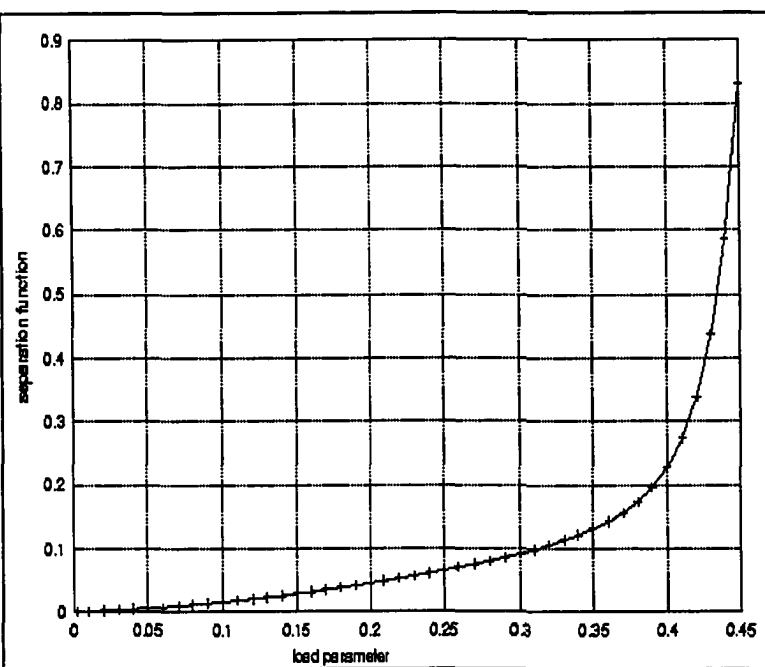


Figure 4.2: Separation function versus load parameter curve for the deformation-based separation criterion.

an expected result for ductile fracture.

The above analysis led to the initial conclusion that a deformation-based separation criterion was an appropriate model to characterize the critical state at the crack tip during ductile crack growth. The criterion defined in EQ 4.4 was then studied to determine if it offered a robust, accurate model of ductile fracture relative to observed behavior. After numerous analyses, a weakness in the model was realized. The criterion is based on the average deformation gradient within the ER, which includes both elastic and plastic contributions. The plastic deformation is a monotonically increasing function - i.e. as the crack tip approaches a material region, the plastic deformation will continue to increase until the crack tip actually enters the region and a maximum is reached. The total deformation, on the other hand, does not monotonically increase and, in fact, can

decrease. This resulted in values of the separation function at angles behind the crack tip that were higher in magnitude than those found at angles ahead of the crack tip. This was observed in the case of symmetric crack growth. As this is not a realistic characterization, a new deformation-based criterion was developed.

The new separation function was based on the notion that it is desirable for the magnitude of the separation function to reflect the progression of the material state towards fracture. It is known that some amount of local plastic deformation precedes crack growth. As noted in the above paragraph, the plastic deformation in a region ahead of the crack tip increases monotonically as the extending crack approaches until the state in that zone becomes critical, and the crack extends into the region. Therefore, the plastic deformation is thought to provide a useful measure upon which to develop the separation function. Accordingly, the deformation-based separation function used in this research is based on the average plastic strain in the Exclusion Region. Complete details of the formulation of this function were presented in Chapter 2, EQ 2.4. The use of the plastic deformation and strain, as opposed to the total deformation, is also convenient from a numerical standpoint. The plastic strain is a state variable, determined at the integration points, and, as such, can be remapped with greater accuracy than the total deformation gradient, which is determined from the displacement of the nodal points.

4.3 Computer Simulation

With a suitable separation function in hand, computer simulations of the experimental tests were now possible. Three computer codes were utilized in the complete analysis

process: FEFRAC, discussed in detail in Chapter 2; MGEN, a mesh generator; and FRPOST, a post-processor for generating plots of the deformed geometry and crack location at a given load step. The development of the finite element model begins with MGEN, which requires one input file defining the background mesh framework, the new free surfaces to define any initial crack, and the radius and number of wedges of the patch mesh. From this information, MGEN creates the binary mesh-definition file for FEFRAC that defines all node locations and element connectivity. The mesh definition file is one of two input files required by FEFRAC. The second input file is the job control and boundary condition file, which also includes the material properties, crack increment, and load step definitions. FEFRAC generates an output file used in FRPOST that allows the user to generate deformed plots at any desired load step. FRPOST gives the user two viewing options. The ‘outline’ option shows only the specimen boundaries, including crack faces, in an undeformed configuration and is useful for tracking the crack path. The ‘deformed’ option displays the entire meshed model, including the patch and new free surfaces, in its deformed state for a given load step and user-defined magnification.

Computer simulations for determining the material parameters were completed under conditions of plane strain for both materials. This is a reasonable approach given that the plane strain assumption is a close representation of physical reality for fracture specimen geometries that meet the ASTM standard E 1820-99 guidelines for ductile fracture. The modeling intent was to set the initial material parameters under plane strain conditions, with the hope that these parameters would then apply to a more complete three-

dimensional model. The initial parameters were set by seeking a best fit between the calculated and measured load vs. CMOD curves. As discussed in Sections 4.3 and 4.4, a number of different approaches were taken to determine the effects of Φ_c and the ER radius on the model-generated load vs. CMOD results. As will become apparent in the following sections, a formal, systematic optimization approach was not used to determine ideal Φ_c and a magnitudes. Such an approach would require back calculating the material parameters by minimizing the difference between the calculated and measured load vs. CMOD curves in a least-squares or root-mean-square sense. This would involve taking partial derivatives of the least-squares objective function with respect to the material parameters. However, the only way to determine the derivative information would be by means of finite differences. With only two unknown material parameters, it was decided that this systematic approach would not provide an efficient method for determining the material parameters that offered the best fit to the experimental data.

4.3.a Modeling 2024 Aluminum

The first aluminum specimens modeled were the symmetric SYM specimens detailed in Section 3.2, with the goal of establishing the fracture-related material parameters: the critical separation criterion Φ_c and the ER radius a . The intent was to then measure the validity of the values determined for these parameters with additional computer simulations corresponding to the experimental data from the unsymmetric and reduced thickness specimens. Therefore, the initial finite element work consisted of developing the input files for the symmetric loading condition.

To create the input file for MGEN, ten initial points, as shown in Figure 4.3 and Table

4.1, were defined in reference to the three-point bend specimen geometry and support conditions. The total length of the modeled specimen was 228.6 mm. The initial notch

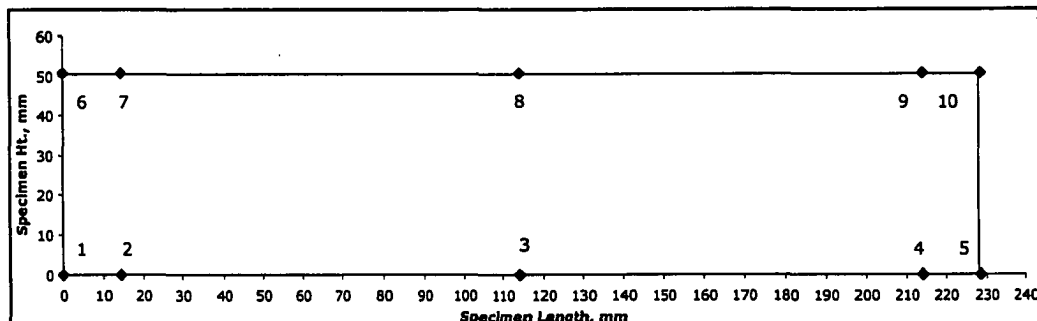


Figure 4.3: Node locations of the general framework of the finite element mesh for the symmetric Inconel 718 specimens

and fatigue crack were modeled by 10 new free segments of length 1.5 mm each. The first segment originated at the location of node 3. The last ended at the experimental location of the initial crack tip (114.3 mm, 25.5 mm). The patch was defined with a radius of 8 mm and 36 annular wedges. From these two parameters, MGEN automatically sets the number and spacing of rings of patch elements so that the elements in the patch all have aspect ratios close to one. It should be noted, the divisions chosen to define the number of elements created in the background mesh resulted in a node 2.5 mm to the left of node 3 and a corresponding node 2.5 mm to the right. This allowed FEFRAC to determine CMOD at nodes that were 5 mm apart in the undeformed

Node	X-Coordinate	Y-Coordinate		Node	X-Coordinate	Y-Coordinate
1	0.0 mm	0.0 mm		6	0.0 mm	50.8 mm
2	14.3 mm	0.0 mm		7	14.3 mm	50.8 mm
3	114.3 mm	0.0 mm		8	114.3 mm	50.8 mm
4	214.3 mm	0.0 mm		9	214.3 mm	50.8 mm
5	228.6 mm	0.0 mm		10	228.6 mm	50.8 mm

Table 4.1: Coordinates of the general framework of the finite element mesh for the symmetric 2024 Aluminum specimens.

configuration, conforming to the experimental clip gage location.

The roller/notch support described in Chapter 3 was modeled in the job control and boundary condition input file by restraining nodes 2 and 4 in the vertical direction while allowing movement in the horizontal direction. Node 8, where the crosshead contacted the specimen, was restrained in the horizontal direction. The loading of the crosshead was simulated as a traction applied over the two adjacent, exterior element edges that share node 8. The magnitude of the applied traction was 800 MPa. However, the exact value is not important since the load is multiplied at each load step by a user-defined load parameter. This occurs until the critical value of the separation function is reached; at which time, the load parameter is automatically scaled such that the separation function equals its critical value without exceeding it. This transition from “load parameter control” to “crack advance control” occurs automatically within FEFRAC.

The job control and boundary condition input file also requires the modulus of elasticity, Poisson’s ratio, and, for the power-law hardening model: the yield stress, reference plastic strain and the hardening exponent. These values, as mentioned in Chapter 3, are 72250 MPa, 0.306, 150 MPa, 0.52 and 0.72 respectively. The two fracture-related material properties, Φ_c , the critical separation function value, and a , the radius of the Exclusion Region, are also required in this input file.

The above mesh framework was used to generate two mesh-definition files for FEFRAC. The first mesh, referred to as the ‘standard’ mesh, contained 1911 nodes and 1800

elements. The second or ‘fine’ mesh contained 4247 nodes and 4080 elements. Figure 4.4 shows a comparison of load vs. CMOD curves for the fine mesh and for the standard mesh as generated by FEFRAC using identical material parameters including $\Phi_c = 0.09$ and $a = 0.06$ mm. As can be seen

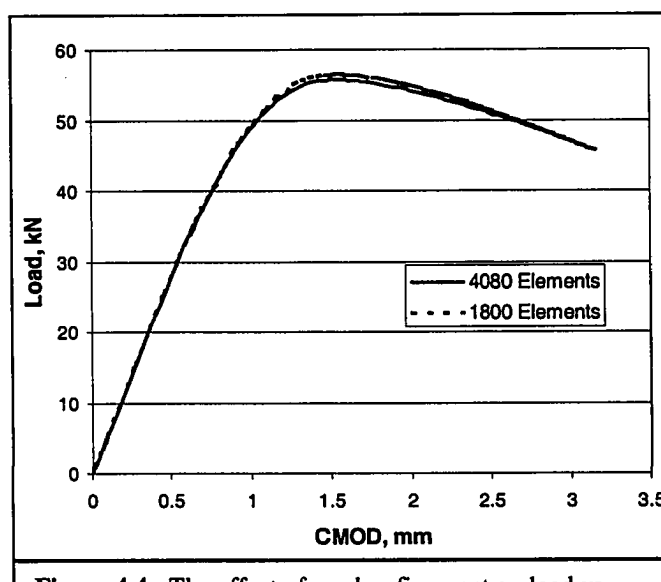


Figure 4.4: The effect of mesh refinement on load vs. CMOD curves for 2024 Aluminum SYM model.

from the figure, the two meshes provide nearly identical results. Therefore, the standard mesh, which is more economical computationally, was used in efforts to calibrate the Φ_c and ER radius values.

Initial plane strain computational models based on the input files described above revealed that, while the basic shape of the experimental load vs. CMOD curve could be duplicated, the magnitude of the load at fracture in the computer models was approximately double

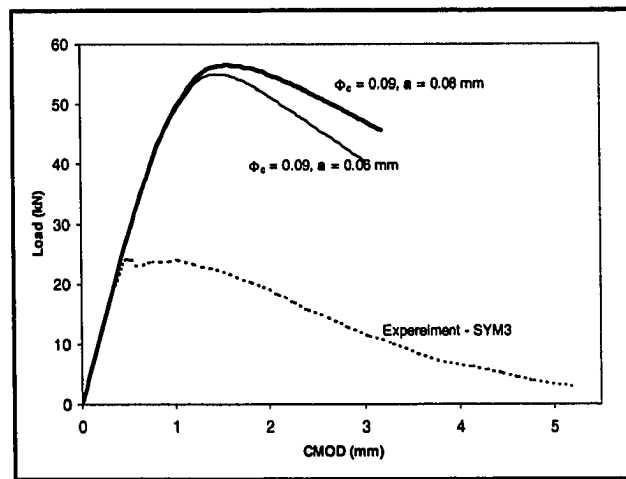


Figure 4.5: Results of initial computer simulations of 2024 Aluminum showing unrealistically high peak loads.

that observed in the experiment (Figure 4.5 and 4.6). It should be noted that the relative magnitude of the load at fracture did not vary greatly between the candidate separation

functions mentioned above, although the function based on the average of the plastic strain still provided the most realistic ductile behavior. Numerous attempts were made in an effort to reduce the load at fracture.

One approach was to reduce the separation function value such that fracture required less plastic deformation and, therefore, lower peak loads.

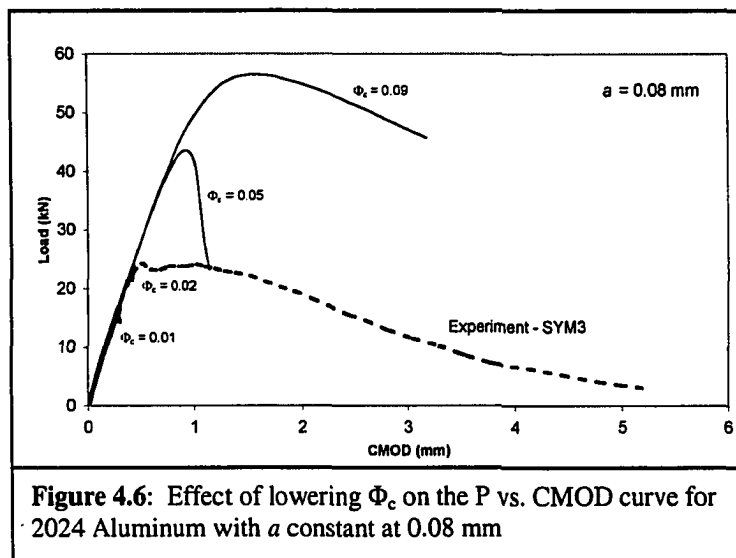


Figure 4.6: Effect of lowering Φ_c on the P vs. CMOD curve for 2024 Aluminum with a constant at 0.08 mm

The results of this approach are presented in Figure 4.6. Decreasing the Φ_c value while holding a constant did result in lower peak loads. However, fracture was occurring unrealistically early, before sufficient plasticity was able to develop. After the peak load was reached, the load vs. CMOD curves drop off steeply. In fact, the two cases with Φ_c equal to 0.01 and 0.02 show very steep concave curves with little or no additional crack mouth opening displacement after the peak load is reached (Figure 4.6). These runs both resulted in convergence errors in the computational solution.

A second tactic followed from the observation that increasing the ER radius, while holding Φ_c constant, increased both the load at which crack growth initiated, as well as the peak load. (Complete details of the effects of Φ_c and a are presented later in this chapter.) Therefore, ER radius values were increased to raise the load at crack growth initiation and allow for more plasticity to develop in the near-tip region. At the same

time, Φ_c was decreased to reduce the overall magnitudes of the loads. While this approach did bring the initial fracture loads and peak loads closer to those found in the experimental work, the resulting curves did not reflect the ductile behavior of the material, as can be seen in Figure 4.7.

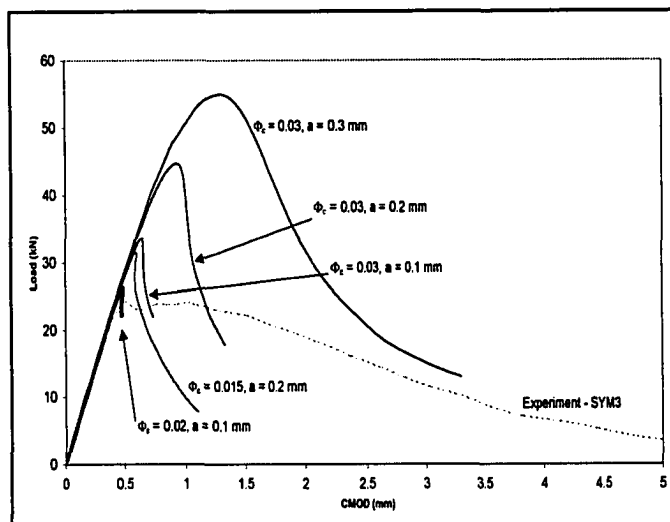


Figure 4.7: Load versus CMOD curves for various values of Φ_c and the ER radius, a , for modeling the 2024 Aluminum SYM case

As discussed in Chapter 3, the yield stress of this material as derived from tension specimens was higher than typical values reported for 2024-T3 Aluminum. Therefore, additional computer simulations were completed using reduced yield stresses, along with unchanged power-law hardening parameters. Figure 4.8 shows load

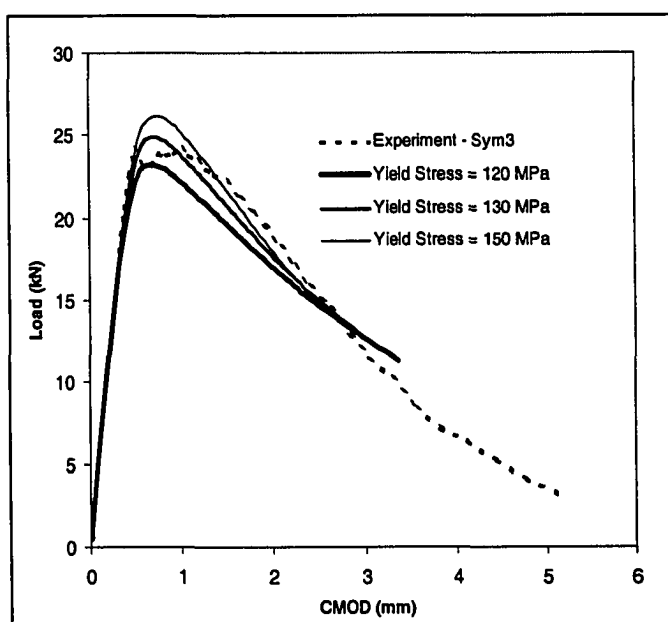


Figure 4.8: Load vs. CMOD curves for 2024 Aluminum computer simulations with unrealistically low yield stress values.

vs. CMOD curves for three identical models, with the exception that the yield stress varied from 150 MPa to 120 MPa. As these values of yield stress are unrealistic for this material, no additional effort to improve the fit between the experimental and the

computational results was made.

In reviewing the foregoing efforts at modeling the fracture behavior of this material, it is apparent that significant difficulties were encountered. The loads determined in the plane strain analyses were unrealistically high, and suitable values for the critical function criterion, Φ_c , and the ER radius, a , for this material could not be found. The question then becomes, was this difficulty a function of the ER theory itself, the separation function, or the bulk constitutive model? Of these three possibilities, the constitutive model seemed the most likely cause. This observation was reached after discussions with other researchers, including Dr. Mike Hill of UC Davis (2002) and Dr. Beth DeBartolo of Rochester Institute of Technology (2002), both of whom suggested that fracture in 2024 Aluminum does not follow the typical ductile fracture behavior that is controlled by plastic deformation at the crack tip. DeBartolo (2002) discusses a quasi-ductile fracture between precipitates. During SEM monitored crack growth, she observed plastic zones forming in front of the crack tip, followed by the crack jumping to the next precipitate, and changing direction as it traveled. This behavior is different than the standard notion of void coalescence in ductile fracture and suggests a possible cause of the modeling difficulties. The local constitutive model implemented in FEFRAC, which is used in the background continuum, on the boundary of the ER when enforcing equilibrium, and in the derivation of the plastic strain for the separation function, is the J_2 flow theory of plasticity. This theory is not an appropriate model if the crack growth behavior follows the quasi-ductile behavior discussed above. Therefore, it appears that a promising direction for future research would be the development of a new constitutive model that

is capable of modeling this quasi-ductile behavior. A possible example would be a model able to incorporate microcracking.

Due to the above described challenges in modeling the 2024 Al behavior during crack extension, it was determined that efforts to model the unsymmetric and thin 2024 Al specimens would not be relevant to the goal of the present research; i.e. to determine material parameters for a ductile material to support the ER theory. The theory and the code have already been shown to be capable of modeling arbitrarily curved crack paths (Rashid 1997). While it would be interesting to compare FEFrac crack path results to the experimental specimens, this would provide no additional information towards the objectives of the present research. Should future research lead to the development of a constitutive model that is appropriate to the 2024 Al behavior, the experimental results as presented in Chapter 3 for the unsymmetric and thin specimens would then provide a useful tool to measure the applicability of the ER theory to various geometries. As previously mentioned, load vs. CMOD curves for all 2024 Al experiments are provided in Appendix A. Photographs showing the curved paths of the fracture specimens are provided in Appendix C.

4.3.b Modeling the Inconel 718

In light of the above difficulties with modeling the 2024 Aluminum, a second material was chosen for model calibration. Inconel 718, as described in Chapter 3, was selected for this purpose.

The finite element model for the 3-point bending specimens of Inconel was developed in much the same manner as for the 2024 Aluminum. In the case of the Inconel specimens, the mesh framework described in the input file for the mesh generator, MGEN, was defined by 14 nodes (see Table 4.2 and Figure 4.9). The length between supports, S, was

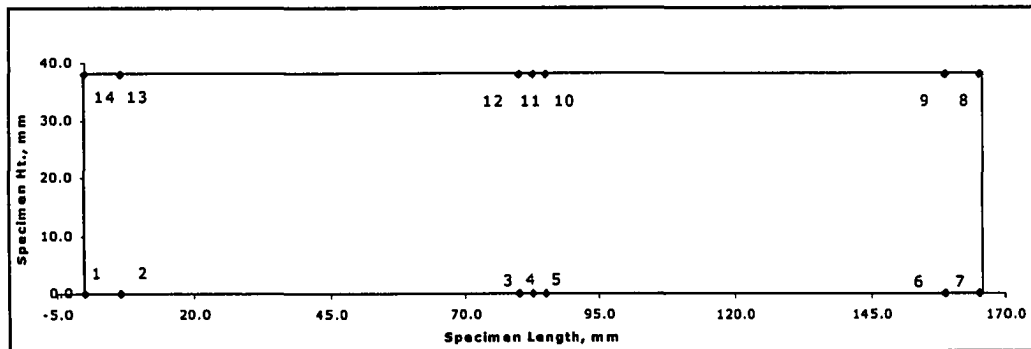


Figure 4.9: Node locations of the general framework of the finite element mesh for the symmetric Inconel 718 specimens

given as 152.4 mm. In the finite element model, an additional 6.35 mm of length was included at each end so that the nodes constrained in the vertical direction were not at the corners of the finite element mesh. This step was taken to correlate with experimental procedures. Nodes 3 and 5 were included to exactly locate the edges of the 5 mm notch where the clip gage for measuring CMOD was attached. Ten new free surface segments were used to represent the notch height and initial fatigue crack. The first nine segments

Node	X-Coordinate	Y-Coordinate		Node	X-Coordinate	Y-Coordinate
1	0.0 mm	0.0 mm		8	165.1 mm	38.1 mm
2	6.4 mm	0.0 mm		9	158.8 mm	38.1 mm
3	80.1 mm	0.0 mm		10	85.0 mm	38.1 mm
4	82.6 mm	0.0 mm		11	82.6 mm	38.1 mm
5	85.0 mm	0.0 mm		12	80.1 mm	38.1 mm
6	158.8 mm	0.0 mm		13	6.4 mm	38.1 mm
7	165.1 mm	0.0 mm		14	0.0 mm	38.1 mm

Table 4.2: Coordinates of the general framework of the finite element mesh for the symmetric Inconel 718 specimens.

were 1.905 mm. The last varied between 1.905 and 2.46 mm in length as possible variations in the initial crack length were modeled. The first new free surface segment originated at the location of node 4 as seen in Figure 4.9. The patch was generated with a radius of 8.13 mm and 36 wedges.

In the job control and boundary condition input file for FEFRAC, vertical constraints were placed at nodes 2 and 6. The loading of the crosshead was simulated as a traction applied over the two adjacent, exterior element edges that share node 11, which was also constrained in the horizontal direction. In order to distribute the reaction at the roller supports in a more realistic manner, the Inconel model included two additional tractions whose combined total force resultant was equal and opposite to the total force resultant of the traction at the crosshead. One of these force equilibrating tractions was applied on the exterior edge of the element to the left of node 2 and, likewise, on the exterior edge of the element to the right of node 6. This extra step in the modeling eliminated convergence issues in the finite element model due to a displacement boundary condition being applied at a single point. The material properties were the modulus of elasticity, $E = 205.5$ GPa, Poisson's ratio, $\nu = 0.306$, and, for the power-law hardening model, the yield stress, $\sigma_y = 1036$ MPa, the reference plastic strain, $\varepsilon = 9.0$, and the hardening exponent, $n = 0.23$. It should be noted that the crack growth increment was always set at 0.00254 mm larger than the ER radius value to keep the crack growth increment as small as possible.

Prior to the calibration work, the effects of mesh refinement were studied. Three meshes were generated using the mesh framework for MGGEN described above with $\Phi_c = 0.08$ and $a = 0.0381$ mm. The first mesh, the 'coarse' mesh, had 1660 nodes and 1558 elements. The second mesh, the 'standard' mesh, contained 2834 nodes

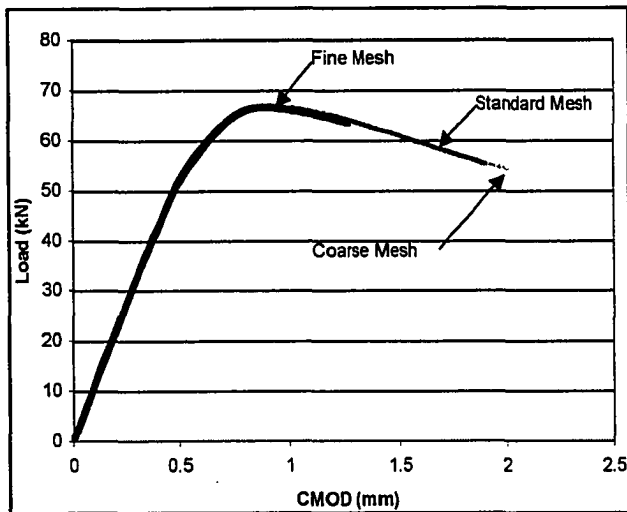


Figure 4.10: The effect of mesh refinement on load vs. CMOD curves for Inconel 718

and 2700 elements. Finally, the third or 'fine' mesh consisted of 4224 nodes and 4389 elements. The patch mesh in each case was discretized with 36 annular rings and a radius of 8.13 mm. Figure 4.10 shows a load vs. CMOD plot comparing the results of the three meshes. As can be seen, the coarse and standard meshes are essentially indistinguishable from each other. Further, the fine mesh varies only slightly from these. Although the coarse mesh appeared to offer adequate refinement, the standard mesh was utilized in subsequent computer simulations. The above meshes are shown in Appendix D.

4.4 Fitting the Material Parameters

To successfully calibrate the values of the fracture-related material parameters, efforts were made to determine the effect of the magnitude of Φ_c and the ER radius on the simulation results. As was done in the Aluminum work, the experimental load versus crack mouth opening displacement curve was used as a reference for comparison with computer-generated results for each Φ_c and a combination. Two distinct sets of computer

simulations were completed: one with the initial crack depth, c_0 , at 19.18 mm from the bottom edge of the specimen, and one with c_0 at 19.61 mm. The value of 19.18 mm was determined from the experimental data using the ASTM elastic compliance method for 3-point bend geometry, as explained in Chapter 3, with the modulus of elasticity equal to 205.5 GPa. The second value of 19.61 mm is the calculated initial crack depth if the modulus of elasticity is set at 219 GPa, the value reported by Hill and Panontin (2002). As was discussed in Chapter 3, the higher modulus value is not used in this research. However, using the second crack tip location offered a slight variation to the geometry. While it is apparent that the shorter remaining ligament would decrease the magnitudes of the loads, it was of interest to determine if the shape of the load vs. CMOD curves would vary between the two crack lengths for identical Φ_c and ER radius values.

4.4.a Load vs. CMOD Comparisons

Numerous simulations were completed for both initial crack tip locations. Almost immediately, reasonably shaped load vs. CMOD curves with load values of satisfactory magnitude were achieved (Figure 4.11). Exact matches to the experimental load magnitudes were not expected as these simulations were completed with plane

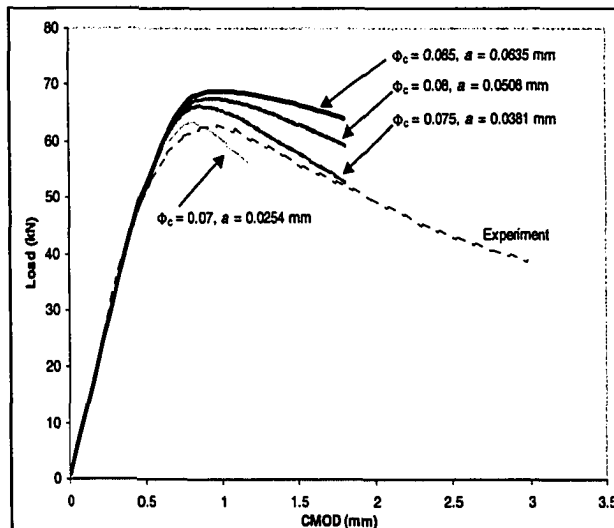


Figure 4.11: Variations in the computed Inconel load vs. CMOD curves for varying Φ_c and a values with $c_0 = 19.61$ mm.

strain calculations. As previously mentioned, the plane strain model closely represents the

behavior due to the experimental geometry. However, the experimental specimens are not truly in a state of plane strain, which will result in different loads than those measured experimentally as they do not capture the 3-D effects experienced in the actual testing.

Although the initial plane strain curves were promising, there were still significant variations in the peak loads and the final slope of the curves, which were contingent on the values of Φ_c and a (Figure 4.11). Visual comparisons of load vs. CMOD curves for more than 100 simulations led to ranges of potential values for Φ_c and a . For both c_o values, the range for the ER radius was found as 0.0254 to 0.0635 mm and 0.065 to 0.09 mm/mm for Φ_c .

During the process of completing the numerous simulations and load vs. CMOD plots, it became apparent that increasing the magnitude of the critical value of the separation function or the ER radius resulted in higher peak loads. In addition, increases in either parameter also decreased the slope of the curve after the peak load. These effects can be seen by comparing the results for $c_o = 19.61$ mm shown in Figure 4.12. In Figure 4.12(a) the ER radius value is held constant at $a = 0.0381$ mm while varying the Φ_c magnitude within the given range mentioned above. In Figure 4.12(b), Φ_c is held constant at 0.07 with ER radii varied within the suggested range of a . Additional plots in the form of Figures 4.12(a) and 4.12(b) were generated for other Φ_c and ER radii and are presented in Appendix A, Figures A.7 – A.12. From these plots, the following observations can be made.

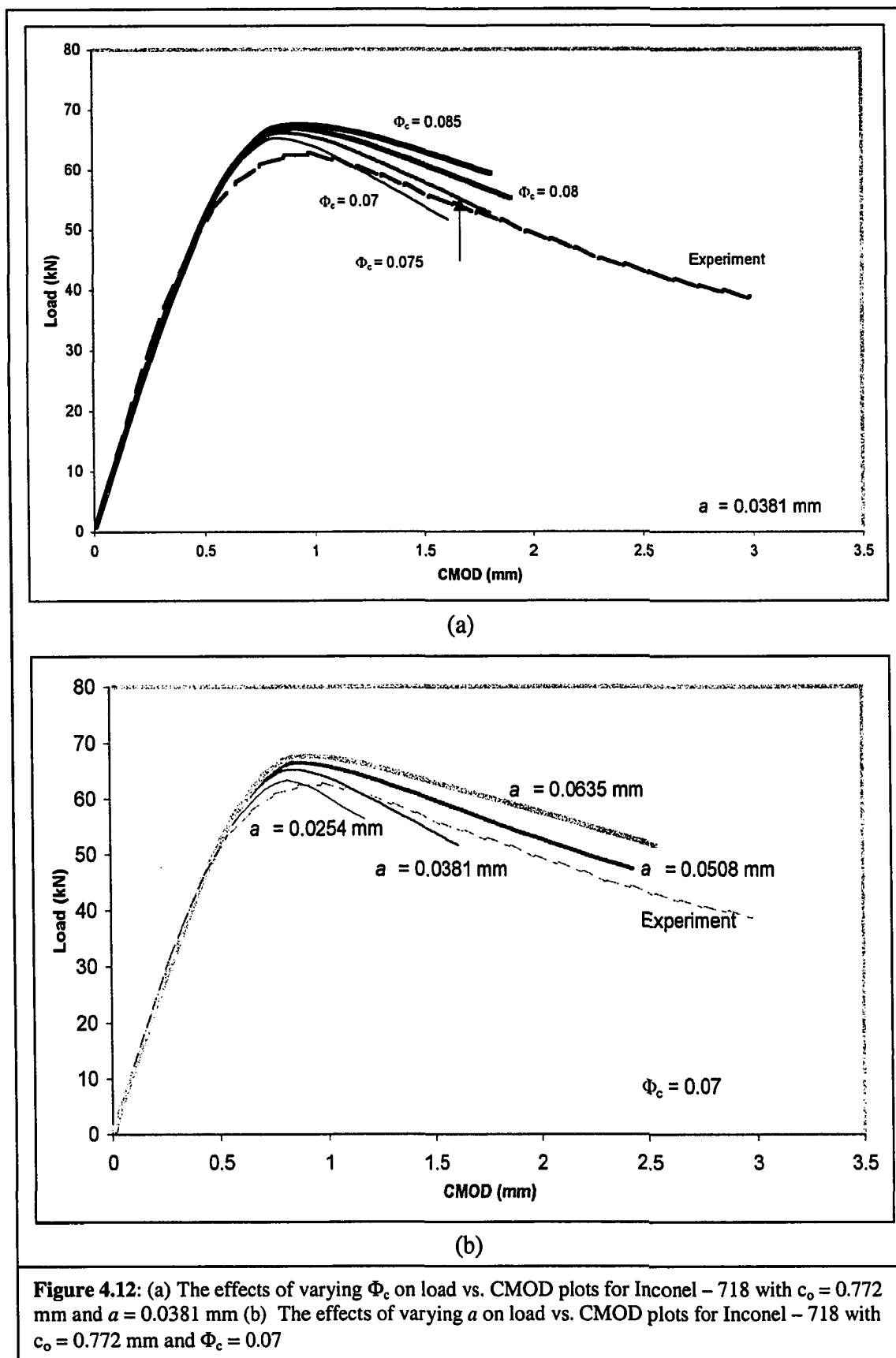


Figure 4.12: (a) The effects of varying Φ_c on load vs. CMOD plots for Inconel - 718 with $c_o = 0.772 \text{ mm}$ and $a = 0.0381 \text{ mm}$ (b) The effects of varying a on load vs. CMOD plots for Inconel - 718 with $c_o = 0.772 \text{ mm}$ and $\Phi_c = 0.07$

- (1) In the case of constant ER radius, the curves on each plot remain coincident up to loads as high as 63 kN.
- (2) For constant Φ_c , the curves begin diverging as early as 54 kN.
- (3) For all plots, higher ER radius and Φ_c magnitudes result in higher peak loads and flatter curves after the peak load.
- (4) In comparison with variations in the Φ_c magnitude, deviations in the ER values appear to lead to greater variations in the peak values and to a larger divergence of the curves after the peak loads are reached.
- (5) There exists a curve on each plot that appears to be the closest match to the experimental curve. The Φ_c and the ER radius combinations for these curves are $\{(\Phi_c = 0.085, a = 0.0254 \text{ mm}), (\Phi_c = 0.080, a = 0.0381 \text{ mm}), (\Phi_c = 0.07, a = 0.0508 \text{ mm}), (\Phi_c = 0.065 \text{ and } a = 0.0635 \text{ mm})\}$, and result in no duplication of either parameter.

The above observations begin to shed light upon the influence of Φ_c and a . However, as pointed out in Observation 3 above, both parameters appear to affect the curve in similar ways, which presents a challenge in distinguishing the separate effects of each parameter from the load vs. CMOD plots alone. Therefore specific information was collected from the completed simulations, with Φ_c and the ER radius values within the suggested ranges. Key factors such as the load at which crack begins to extend, P_{fracture} ; the peak load the specimen can withstand, P_{max} ; the amount of crack extension prior to reaching the peak load; and the percent increase in the load between P_{fracture} and P_{max} were tabulated for 22 simulations and are presented in Tables 4.3 and 4.4. As more simulations within the

identified ranges were completed for $c_o = 19.61$ mm than for $c_o = 19.18$ mm, the development of the effects of Φ_c and the ER radius will henceforth focus on the $c_o = 19.61$ mm initial crack tip depth, with verification with the second c_o value to follow. Table 4.3 is grouped by ER radii to allow for the comparison of the influence of Φ_c . Table 4.4 is grouped by the Φ_c value

As can be seen in Table 4.3, both $P_{fracture}$ and P_{max} increase with Φ_c . The two "% diff from 0.07" columns record the percent increase or decrease of $P_{fracture}$ and P_{max} with respect to magnitudes found at $\Phi_c = 0.07$. An interesting result was the consistency of the increase in $P_{fracture}$ for each Φ_c value regardless of the ER radius. For example, increasing the Φ_c from 0.07 to 0.08 increased the $P_{fracture}$ by 6.24% for an ER radius of 0.0635mm, and 6.98% when the ER radius was 0.0508 mm. The difference was only 0.04% when comparing the 0.0381 mm and 0.0508 mm radii. The P_{max} magnitudes were also seen to increase with Φ_c . However, the percentage of increase does not maintain the same consistency and decreases with rising ER radius. Note also that, as the magnitude of P_{max} rises with an increasing Φ_c , the amount of crack extension prior to reaching P_{max} decreases. A final result worth noting can be seen in the last column of the table, which shows the percent increase of load above $P_{fracture}$ to attain P_{max} . Each increase in Φ_c of 0.05 resulted in a decrease in the percent difference by 3 to 4 % regardless of the ER radius. Therefore, as Φ_c increased, $P_{fracture}$ experienced greater increases in magnitude than did the corresponding P_{max} .

Now turning to Table 4.4, similar effects to those seen in Table 4.3 appear to occur with

changes in the ER radius, but with much greater magnitudes. In looking at the P_{fracture} column, the magnitude of the ER radius greatly influenced the load at fracture, which provides an explanation for the early divergence seen in the curves of 4.12(b). For example, in reference to the load determined at an ER radius of 0.0254 mm, there were increases in P_{fracture} of over 22% between an ER of 0.0254 and 0.0381 mm. The magnitude of this percent increase remained consistent between each Φ_c . Specifically, for the five Φ_c values ranging from 0.07 to 0.09, the percent increase varies between 22.27% and 22.35%, a range of only 0.08%. As with Table 4.3, P_{max} values increased with each larger ER radius but the magnitude of this increase also decreased with rising Φ_c values. Again, the amount of crack extension at P_{max} was observed to decrease as the ER radius was incremented upward. It should also be noted that the magnitude of the percent increase of P_{max} for each ER radius is only slightly higher than those in Table 4.3. Therefore, the ER radius has considerable influence on the magnitude of P_{fracture} , but only modest effects on P_{max} . This is readily seen in the percent increase of the applied load between P_{fracture} and P_{max} as shown in the last column of Table 4.4. The percentages drop as much as 24% between two consecutive ER values.

From the above observations, the following conclusions in regard to the effects of Φ_c and the ER radius on the computer simulations of the Inconel 718 were made.

- (1) Both Φ_c and the ER radius independently affect the magnitude of P_{fracture} , as is evidenced in the consistency by which each parameter influenced the load at fracture regardless of the value of the other parameter.
- (2) Small increases in the ER radius lead to significant increases in the value of

P_{fracture} , which indicates more extensive plastic deformations are occurring. This result is a direct consequence of the current form of the fracture criterion, which is found as a function of the average plastic strain in the ER. Given that the magnitude of the plastic strain decreases as you move away from the crack tip, the average plastic strain in the ER will decrease as the ER radius is increased. Therefore, if the ER radius is increased, the size of the plastic zone, and hence the load at fracture, must increase before the average plastic strain found in the ER will reach a given value of the critical separation criterion Φ_c .

- (3) The increase in P_{max} with the corresponding increase in either Φ_c or a indicates rising plasticity in the near-tip region. This occurred in similar magnitudes for both parameters, indicating they both influence the plasticity in the near-tip region. However, the influence of both parameters (Φ_c and a) varied with the value of the other parameter. Therefore, it appears that once crack growth initiates, the effect of Φ_c and the ER radius demonstrate interdependence.

With these observations in hand, it is useful to return to the load vs. CMOD plots. As previously mentioned, there were four combinations of Φ_c and the ER radius that provided the best fits to the experimental curve. Plots of each combination, taken to 92 load steps, are shown in Figure 4.13. While the curves are very similar in shape, slight variations are apparent in the peak loads and in the final curve slopes. The initial shapes of each curve in the region of the peak load are too similar to make any judgments regarding the appropriateness of one set of parameters over another. However, careful review of the plot shows undesirable slopes in the latter half of the curve for two

parameter sets. Specifically, when $\Phi_c = 0.085$ and $a = 0.0254$ mm the latter part of the curve begins to diverge from the experimental slope. Similarly, when $\Phi_c = 0.065$ and $a = 0.0635$ mm, the curve begins to slope toward the experimental data near 1.6 mm of CMOD. The remaining combinations both maintain consistent parallel slopes with the experimental data. Of the two, the combination of $\Phi_c = 0.07$ and $a = 0.0508$ mm offers a slight improvement on matching the magnitude of the experimental loads.

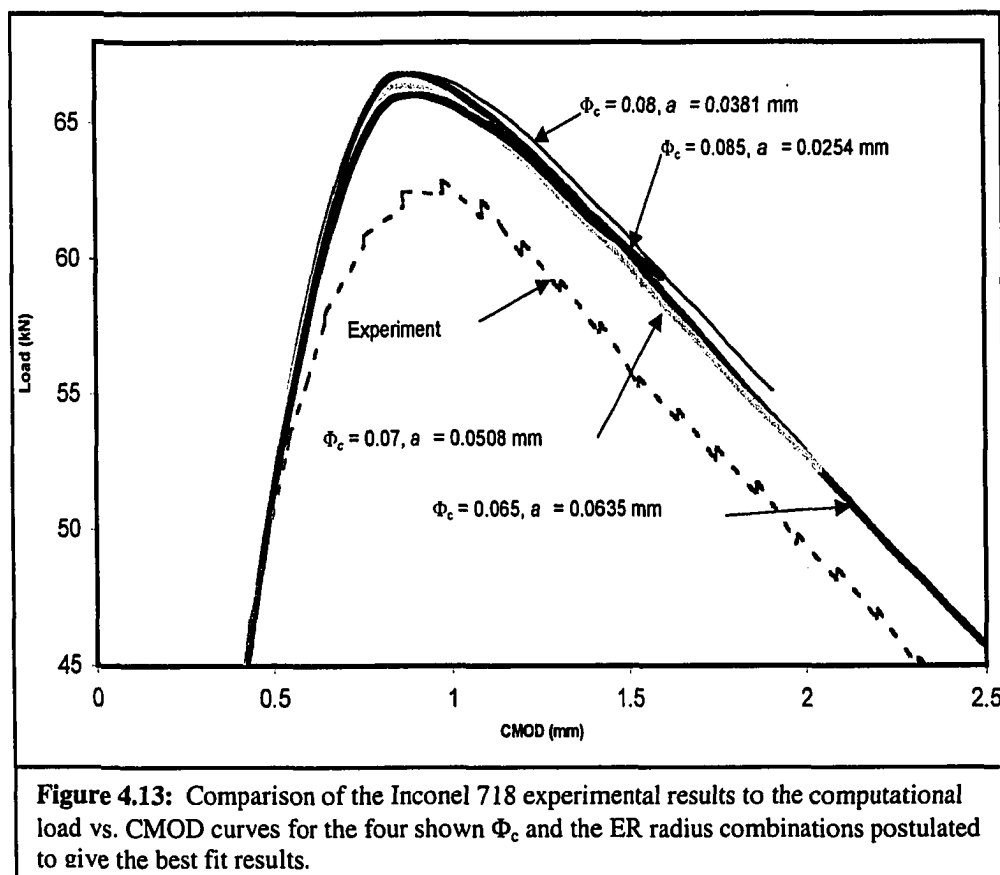


Figure 4.13: Comparison of the Inconel 718 experimental results to the computational load vs. CMOD curves for the four shown Φ_c and the ER radius combinations postulated to give the best fit results.

A further comparison of these four combinations is given by considering the P_{max} and $P_{fracture}$ data for each simulation (see Table 4.5). The maximum change in the peak load between all cases is only 1.21%. Additionally, the crack length when the peak load is reached is also virtually identical. Recall that each simulation involves an increment of

$c_o = 19.61 \text{ mm}$		P_{fracture} (kN)	% diff	P_{max} (kN)	% diff	Δc at P_{max} (mm)	P_{max} as a % of P_{fracture}
$a = 0.0254$	$\Phi_c = 0.085$	32.09	0.00%	65.64	0.00%	0.6706	204.57%
$a = 0.0381$	$\Phi_c = 0.08$	38.11	18.77%	66.44	1.21%	0.6096	174.32%
$a = 0.0508$	$\Phi_c = 0.07$	40.96	27.65%	66.00	0.53%	0.5867	161.12%
$a = 0.0635$	$\Phi_c = 0.065$	44.06	37.31%	66.42	1.18%	0.5283	150.74%

$c_o = 19.18 \text{ mm}$		P_{fracture} (kN)	% diff	P_{max} (kN)	% diff	Δc at P_{max} (mm)	P_{max} as a % of P_{fracture}
$a = 0.0254$	$\Phi_c = 0.085$	33.26	0.00%	68.51	0.00%	0.2705	205.99%
$a = 0.0381$	$\Phi_c = 0.08$	39.48	18.69%	69.34	1.21%	0.2224	175.65%
$a = 0.0508$	$\Phi_c = 0.07$	42.49	27.76%	68.71	0.29%	0.1587	161.70%
$a = 0.0635$	$\Phi_c = 0.065$	45.66	37.30%	69.35	1.23%	0.1664	151.88%

Table 4.5: Variations in P_{fracture} and P_{max} for the four best-fit Φ_c and ER radius combinations

crack growth of 0.00254 mm larger than the a value. Therefore, it would be impossible for the crack lengths to exactly match. The significant observation lies in the magnitude of the load at crack growth initiation. These values vary as much as 37% between the simulations. If the magnitude of the load at which the crack growth initiates can be determined experimentally, it would offer an additional guide by which to choose the most appropriate Φ_c and ER radius values. A discussion of load vs. crack length comparisons is presented later in this chapter.

Before discussing attempts at further calibration of Φ_c and the ER radius, it is appropriate to consider variations in the results for the two trial initial crack tip locations. Figure 4.14 compares the load vs. CMOD curves for the two c_o values at the four Φ_c and a combinations presented in Table 4.5. Individual plots for each Φ_c and ER radius set are provided in the Appendix A, Figures A.13 – A.16. The curves are remarkably similar in shape, suggesting the effect of Φ_c and the ER radius on the curve shape is not influenced by the slight variation in the geometry. Table 4.5 tabulates the P_{fracture} and P_{max} values for

each simulation.

Although the peak loads between the two geometries vary by as much as 3 kN, the consistency of the percent difference between the parameter combinations would

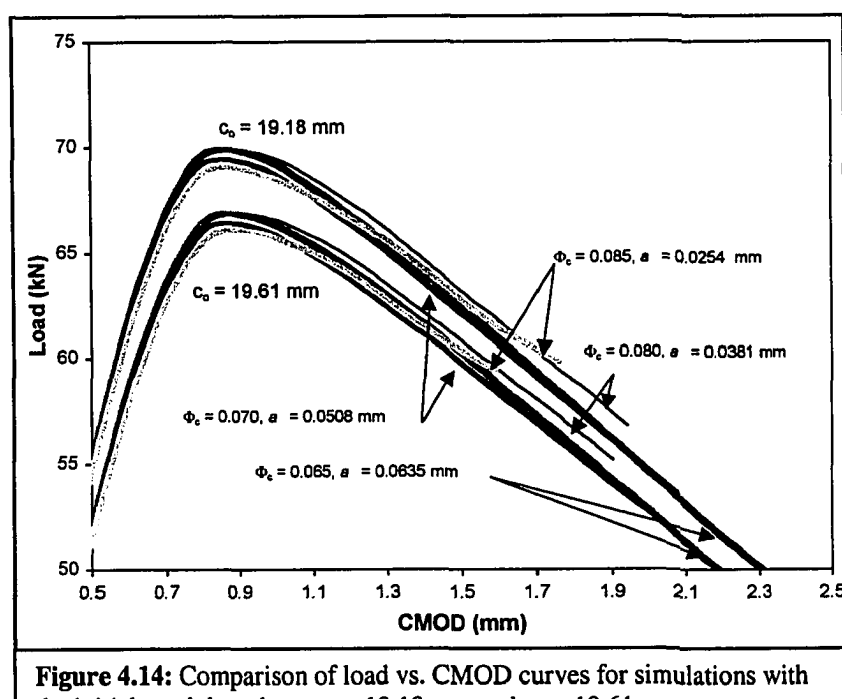


Figure 4.14: Comparison of load vs. CMOD curves for simulations with the initial crack lengths at $c_0 = 19.18 \text{ mm}$ and $c_0 = 19.61 \text{ mm}$

also indicate the small variation in the geometry is not affecting the manner in which Φ_c and the ER radius influence the load magnitudes and crack lengths.

4.4.b Comparison of Computer Simulated Crack Lengths to Experimental Data

Turning now to the crack length at P_{\max} and the magnitude of P_{fracture} , Figure 4.15 shows the experimental load versus crack length as calculated by the ASTM elastic unloading compliance method for the 3-point bend geometry described in Chapter 3. It should be noted that this method has been found to be an unreliable measure of crack extension, especially in the early stages of crack growth (Hill and Panontin 2002, Joyce 1992). Due to the inherent approximations in the elastic unloading compliance method, exact matches between experimental and theoretical data points were not expected. From Figure 4.15, it appears that the crack experiences very little crack growth prior to

reaching the peak load. Crack growth appears to initiate near the seventh data point at $c = 19.21$ mm and $P_{\text{fracture}} = 60.7$ kN. The peak load of $P_{\text{max}} = 62.9$ kN is then quickly reached at $c = 19.45$ mm. Due to the uncertainty in the determination of the

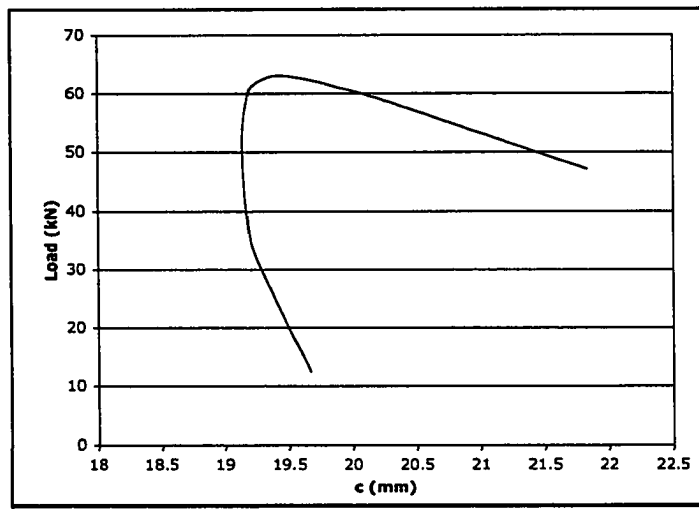


Figure 4.15: Experimental load vs. crack length curve for Inconel 718

experimental crack length values as discussed above, these values should not be used with the load at fracture data in Table 4.5 as an exact indicator of the appropriate Φ_c and a combination.

From the crack length data we can study the general trends of the experimental data and compare these with the four preferred parameter sets. Figure 4.16(a) presents load versus crack length, c , curves, and Figure 4.16(b) presents CMOD versus c data. In the case of load vs. c , the large range of crack growth prior to reaching the peak load for the theoretical data is readily apparent. The lowest curve on plot 4.16(a), with the correspondingly largest radius of curvature, corresponds to $\Phi_c = 0.085$ with $a = 0.0254$ mm, and, as already stated, exhibits the earliest crack initiation. The upper curve, with the smallest radius, must therefore be $\Phi_c = 0.065$ and $a = 0.0635$ mm. The behavior of the two intermediate curves is interesting. In the lower half of the curve, $\Phi_c = 0.08$ with $a = 0.0381$ mm has a larger radius of curvature. Then, at approximately 14000 lbs, the

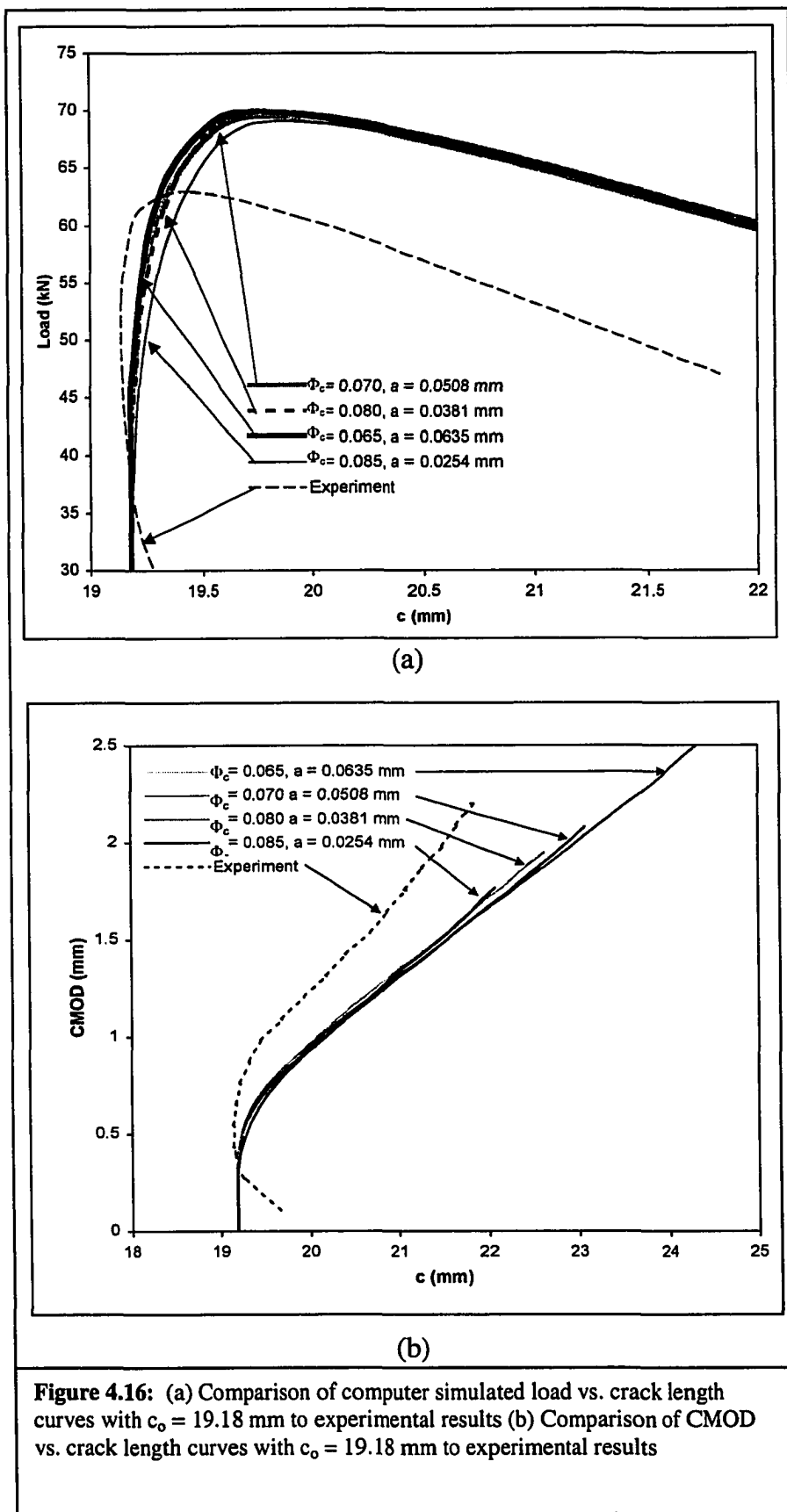


Figure 4.16: (a) Comparison of computer simulated load vs. crack length curves with $c_o = 19.18 \text{ mm}$ to experimental results (b) Comparison of CMOD vs. crack length curves with $c_o = 19.18 \text{ mm}$ to experimental results

paths of the two curves cross and the $\Phi_c = 0.08$ with $a = 0.0381$ mm curve continues to rise until it crosses the upper curve at approximately 19.94 mm. In the latter portion of the plot, the behavior between the four parameter sets is practically identical, and all curves continue at a slope that is slightly shallower than the experimental data. Therefore, in the lower half of the curve, none of the Φ_c - a combinations provide a superior approximation of the experimental data.

The plot in Figure 4.16(b) again shows the consistency in the theoretical data. The experimental data exhibits less crack growth at the same amount of CMOD than any of the theoretical curves; however, the basic shapes of the curves are satisfactorily similar, with $\Phi_c = 0.085$ with $a = 0.0254$ mm presenting a slightly improved approximation over the other curves. In both plots, it would appear that, without accurate values for experimental crack length data, the theoretical curves are too similar to make any judgments on the appropriateness of any Φ_c or a magnitude.

4.5 Application of the Material Parameters to Plane Stress

The ability of ER theory, with the present plastic-strain based fracture criterion, to effectively model the experimental data under plane strain conditions is indicated in Figure 4.13. As is evident in this figure, the simulations over-predict the peak experimental load by approximately 5%. An exact determination of a specific parameter or assumption in the modeling process that is the cause of this over-prediction presents a significant challenge.

As stated earlier, the fracture criterion is based on the plastic strain in the near-tip region. It appears that the fracture model is underestimating the plastic strain in the near-tip region, which is resulting in the need for additional load accumulation to initiate crack extension. Determining what modeling characteristics lead to this lower plastic strain presents the difficulty. Two distinct, yet connected, factors appear to be influencing the computational model's ability to predict the experimental reality. The first is the difference between the three dimensional reality of the experimental specimen in comparison to the plane strain modeling condition. The hydrostatic stress state, along with the amount of plastic flow, will not be perfectly consistent between the experiment and a plane strain representation. The second factor is the dependence of the assumed fracture criterion on the hydrostatic stress state and the amount of plastic flow. Whereas, it is known that ductile fracture is promoted by high hydrostatic tension, the present fracture model did not directly include a measure of hydrostatic stress. In other words, both the accuracy of the model's representation of these two quantities and the accurate representation of their effects, greatly influence the overall fidelity of the model.

A fracture criterion that accurately incorporates the effects of the hydrostatic stress state and the amount of plastic flow on crack extension should extend to a plane stress situation. Conventional wisdom in fracture mechanics (Anderson 1995, Dowling 1999) requires that a plane stress analysis using material parameters within the proposed ranges presented in Section 4.4 should result in higher peak loads than the plane strain simulation. This is due to the variation in the hydrostatic tensile stress in the near-tip region between a plane stress and plane strain analysis. In the case of plane strain, the

hydrostatic stresses that develop are significantly higher than those in a plane stress condition due to the high constraint conditions of the plane strain specimens. It should be noted that ‘in-plane’ geometric features as well as loading and residual stresses (Hill and Panontin 2002) can also influence the amount of constraint and hence the magnitude of hydrostatic tensile stress. Larger hydrostatic tensile stresses in the near-tip region accelerate the void coalescence process, which leads to fracture occurring at lower loads than in the case of plane stress or low constraint.

To investigate whether or not the fracture model employed in this research reflects the expected trends, some analyses were re-run with the plane stress assumption. Figure 4.17

shows the results of two plane-stress analyses using material parameters within the ranges recommended in Section 4.4.a. As can be seen in this figure, the plane stress loads are significantly lower than the experimental results, which would indicate an inability of the fracture criterion to

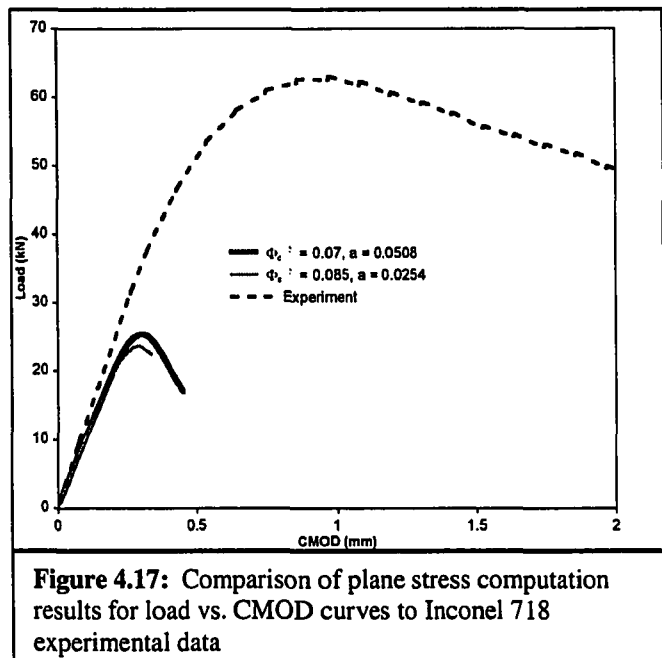


Figure 4.17: Comparison of plane stress computation results for load vs. CMOD curves to Inconel 718 experimental data

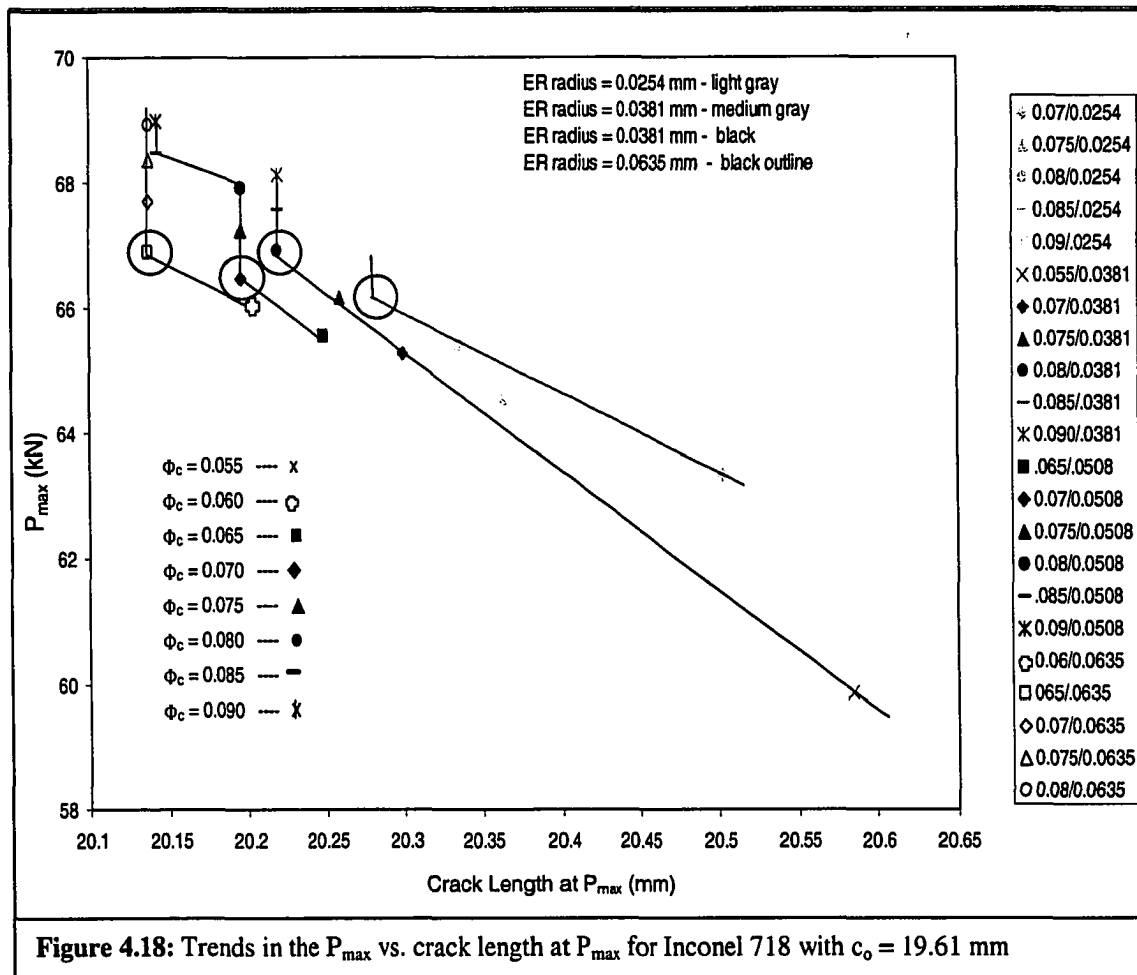
capture the three-dimensional effects that occur during crack growth. The unrealistic load magnitudes of the plane stress analysis are a direct result of the proposed plastic-strain-based fracture criterion. As is well known in fracture mechanics, the plane stress plastic zone size is larger than the plastic zone in plane strain conditions (Dowling 1999,

Anderson 1995). This additional plastic deformation predicted in the plane stress analysis will result in a larger average plastic strain in the Exclusion Region when compared to a plane strain analysis for the same specimen geometry and material parameters. As such, the critical separation criterion implemented in this research will be met at loads of lesser magnitude in the plane stress conditions than those required for a plane strain analysis. Therefore, although the fracture criterion appears reasonable for use in modeling crack growth for plane strain conditions, additional efforts are necessary to extend the criterion to three-dimensional behavior.

4.6 A Possible Indicator of Unique Φ_c and ER radius values

Before discussing any final conclusions that can be drawn from the above calibration work, an interesting and unexpected trend in the peak load vs. crack length at peak load data is presented for the plane strain calculations. Figure 4.18 shows a plot of P_{max} with its corresponding crack length for 22 simulations with $c_0 = 19.61$ mm. The plot is organized such that a specific symbol represents the Φ_c magnitude used in determining the given data point, e.g. all data points calculated with $\Phi_c = 0.065$ are depicted by squares, ■. The value of the ER radius is indicated by the color of the symbol, e.g. light gray for 0.0254 mm and black outline for 0.0635 mm. The first trend observed was the piecewise linearity of the data within each ER radius grouping. With the exception of one point in the ER = 0.0254 mm group, all the data points follow this trend. Consistency in the manner in which the crack length increases is to be expected, since the computer simulation specifies a specific crack-advance increment for each load step. Recall this increment was defined as 0.00254 mm larger than the given ER radius for

these analyses. However, there is nothing inherent in the model to suggest the magnitude of the peak load at fracture would result in piecewise linear increases in the peak load. The data points determined with $a = 0.0381$ mm offer the best example of this trend.



A second trend observed in each ER radius group was the temporary stabilization of the crack length, to a specific value, for varying magnitudes of P_{\max} . It is anticipated that there would actually be some scatter in these values if the crack length increments were not uniform. It is interesting to observe that the Φ_c-a combinations used in the calculations of the circled data points were the same four Φ_c and ER radius combinations that provided the best matches to the experimental data. While no firm conclusions can

be drawn from these observations without further experimental studies, it would be of interest to look for similar trends in plane strain simulations with other materials.

Chapter 5 - Conclusions

5.1 Observations and Conclusions

With the completion of the above-discussed comparative study, a number of conclusions and observations can be made regarding the Exclusion Region theory and the proposed material parameters, Φ_c and the ER radius. Early difficulties in modeling the 2024 Aluminum raised questions regarding the appropriateness of the constitutive model in relation to fracture, the chosen separation criterion, and the ER fracture theory itself. The apparent success in modeling the fracture behavior of the Inconel 718 specimens tend to support the hypothesis that the modeling difficulties lay in the constitutive model for 2024 Aluminum and are not inherent to the ER theory. Further simulations with other ductile materials are needed to investigate this line of reasoning.

Four possible magnitudes for the critical value of the separation criterion were established for the plane strain analysis, along with four corresponding possible ER radii. Although these parameters appear to work in sets of Φ_c and a , both parameters, as discussed in Section 4.4.a, independently affect the theoretical fracture behavior. It may be concluded that one value of Φ_c provides the best fit for a specific value of a . Indeed, consider the consequences if this were not true: Suppose that two computer simulations were completed using the same ER radius but different Φ_c values, and that these simulations resulted in curves of similar consistency to those seen in Figure 4.13. This

would indicate that the modified parameter, in this case Φ_c , had no independent effect on the theoretical fracture behavior, which has been seen to be untrue. However, it can also be argued that additional combinations of Φ_c and a would also provide satisfactory matches to the experimental load vs. CMOD curve. For example, following the trends of parameter sets in Table 4.5, $\Phi_c = 0.06$ with $a = 0.0762$ mm or $\Phi_c = 0.09$ and $a = 0.0127$ mm would be logical candidates. However, the value of P_{fracture} for $a = 0.0254$ mm is already quite low. Reducing the ER radius further would result in unrealistically low loads at crack growth initiation. Conversely, continual escalation of the ER radius will result in P_{fracture} values that barely differ from P_{max} , a behavior that would not be expected in ductile fracture. The rationale for bounding the ER radius between 0.0254 and 0.0635 mm and Φ_c between 0.09 and 0.065 is also evident in Figure 4.13 and Appendix A, Figures A.13 – A.16. While the curves for $\Phi_c = 0.085$ with $a = 0.0254$ mm and $\Phi_c = 0.065$ with $a = 0.0635$ mm provide excellent matches to the shape of the experimental curve in the area of the peak load, the former curve begins to move away from the experimental data in the bottom half of the plot, and the latter curve slowly slopes toward the experimental curve. This observation, along with the magnitudes of P_{fracture} for the two parameter sets at the extreme ends of the given ranges, lead to the conclusion that the proposed bounds on the values of Φ_c and the ER radius are within reasonable ranges.

Taking the above observations on the proposed bounds one step farther, it is suggested that a more accurate range for the ER radius would be 0.0381 to 0.0508 mm and, correspondingly, 0.07 to 0.08 for the critical value of the separation function. Figure 4.19 shows a comparison of these two curves with the experimental data. The plot

demonstrates that both curves remain parallel to the experimental data and to each other. The $\Phi_c = 0.07$ with $a = 0.0254$ mm curve does provide better agreement with the magnitude of the experimental data loads. However, without further experimental results it is difficult to justify either parameter set.

Although values for the critical value of the separation function, Φ_c , and the radius of the Exclusion Region, a , were not given exactly, the above research established that the

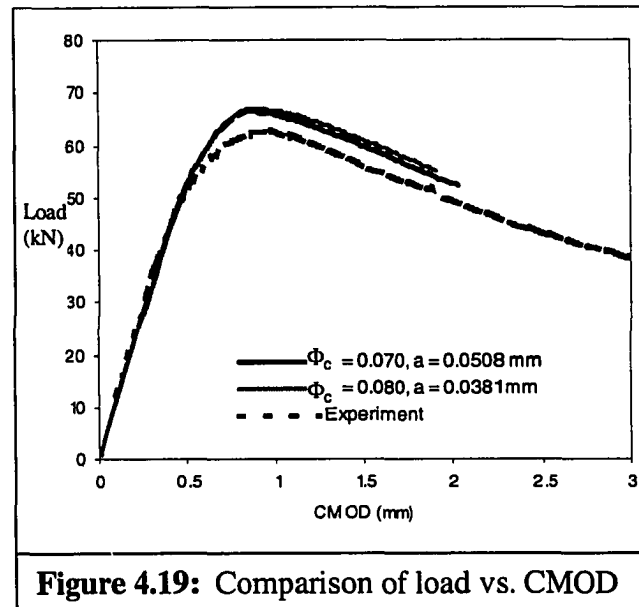


Figure 4.19: Comparison of load vs. CMOD for $\Phi_c = 0.07$ with $a = 0.0508$ mm and $\Phi_c = 0.08$ with $a = 0.0381$ mm with $c_o = 19.61$ mm to experimental data

Exclusion Region fracture theory, with the separation criterion based on the average plastic strain within the ER, is a viable tool for modeling ductile crack growth under plane strain conditions. The proposed material properties, Φ_c and a , were both shown to independently influence the plasticity in the near-tip region of the crack. The range of the proposed ER values from 38 to 51 microns are reasonable values to support the argument of the ER radius as a length scale parameter related to a ductile “process zone”, which has been presented in the literature to have a size of 10^{-4} m (Xia and Shih 1995a). The nearly identical nature of the load vs. CMOD curves when comparing computational results for the two initial crack depths (Figure 4.14 and Table 4.5) suggests, as postulated, the effects of Φ_c and the ER radius are independent of the specimen geometry. However, since it has been shown that the fracture criterion currently implemented with the ER

theory does not accurately account for the three dimensional effects, additional work is required to verify that these parameters' applicability will extend beyond plane strain simulations.

5.2 Suggested Directions of Future Work

It is apparent that an important direction for future work is the extension of the current plastic-strain-based fracture criterion to include the effects of constraint. The plastic strain in the near-tip region is undoubtedly an important indicator of the material state at the crack tip, as it relates to fracture. However, the hydrostatic tensile stress can also significantly affect ductile crack growth, and should be included in the fracture criterion. A suggested direction for a new fracture criterion would be to formulate a damage parameter D. The magnitude of this parameter would accumulate with plastic strain. However, the rate of accumulation would vary as a function of the hydrostatic stress state. For example:

$$\dot{D} = f\left(\frac{\langle P \rangle}{J_2}\right)\dot{\epsilon}_p \quad (\text{EQ 5.1})$$

where P is the hydrostatic stress, J₂ is the second invariant of the deviatoric stress, $\dot{\epsilon}_p$ is the rate of accumulation of the plastic strain, and f(·) is an increasing function. The Macaulay brackets, ⟨ ⟩, are used to ensure that the damage parameter accumulates only when the hydrostatic stress is positive. The form of the separation criterion Φ would parallel the current fracture criterion defined in EQ 2.4. However, the plastic strain value would be replaced with D, such that Φ would depend on the average value of the damage parameter within the ER:

$$\Phi(\psi) = \frac{1}{A_{ER}} \int D dA \cdot \left(\frac{\langle F_n(\psi) \rangle}{F_{n_{MAX}}} \right) \quad (\text{EQ 5.2})$$

As can be seen in EQ 5.2, the fracture criterion would still be maximized in the direction perpendicular to the maximum normal force on the ER boundary.

The incorporation of a fracture criterion that is capable of including the effects of stress triaxiality, such as the one suggested above, in the Exclusion Region theory and the FEFRAC framework, would allow for additional calibration of the Φ_c and a parameters. Further conclusions regarding Φ_c and a for the Inconel 718 material, and the ER fracture theory in general, cannot be made without additional model calibrations with other experimental data. To determine if the reduced ranges of 0.07 to 0.08 for Φ_c and 0.0381 mm to 0.0508 mm for a are valid for Inconel 718, additional experimental fracture tests are required. The compact tension, CT, specimen geometry would provide an interesting test for the proposed ranges of Φ_c and the ER radius, as the CT specimens offer very different geometries and constraint conditions than do the three-point bend specimens. Additional three-point bend specimen tests, which mirror the variations in the geometry and loading used in the 2024 Aluminum fracture tests are also suggested. As these tests would include the additional challenges of arbitrary crack paths and thickness variations, they would provide useful calibration data.

Further validation of the Exclusion Region theory would require computational modeling of an entirely different material. Successful comparison to fracture tests of a second ductile material that is characterized by J_2 elastic-plastic flow theory would further

support the use of the ER theory as a viable modeling tool for nonlinear fracture mechanics. To the same end, development of a local constitutive model to accurately describe the nonlinear fracture behavior of 2024 Aluminum would result in a test of the robustness of the ER theory to accurately predict fracture for materials characterized by various constitutive models. Once calibration of the fracture-related material parameters was completed for the 2024 Aluminum, the numerous variations in the experimental geometry and loading for the 2024 Aluminum as described in Chapter 3, would allow for additionally testing of Φ_c and the ER radius as geometry independent parameters.

The implementation of a fracture criterion that can represent the effects of the stress triaxiality at the crack tip would allow for the determination of values of Φ_c and the ER radius for any experimental geometry, without the limitation of plane strain simulations. Combined with additional experimental results for multiple geometries, such a criterion would allow for the verification of the relevant Φ_c and a values as geometry independent material parameters.

Bibliography

- Al-Ani, A.M.; Hancock, J.W., 1991, "J-Dominance of Short Cracks in Tension and Bending", *Journal of Mechanics and Physics of Solids*, Vol. 39, pp. 23 – 43
- Anderson, T.L., 1995, *Fracture Mechanics, Fundamentals and Applications*, CRC Press
- Barrenblatt, G.I., 1962, "The Mathematical Theory of Equilibrium of Cracks in Brittle Fracture", *Advances in Applied Mechanics*, Vol. 7, p. 55-129
- Belytschko, T.; Lu, Y.Y.; Gu, L.; Tabbara, M., 1995, "Element-Free Galerkin Methods for Static and Dynamic Fracture", *International Journal of Solids and Structures*, Vol. 32, pp. 2547 – 2570
- Belytschko, T.; Lu, Y.Y.; Gu, L., 1994, "Element-Free Galerkin Methods", *International Journal of Numerical Methods in Engineering*, Vol. 37, pp. 229 – 256
- Betegón, C.; Hancock, J.W., 1991, "Two Parameter Characterization of Elastic-Plastic Crack-Tip Fields", *Journal of Applied Mechanics*, Vol. 58, pp. 104 – 110
- Bittencourt, T.N.; Wawrynek, P.A.; Ingraffea, A.R.; Sousa, J.L, 1996, "Quasi-Automatic Simulation of Crack Propagation for 2D LEFM Problems", *Engineering Fracture Mechanics*, Vol. 55, No. 2, pp. 321 - 334
- Brocks, W.; Sun, D.Z.; Hönig, A., 1996, "Verification of Micromechanical Models for Ductile Fracture by Cell Model Calculations", *Computational Materials Science*, Vol 7, pp. 235 – 241
- Camacho, G.T.; Ortiz, M., 1996, "Computational Modeling of Impact Damage in Brittle Materials", *International Journal of Solids and Structures*, Vol. 33., No. 20-22, pp. 2899 – 2938
- Cotterell, B. & Kaminga, J., 1990, *Mechanics of Pre-Industrial Technology*, Cambridge University Press,
- de-Andrés; A., Pérez, J.L.; Ortiz, M., 1999, "Elastoplastic Finite Element Analysis of Three-Dimensional Fatigue Crack Growth in Aluminum Shafts subject to Axial Loading", *International Journal of Solids and Structures*, Vol. 36, pp. 2231-2258
- DeBartolo, B., (2002), Personal Correspondence

- Dolbow, J.; Moës, N.; Belytschko, T., 2001, "An Extended Finite Element Method for Modeling Crack Growth with Frictional Contact", *Computer Methods in Applied Mechanics and Engineering*, Vol. 19, pp. 6825-6846
- Dowling, N.E., 1999, *Mechanical Behavior of Materials, Engineering Methods for Deformation, Fracture and Fatigue*, Prentice Hall, 2nd Ed.,
- Du, Z.Z.; Hancock, J.W., 1991, "The Effect of Non-Singular Stresses on Crack-Tip Constraint", *Journal of Mechanics and Physics of Solids*, Vol. 39, pp. 555 – 567
- Dugdale, D.S., 1960, "Yielding of Steel Sheets Containing Slits", *Journal of Mechanics and Physics of Solids*, Vol. 8, pp. 100 – 104
- Everhart, J.L., 1971, *Engineering Properties of Nickel and Nickel Alloys*, Plenum Press
- Fleming, M.; Chu, Y.A.; Moran, B.; Belytschko, T., 1997, "Enriched Element-Free Galerkin Methods for Crack Tip Fields", *International Journal for Numerical Methods in Engineering*, Vol. 40, No. 8, pp. 1483 - 1504
- Galvez, J.; Elices, M.; Guinea, G.V.; Planas, J., 1996, "Crack Trajectories Under Mixed Mode and Non-Proportional Loading", *International Journal of Fracture*, Vol. 81, pp. 171 - 193
- Gao, X.; Faleskog, J.; Shih, C.F.; 1998, "Ductile Tearing in Part-Through Cracks: Experiments and Cell-Model Predictions", *Engineering Fracture Mechanics*, Vol. 59, No. 6, pp. 761 - 777
- Griffith, A.A., 1920, "The Phenomena of Rupture and Flow in Solids", *Philosophical Transactions, Series A*, Vol. 221, pp. 163 – 198
- Gurson, A.L., 1977, "Continuum Theory of Ductile Rupture by Void Nucleation and Growth –I. Yield Criteria and Flow Rules for Porous Ductile Media", *Journal of Engineering Materials Technology*", Vol. 99, pp 2-15
- Henry, B.S.; Luxmoore, A.R., 1997, "The Stress Triaxiality Constraint and the Q-Value as a Ductile Fracture Parameter", *Engineering Fracture Mechanics*, Vo. 57, No.4, pp. 375 – 390
- Hill, M.R., 2002, Personal Correspondence
- Hill, M.R. & Panontin, T.L., 2002, "Micromechanical Modeling of Fracture Initiation in 7050 Aluminum", *Engineering Fracture Mechanics*, Article in Press
- Irwin, G.R., 1957, "Analysis of Stresses and Strains near the End of a Crack Traversing a Plate", *Journal of Applied Mechanics*, Vol. 24, September, pp. 361 -364

- Irwin, G.R., 1956, "Onset of Fast Crack Propagation in High Strength Steel and Aluminum Alloys", *Sagamore Research Conference Proceedings*, Vol. 2, pp. 289 - 305
- Joyce, J.A., 1992, "J-Resistance Curve Testing of Short Crack Bend Specimens Using Unloading Compliance", *Fracture Mechanics: Twenty-Second Symposium*, ASTM STP 1131, Vol. I American Society for Testing Materials, pp. 904-24
- Komori, K., "Proposal and Use of a Void Model for the Simulation of Ductile Fracture Behavior", *Acta Materialia* Vol. 47, No. 10, 1999, pp. 3069 – 3077
- Koppenhoefer, K.C.; Dodds, R.H. Jr., 1998, "Ductile Crack Growth in Pre-Cracked CVN Specimens: Numerical Studies", *Nuclear Engineering and Design*, Vol. 180, pp. 221 - 241
- Larsson, S.G; Carlsson, A.J., 1973, "Influence of Non-Singular Stress Terms and Specimen Geometry on Small-Scale Yielding at Crack-Tips in Elastic-Plastic Materials", *Journal of Mechanics and Physics of Solids*, Vol. 21, pp. 263 - 278
- Lynch, C.T., 1975, *Handbook of Materials Science, Volume II: Metals, Composites, and Refractory Materials*, CRC Press
- Mackenzie, A.C.; Hancock, J.W.; Brown, D.K., 1977, "On the Influence of State of Stress on Ductile Fracture Initiation in High Strength Steels", *Engineering Fracture Mechanics*, Vol. 9, No. 1, pp. 167 – 188
- Malluck, J.F.; King, W.W., 1978, "Fast Fracture Simulated by Finite-Element Analysis Which Accounts for Crack-Tip Energy Dissipation", *Numerical Methods in Fracture Mechanics*, A.R. Luxmoore and D.R.J Owen, Eds., University College, Swansea, pp. 548 - 659
- Moës, N.; Dolbow, J.; Belytschko, T., 1999, "A Finite Element Method for Crack Growth without Remeshing", *International Journal for Numerical Methods in Engineering*, Vol. 46, pp. 131 - 150
- Needleman, A., 1992, "Micromechanical Modeling of Interfacial Decohesion", *Ultramicroscopy*, Vol. 40, pp. 203 – 214
- Newman, J.C. & Dodds, R.H., 1997, "From Brittle to Elastic-Plastic Fracture Mechanics", *Fracture Research in Retrospective*, A.A. Balkema, pp. 265 - 282
- O'Dowd, N.P., and Shih, C.F., 1992, "Two-Parameter Fracture Mechanics: Theory and Applications", *ASTM 24th National Symposium on Fracture Mechanics*, Tennessee

- Panontin, T.L., Hill, M.R., 1996, "The Effect of Residual Stresses on Brittle and Ductile Fracture Initiation Predicted by Micromechanical Models", *International Journal of Fracture*, Vol. 82, pp. 317 – 33
- Panontin, T.L., Sheppard, S.D., 1995, "Relationship between Constraint and Ductile Fracture Initiation as Defined by Micromechanical Analysis", *ASTM STP 1256*, ASTM, pp. 54 – 85
- Peric, D.; Hochard, C.; Dutko, M.; Owen, D.R.J., 1996, "Transfer Operators for Evolving Meshes In Small Strain Elasto-Plasticity", *Computer Methods in Applied Mechanics and Engineering*, Vol. 137, pp. 331 - 344
- Rashid, M.M., 2002, "Material State Remapping in Computational Solid Mechanics", *International Journal of Numerical Methods in Engineering*, in press
- Rashid, M.M.; Roy R., 1999, "A New Theoretical Framework for Inelastic Fracture Processes", *Fatigue and Fracture Mechanics: Twenty-ninth Volume, ASTM STP 1332*, T. L. Panontin and S. D. Sheppard, Eds., American Society of Testing and Materials: West Conshohocken, PA, pp. 264 – 283
- Rashid, M.M., 1998, "The Arbitrary Local Mesh Replacement Method: An Alternative To Remeshing For Crack Propagation Analysis", *Computational Methods in Applied Mechanics and Engineering*, Vol. 154, pp. 133 - 50
- Rashid, M.M., 1997, "A New Theory For Free-Surface Formation in Solid Continua," *International Journal of Solids and Structures*, Vol. 34, pp. 2303 – 2320
- Rice, J.R., 1968, "A Path Independent integral and the Approximate Analysis of Strain Concentration by Notches and Cracks", *Journal of Applied Mechanics*, June, pp. 379 – 386
- Rossmannith, H.P., 1997, Editor, "The Struggle for Recognition of Engineering Fracture Mechanics", *Fracture Research in Retrospective*, A.A. Balkema, pp. 37 – 93
- Siegmund, T., Brocks, W., " A Numerical Study on the Correlation between the Work of Separation and the Dissipation Rate in Ductile Fracture", *Engineering Fracture Mechanics*, Vol. 67, pp. 139 – 154
- Reynolds Metal Company, 1965, *The Aluminum Data Book*, Reynolds Metal Company, Richmond, VA., pg. 31
- Thomason, P.F, 2000, "A Three Dimensional Model for Ductile Fracture by the Growth and Coalescence of Micro-Voids", *Acta Metallica*, Vol. 33, 1985, pp. 1087 – 1095
- Thomason, P.F., 1998, "A View on Ductile-Fracture Modeling", *Fatigue and Fracture of Engineering Materials and Structures*, Vol. 21, pp. 1105 – 1122

- Trädegård, A.; Nilsson, F., Östlund, S., 1998, "FEM-Remeshing Technique Applied to Crack Growth Problems", *Computer Methods in Applied Mechanics and Engineering*, Vol. 160, pp. 115 - 131
- Tvergaard, V., 1982 "Ductile Fracture by Cavity Nucleation between Larger Voids", *Journal of Mechanics and Physics of Solids*, Vol. 30, , pp. 265 – 286
- Tvergaard, V.; Needleman, A., 1984, "Analysis of the Cup-Cone Fracture in a Round Tensile Bar", *Acta Metallica*, Vol. 32., pp. 157 - 169
- Wawrzynek, P.A.; Ingraffea, A.R., 1989, "An Interactive Approach to Local Remeshing Around a Propagating Crack", *Finite Element in Analysis and Design*, Vol. 5, pp. 87 - 96
- Westergaard, H.M., 1939, "Bearing Pressures and Cracks", *Trans. ASME*, Vol. 61, pp. A-49 – A-53
- Wilsius, J.; Imad, A.; Nait Abdelaziz, M.; Mesmacque, G.; Eripret, C., 2000, "Void Growth and Damage Models for Predicting Ductile Fracture in Welds", *Fatigue and Fracture of Engineering Materials and Structures*, Vol. 23, pp. 105 - 112
- Xia, L.; Shih, C.F., 1996, "Ductile Crack Growth – III. Transition to Cleavage Incorporating Statistics", *Journal of Mechanics and Physics of Solids*, Vol. 44, No. 4, pp. 603 - 639
- Xia, L.; Shih, C.F., 1995a, "Ductile Crack Growth – I. A Numerical Study Using Computational Cells with Microstructurally-Based Length Scales", *Journal of Mechanics and Physics of Solids*, Vol. 43, No. 2, pp. 233 - 259
- Xia, L.; Shih, C.F., 1995b, "Ductile Crack Growth – II. Void Nucleation and Geometry Effects on Macroscopic Fracture Behavior", *Journal of Mechanics and Physics of Solids*, Vol. 43, No. 12, pp. 1953 – 1981
- Zhang, K.S.; Bai, J.B.; Francois, D., 1999, "Ductile Fracture of Materials with High Void Volume Fraction", *International Journal of Solids and Structures*, Vol. 36, pp. 3407 - 3425

Appendix A – Load vs. CMOD Curves

Figure A.1 – Aluminum 2024, SYM test	103
Figure A.2 – Aluminum 2024, SYMA test	103
Figure A.3 – Aluminum 2024, A-18 test.....	104
Figure A.4 – Aluminum 2024, B-18 test.....	104
Figure A.5 – Aluminum 2024, C-18 test.....	105
Figure A.6 – Aluminum 2024, D-18 test.....	105
Figure A.7 – Inconel 718 with $\Phi_c = 0.075$, $c_o = 19.61$ mm	106
Figure A.8 – Inconel 718 with $\Phi_c = 0.080$, $c_o = 19.61$ mm	106
Figure A.9 – Inconel 718 with $\Phi_c = 0.085$, $c_o = 19.61$ mm	107
Figure A.10 – Inconel 718 with $a = 0.0254$ mm, $c_o = 19.61$ mm	107
Figure A.11 – Inconel 718 with $a = 0.0508$ mm, $c_o = 19.61$ mm	108
Figure A.12 – Inconel 718 with $a = 0.0635$ mm, $c_o = 19.61$ mm	108
Figure A.13 – Inconel 718 c_o comparison, with $a = 0.0635$ mm & $\Phi_c = 0.065$.....	109
Figure A.14 – Inconel 718 c_o comparison, with $a = 0.0508$ mm& $\Phi_c = 0.07$.....	109
Figure A.15 – Inconel 718 c_o comparison, with $a = 0.0381$ mm & $\Phi_c = 0.08$.....	110
Figure A.16 – Inconel 718 c_o comparison, with $a = 0.0254$ mm & $\Phi_c = 0.085$.....	110

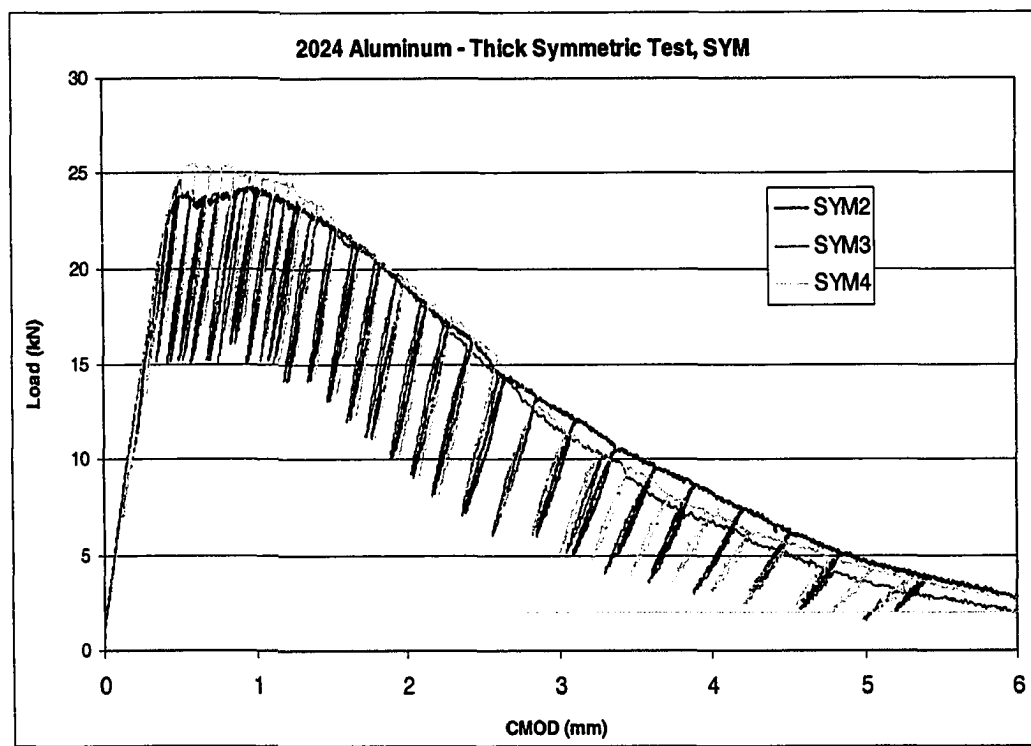


Figure A.1: Aluminum 2024 – SYM test. Symmetric test of standard thickness with crosshead and rollers in symmetric configuration.

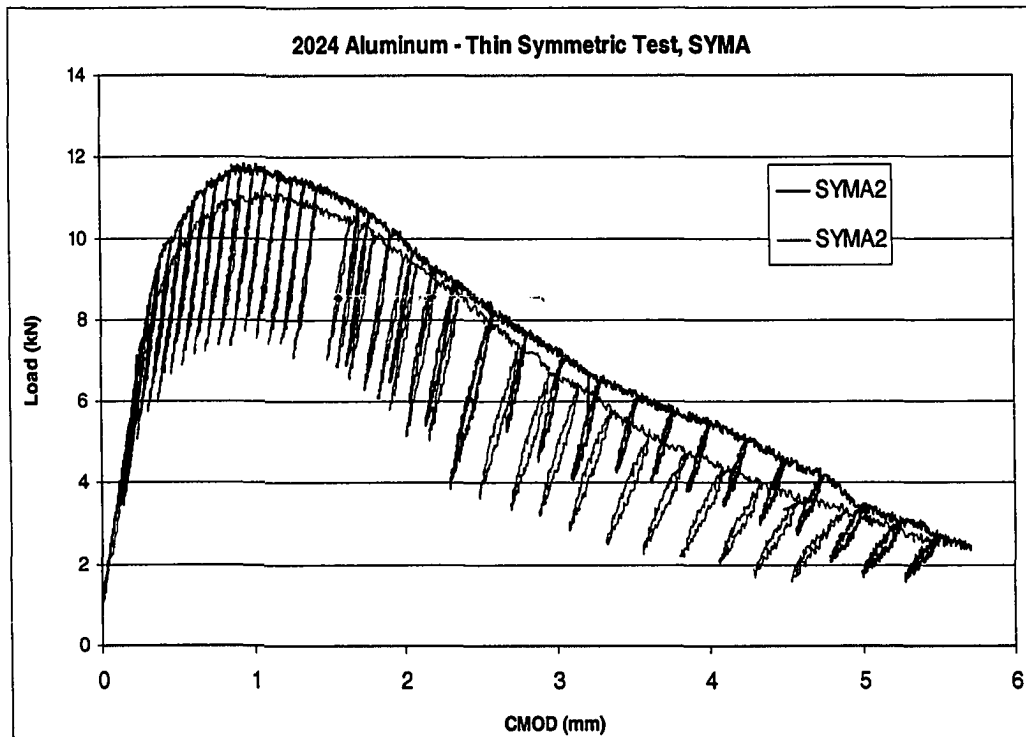


Figure A.2: Aluminum 2024 – SYMA test. Symmetric test of thin specimen with crosshead and rollers in symmetric configuration.

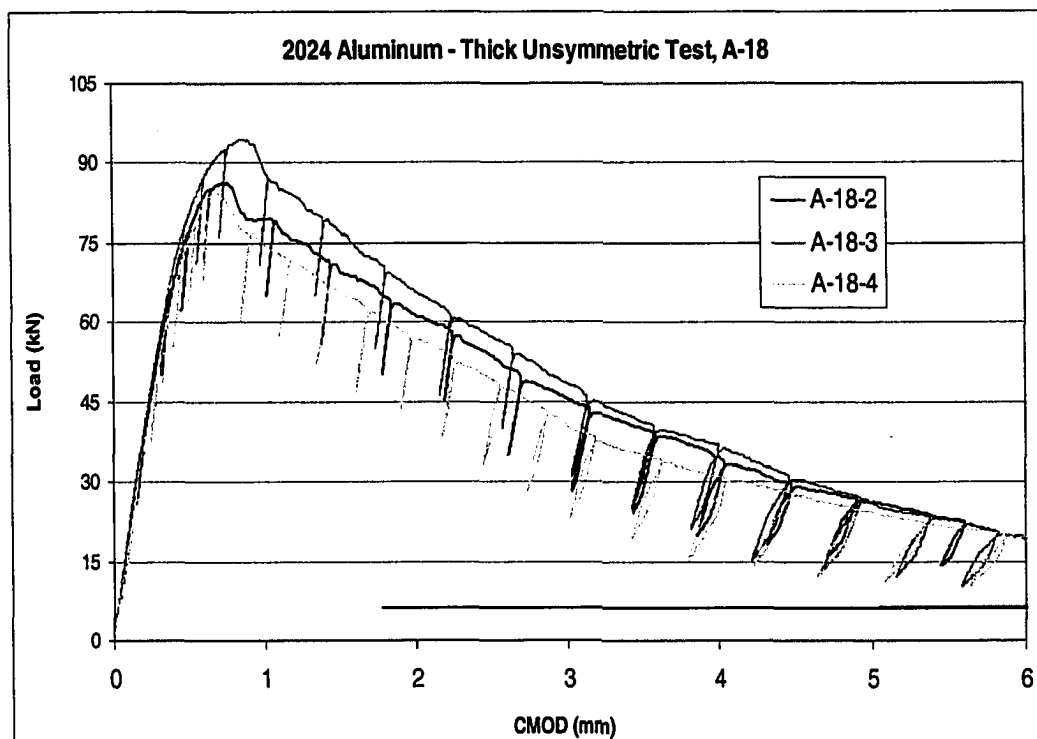


Figure A.3: Aluminum 2024 – A-18 test. Unsymmetric test of standard thickness with load at $c = 18\text{mm}$ and right roller at $b = 20\text{ mm}$ (Table 3.1)

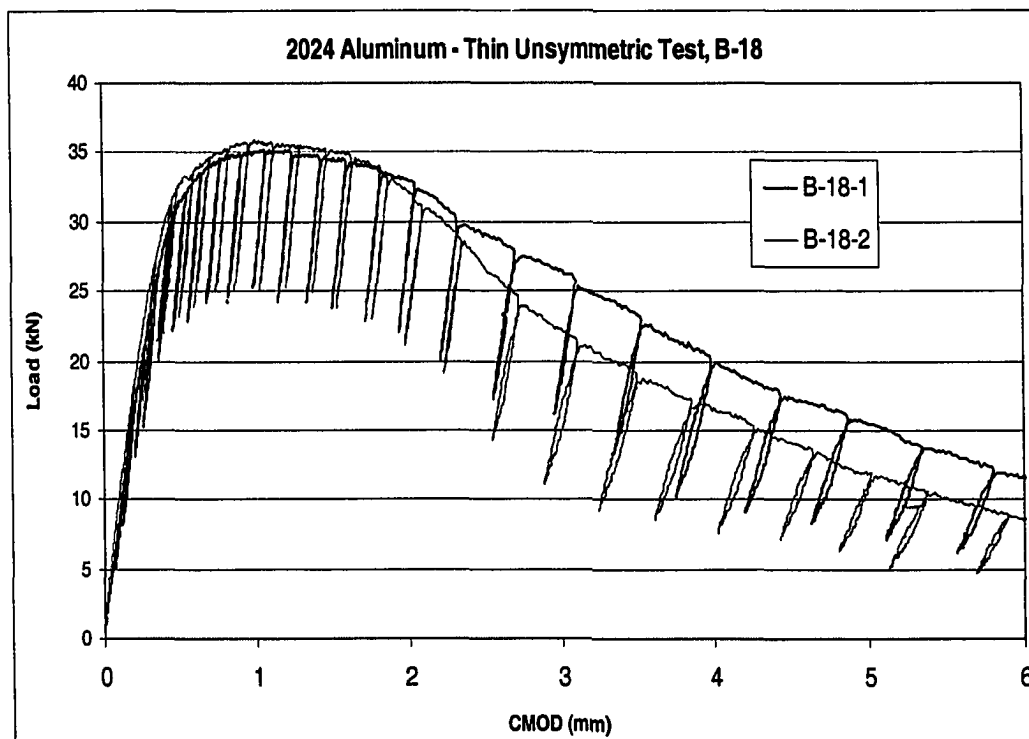


Figure A.4: Aluminum 2024 – B-18 test. Unsymmetric test of thin specimen with load at $c = 18\text{mm}$ and right roller at $b = 20\text{ mm}$ (Table 3.1)

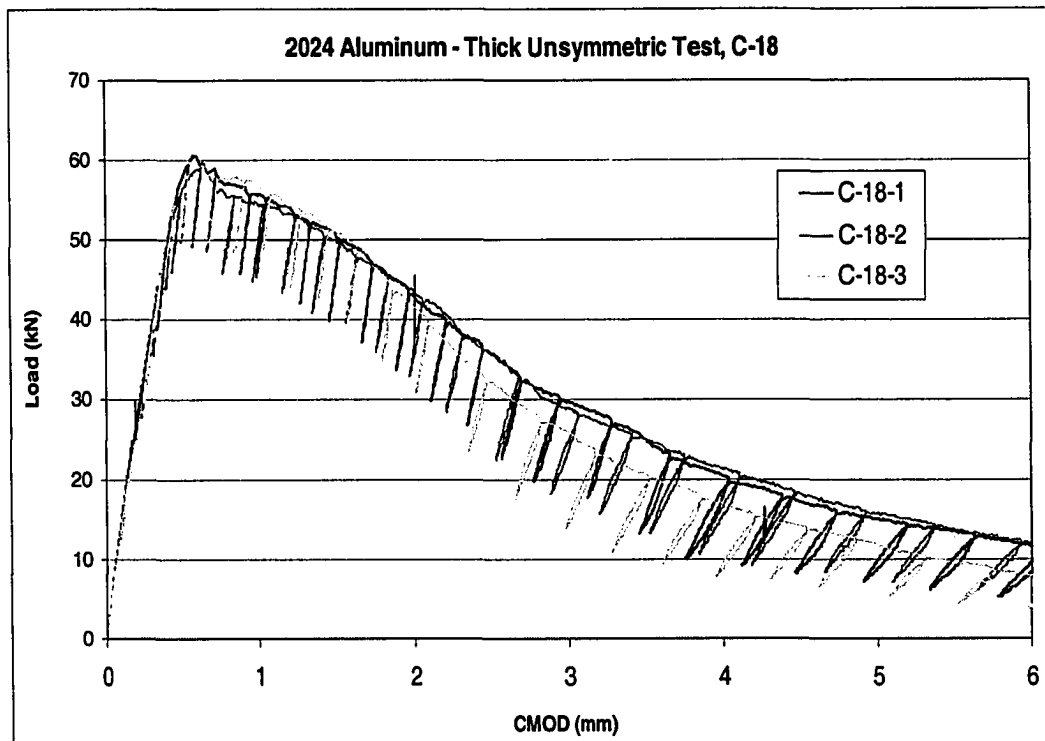


Figure A.5: Aluminum 2024 – C-18 test. Unsymmetric test of standard thickness with load at $c = 18\text{mm}$ and right roller at $b = 30\text{ mm}$ (Table 3.1)

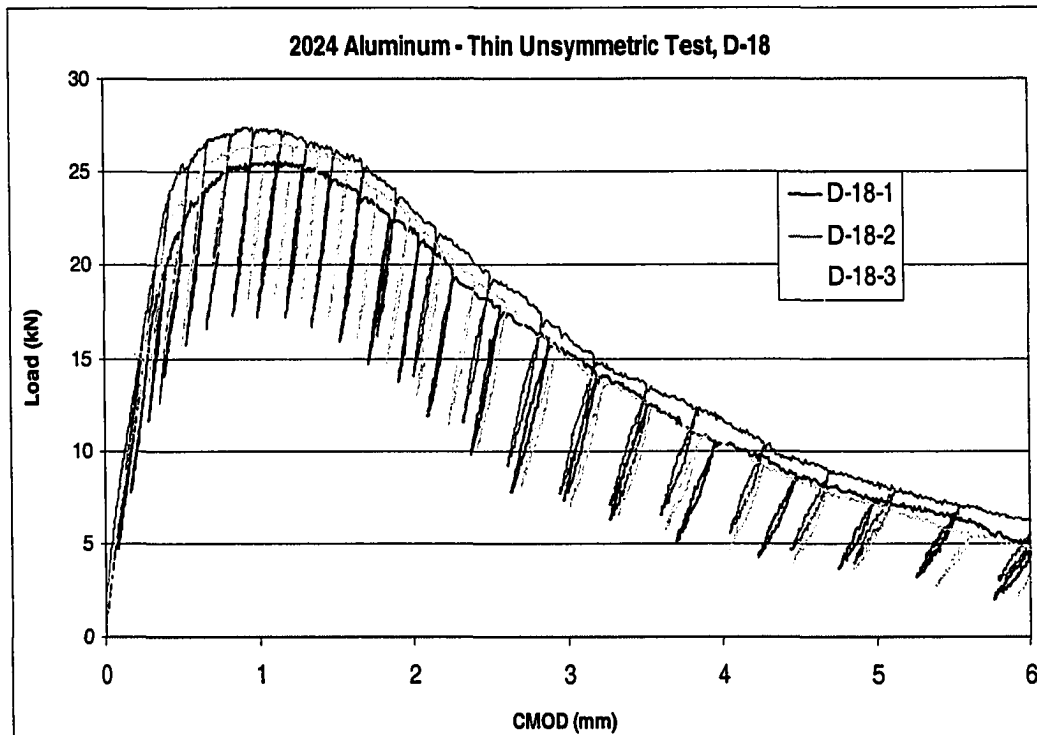


Figure A.6: Aluminum 2024 – D-18 test. Unsymmetric test of thin specimen with load at $c = 18\text{mm}$ and right roller at $b = 30\text{ mm}$ (Table 3.1)

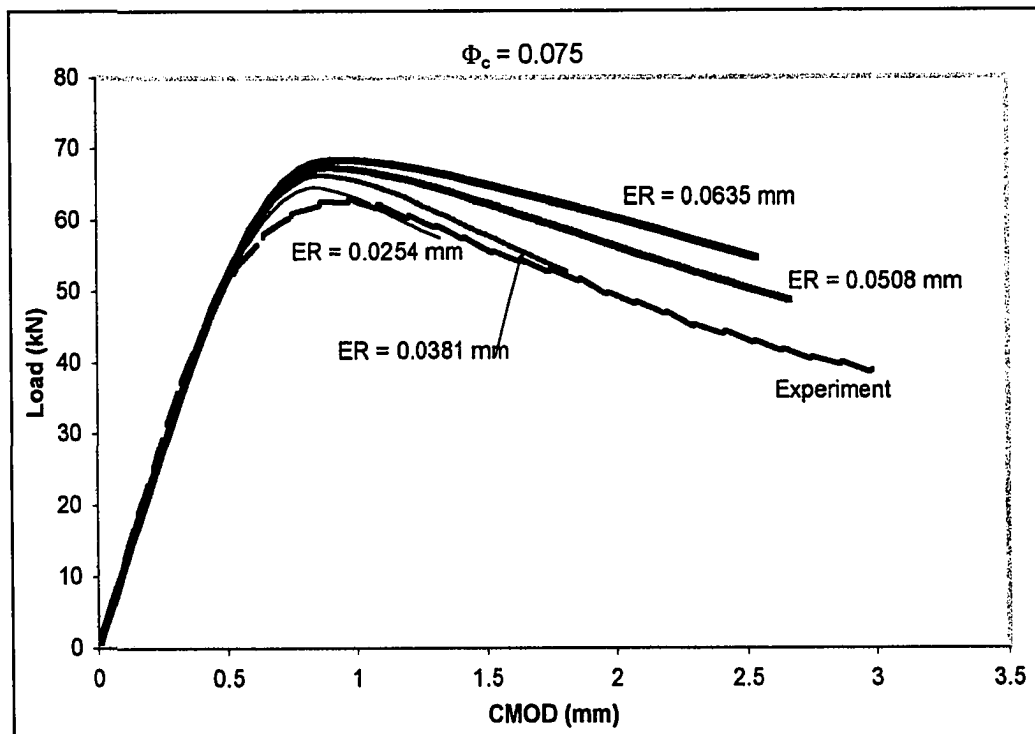


Figure A.7: Inconel 718 with $c_o = 19.61$ mm. Load versus CMOD comparisons with $\Phi_c = 0.075$ and $a = 0.0254$ mm, 0.0381 mm, 0.0508 mm, and 0.0635 mm

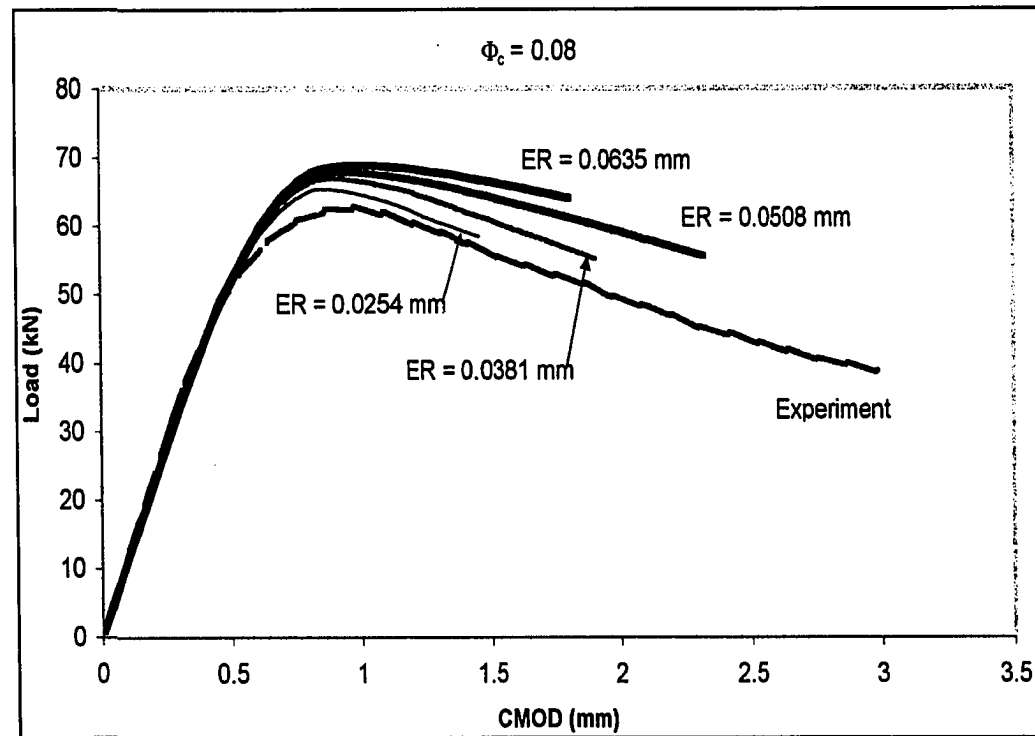


Figure A.8: Inconel 718 with $c_o = 19.61$ mm. Load versus CMOD comparisons with $\Phi_c = 0.08$ and $a = 0.0254$ mm, 0.0381 mm, 0.0508 mm, and 0.0635 mm

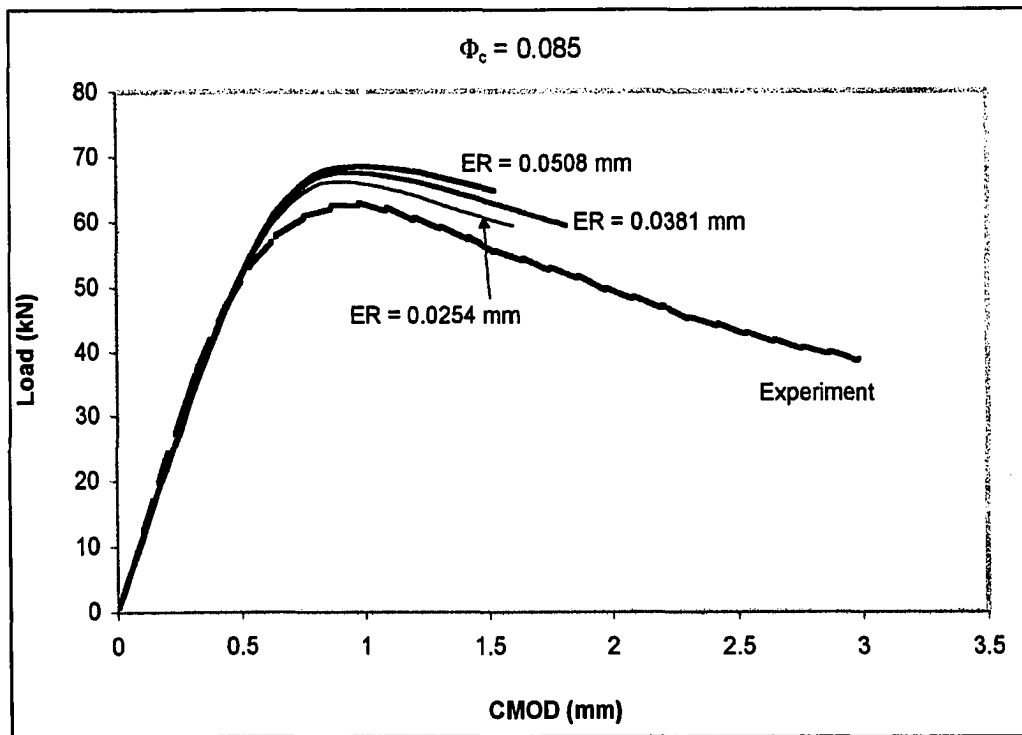


Figure A.9: Inconel 718 with $c_o = 19.61$ mm. Load versus CMOD comparisons with $\Phi_c = 0.085$ and $a = 0.0254$ mm, 0.0381 mm and 0.0508 mm

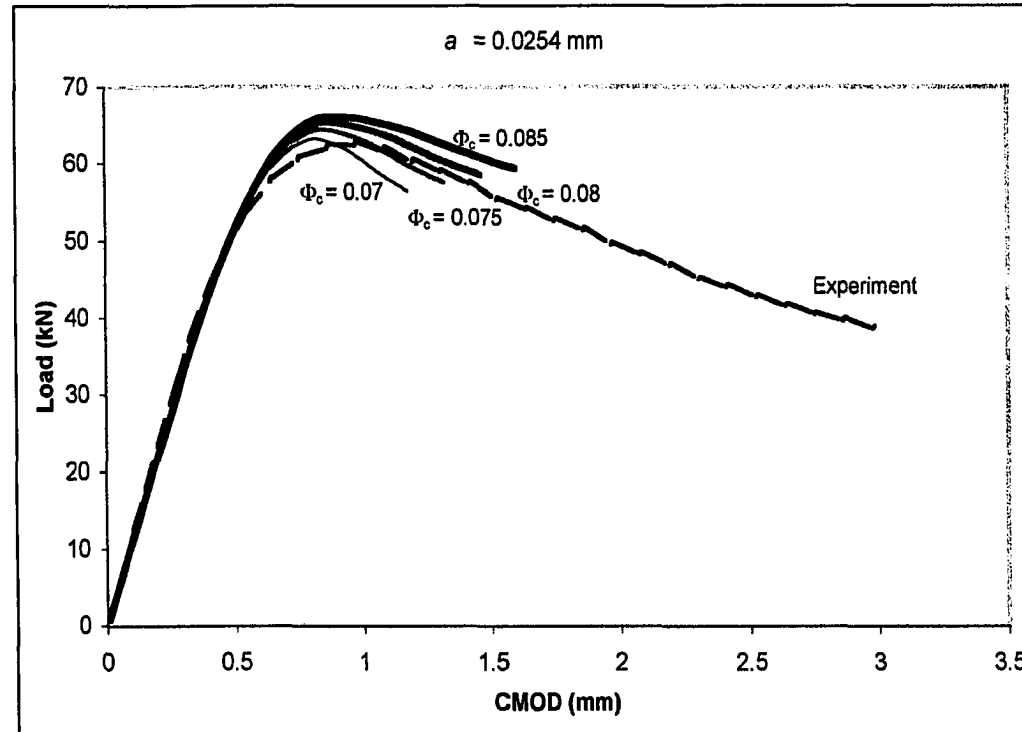


Figure A.10: Inconel 718 with $c_o = 19.61$ mm. Load versus CMOD comparisons with $a = 0.0254$ mm and $\Phi_c = 0.07$, 0.075, 0.08, and 0.085

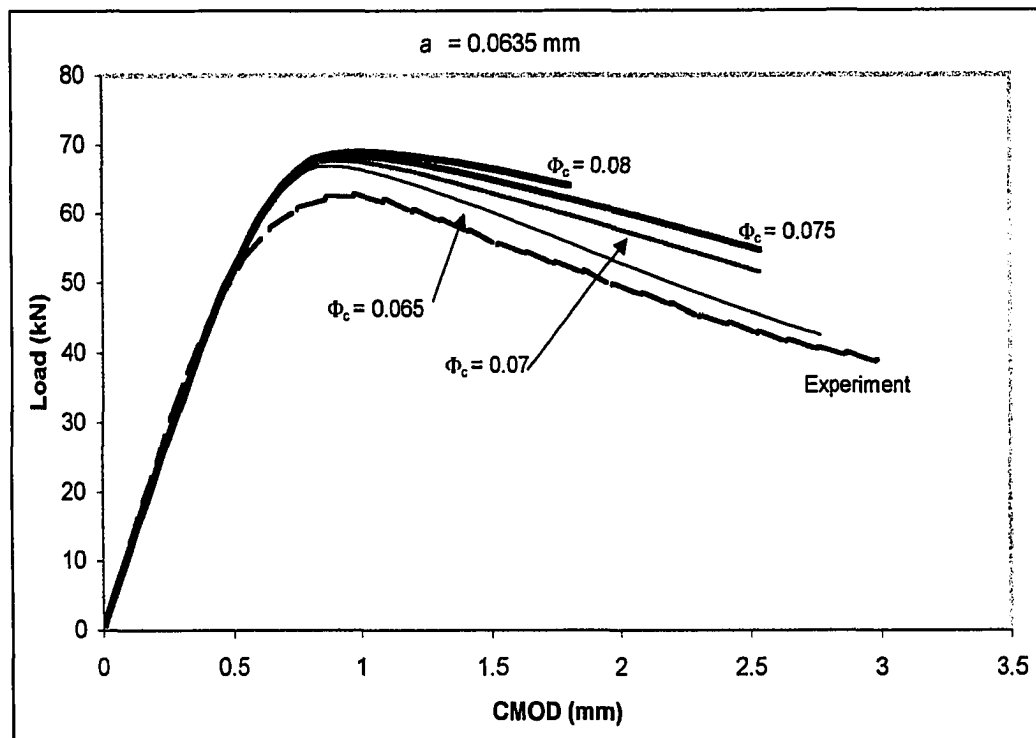


Figure A.11: Inconel 718 with $c_o = 19.61 \text{ mm}$. Load versus CMOD comparisons with $a = 0.0508 \text{ mm}$ and $\Phi_c = 0.07, 0.075, 0.08$, and 0.085

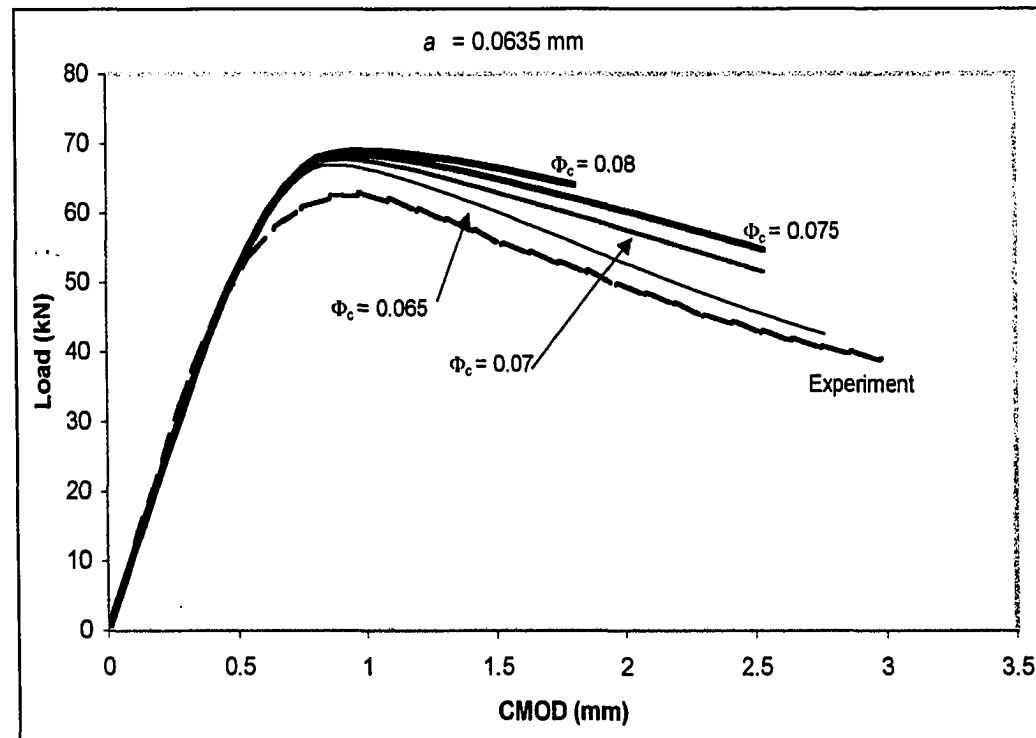


Figure A.12: Inconel 718 with $c_o = 19.61 \text{ mm}$. Load versus CMOD comparisons with $a = 0.0635 \text{ mm}$ and $\Phi_c = 0.065, 0.07, 0.075$, and 0.08

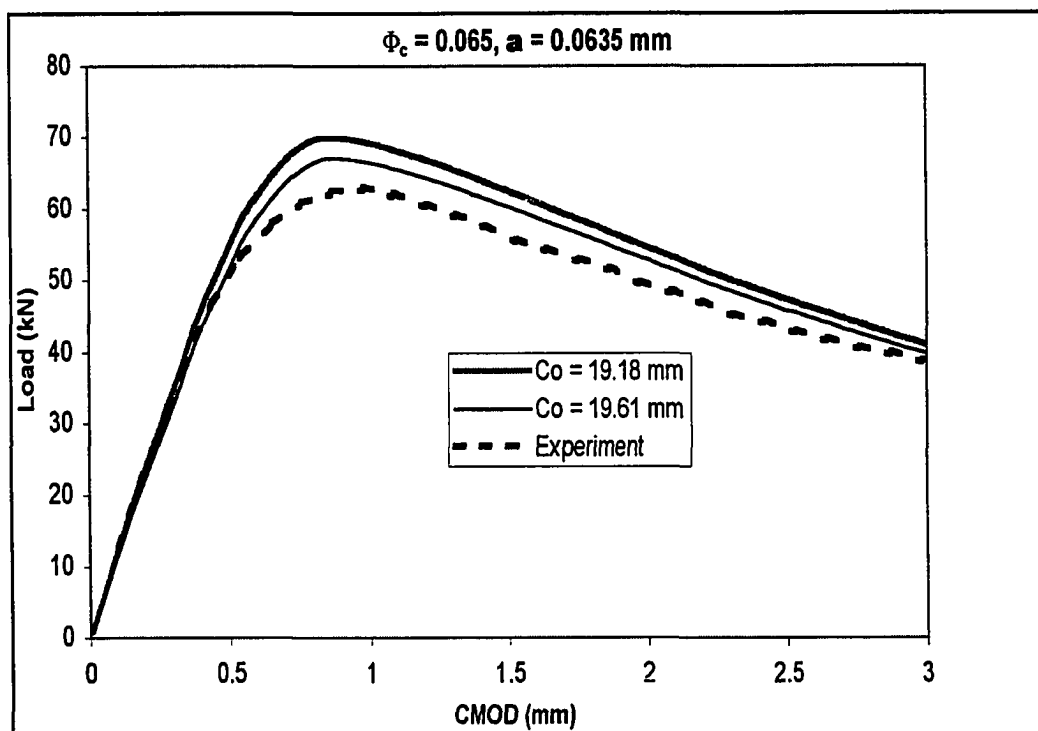


Figure A.13: Inconel 718 with $\Phi_c = 0.065$ and $a = 0.0635 \text{ mm}$. Load versus CMOD comparisons for $c_0 = 19.18 \text{ mm}$ and $c_0 = 19.61 \text{ mm}$

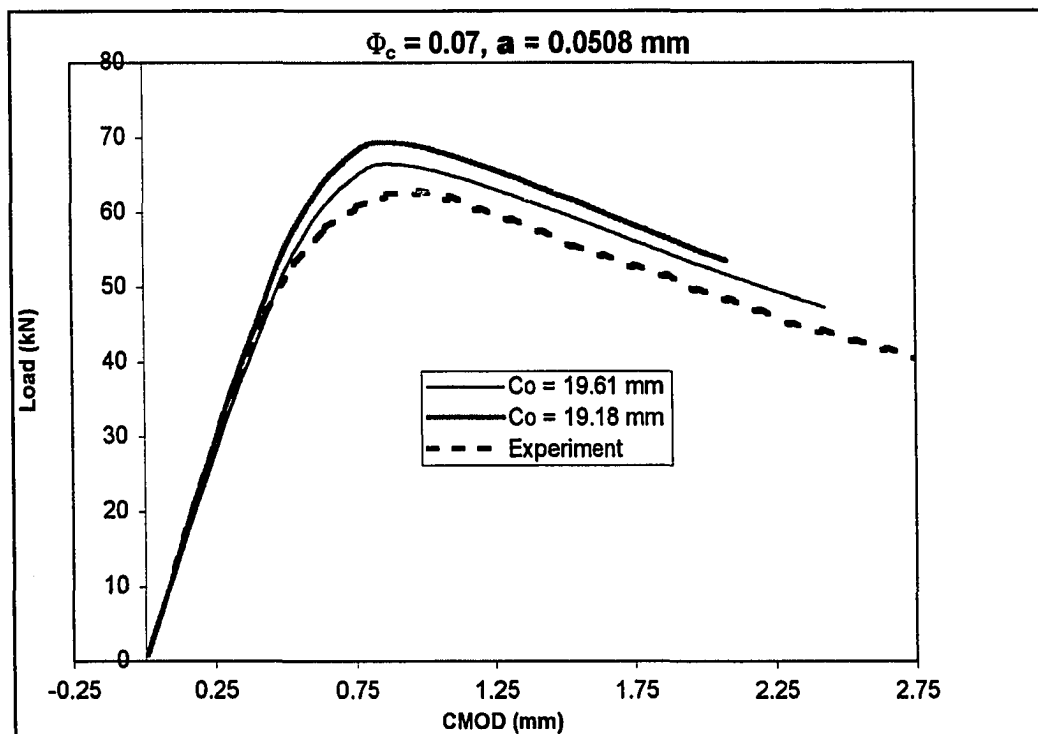


Figure A.14: Inconel 718 with $\Phi_c = 0.07$ and $a = 0.0508 \text{ mm}$. Load versus CMOD comparisons for $c_0 = 19.18 \text{ mm}$ and $c_0 = 19.61 \text{ mm}$

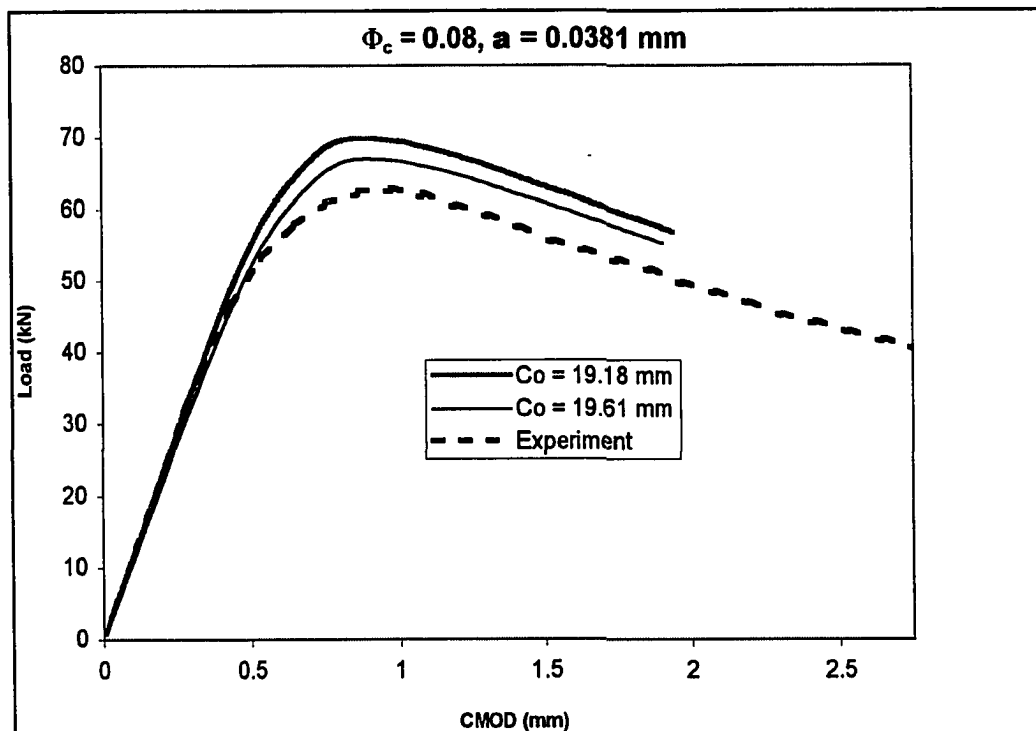


Figure A.15: Inconel 718 with $\Phi_c = 0.08$ and $a = 0.0381 \text{ mm}$. Load versus CMOD comparisons for $c_0 = 19.18 \text{ mm}$ and $c_0 = 19.61 \text{ mm}$

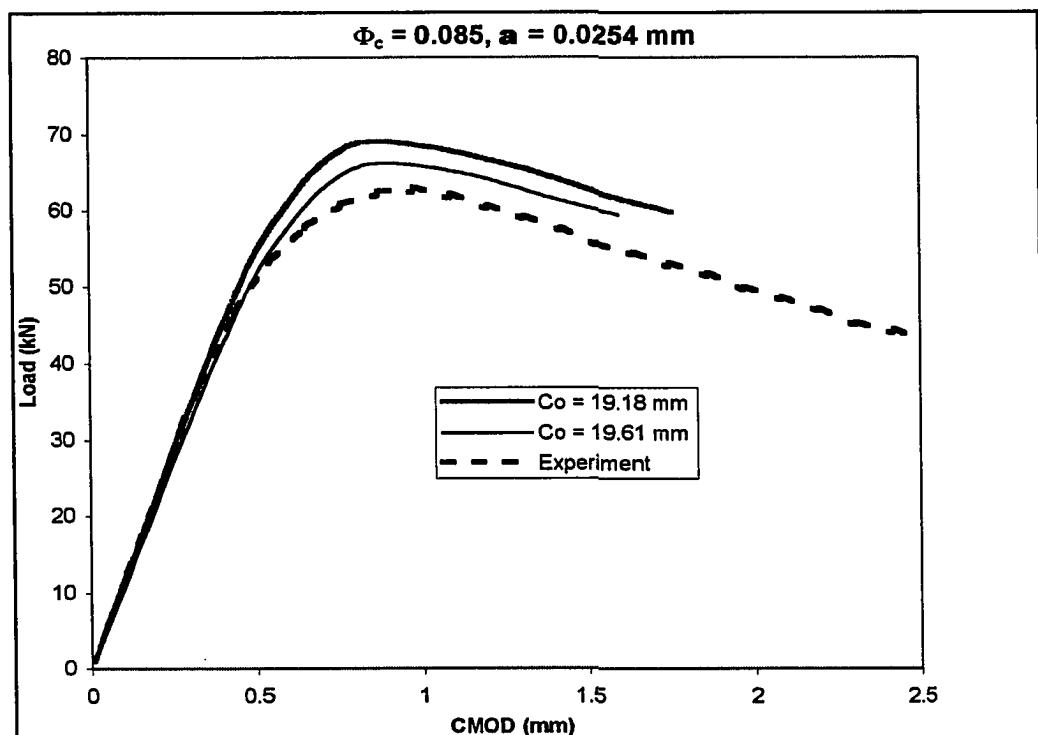


Figure A.16: Inconel 718 with $\Phi_c = 0.085$ and $a = 0.0254 \text{ mm}$. Load versus CMOD comparisons for $c_0 = 19.18 \text{ mm}$ and $c_0 = 19.61 \text{ mm}$

Appendix B – Supplemental Aluminum 2024

Material Information

Figure B.1 – Aluminum 2024, Material Data Sheet.....112

Figure B.2 – Aluminum 2024, SEM Electron Backscatter Plot.....113

PAGE: 1	TRFC	INCLUSION	SERIAL NUMBER 0049-5945
SOLD TO AFFILIATED METALS INC 2895 SOUTH 300 WEST P.O. BOX 65529 SALT LAKE CITY UT 84115	KAI SER ALUMINUM CERTIFIED TEST REPORT TRENTWOOD WORKS - SPOKANE, WASHINGTON		
SHIP TO AFFILIATED METALS INC 2895 SOUTH 300 WEST P.O. BOX 65529 SALT LAKE CITY UT 84115	MATERIAL AFFILIATED METALS INC 2895 SOUTH 300 WEST P.O. BOX 65529 SALT LAKE CITY UT 84115		
CUSTOMER PURCHASE ORDER NO & ITEM 114959 KAI SER ORDER NO 2024 00 T351 052-813881 ITEM NUMBER 727-8740 PAK NUMBER WEIGHT SHIPPED NO OF PCKG'S 3,632 4 GOVT CONTRACT NO 227211 09-20-93 CUSTOMER SPECIFICATION QQA 25014 REV E AM 2 AMS 4037 REV M AM ASTM B 209 REV92 AM BAC 5439 REV H MIL-STD-2154 TEST CODE 1504C1 TEST RESULTS LOT: 376433 TENSILE: TEMPER DIR/TESTS T351 LT 02 (MIN/MAX) ULTIMATE KSI 66.0 : 66.2 YIELD KSI 44.6 : 46.6 ELONGATION % IN 2" LOT: 390961 TENSILE: TEMPER DIR/TESTS T351 LT 02 (MIN/MAX) ULTIMATE KSI 65.7 : 66.0 YIELD KSI 45.6 : 46.1 ELONGATION % IN 2" METAL COMPLIES WITH ULTRASONIC TESTING REQUIREMENTS OF DPS 4.713 GRADE A REQUIREMENT, AND PS 21211, GSS 16100, ASTM B594, BAC 5439, MIL-I-8950, AND MIL-STD-2154 CLASS A REQUIREMENTS. CHEMISTRY: 2024 MIN Si Fe Cu Mn Mg Cr Zn II V Zr OTHER MAX 0.50 0.50 3.80 0.30 1.20 0.10 0.25 0.15 0.05 ALUMINUM REMAINDER TOT 0.15 -- END OF REPORT -- PLEASE REFER QUESTIONS TO YOUR KAISER-TRENTWOOD SALES REPRESENTATIVE OR CALL 1-800-367-2586.			

Figure B.1: Material Data sheet for 2024 Aluminum as provided by supplier.

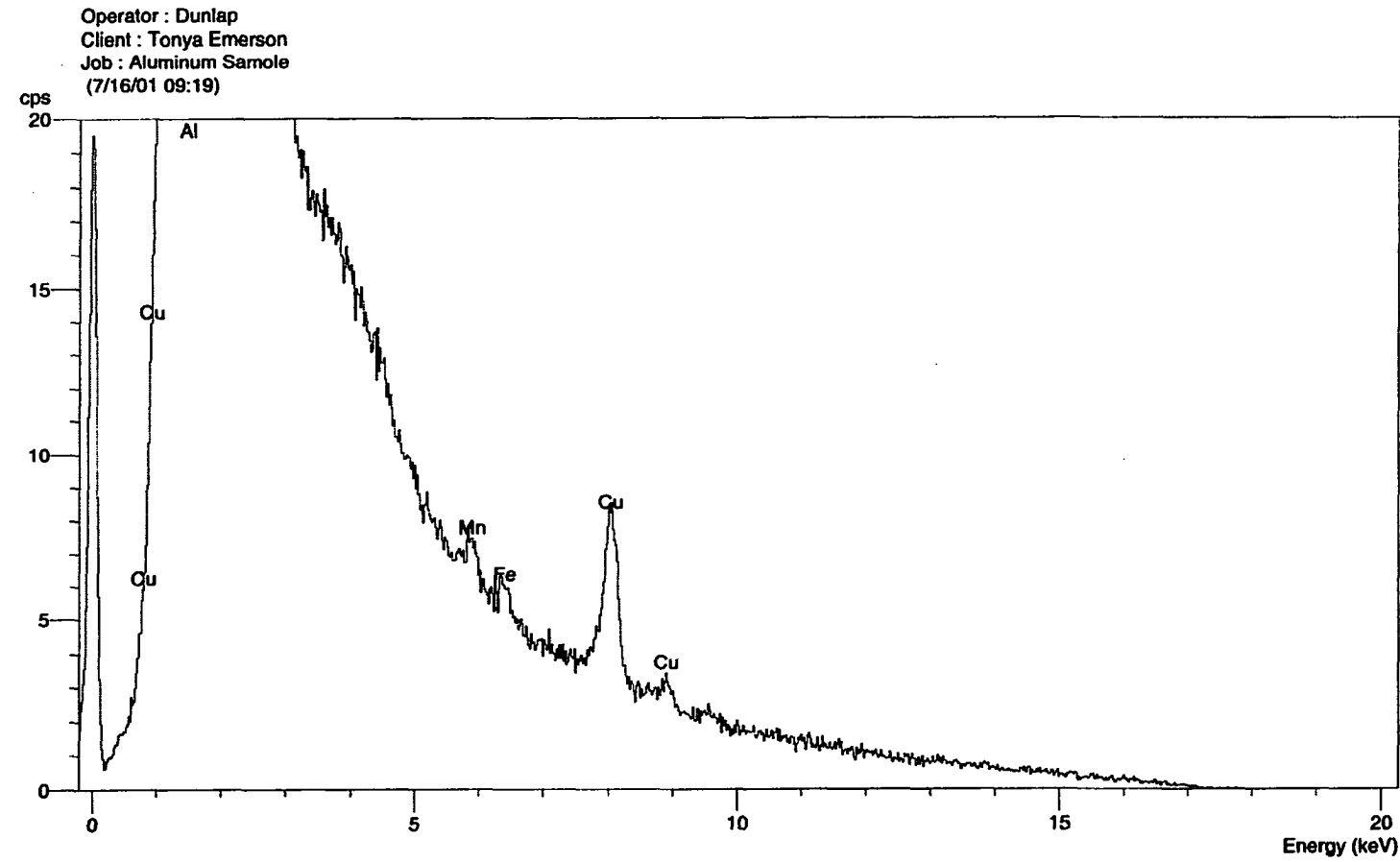


Figure B.1: Chemical composition of 2024 Aluminum per Scanning Electron Microscope, SEM, electron backscatter analysis.

Appendix C – Aluminum 2024 Fracture Specimen Photographs

Figure C.1 – A typical SYM fracture specimen.....	115
Figure C.2 – Typical crack path angle of A-18 specimens.....	115
Figure C.3 – Typical crack path angle of C-18 specimens	115
Figure C.4 – A typical SYMA thin fracture specimen.....	116
Figure C.5 – Typical B-18 thin specimen.....	116
Figure C.6 – Typical C-18 thin specimen.....	116

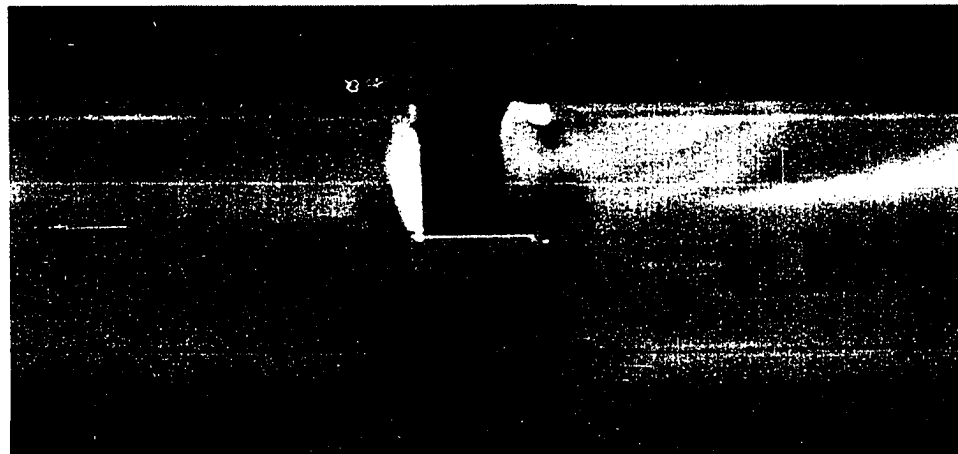


Figure C.1: Typical SYM fracture specimen. Self-similar fracture surface is visible on left half, while the right half clearly shows the depth of the shear lips.

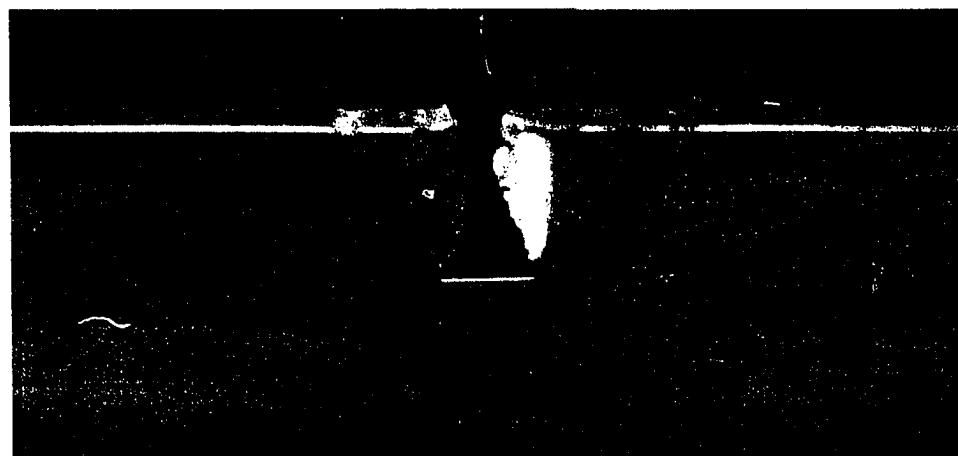


Figure C.2: Typical crack path angle of A-18 specimens. The angled crack path is visible on the right half of the specimen while the shear lips obscure the crack path on the left half.

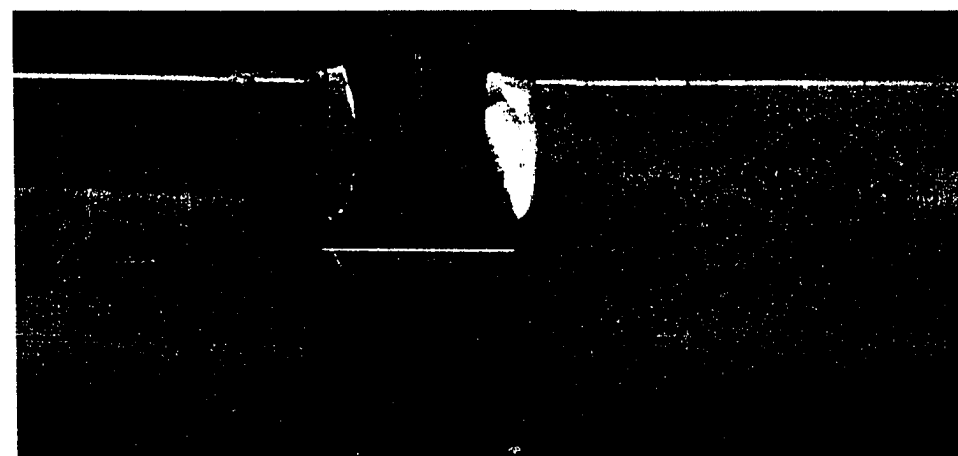


Figure C.3: Typical crack path angle of C-18 specimens. The angled crack path is visible on the right half of the specimen while the shear lips obscure the crack path on the left half.

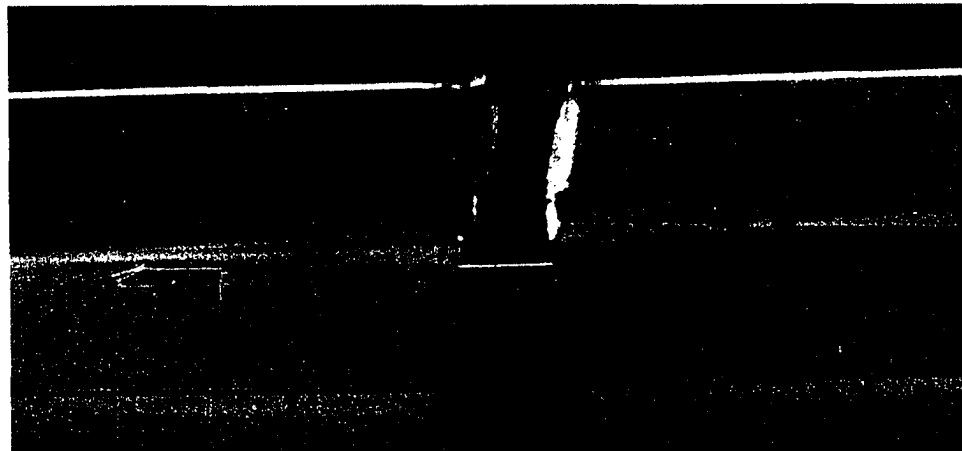


Figure C.4: Typical SYMA thin fracture specimen. The 45 degree shear lips that extend through the crack surface obscure self-similar fracture surface.



Figure C.5: Typical B-18 thin fracture specimen. The 45 degree shear lips that extend through the crack surface significantly alter the appearance of the crack path. Dashed line shows what appears to be the crack path.

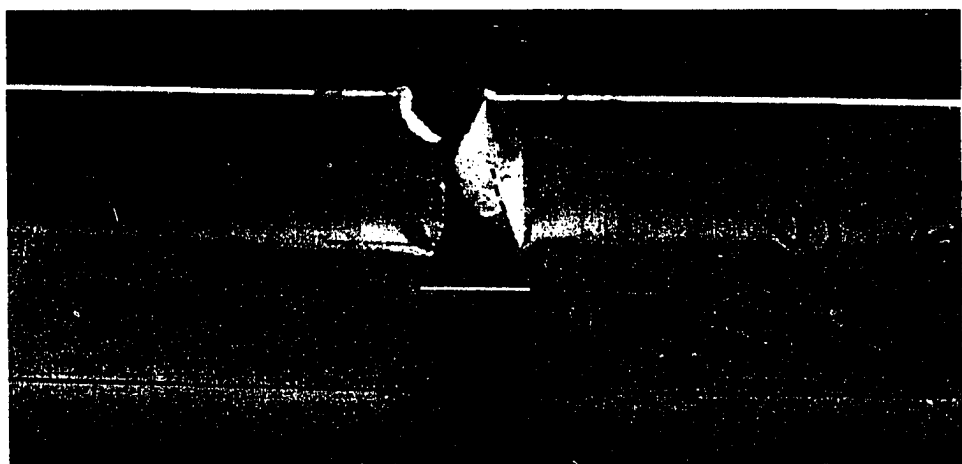
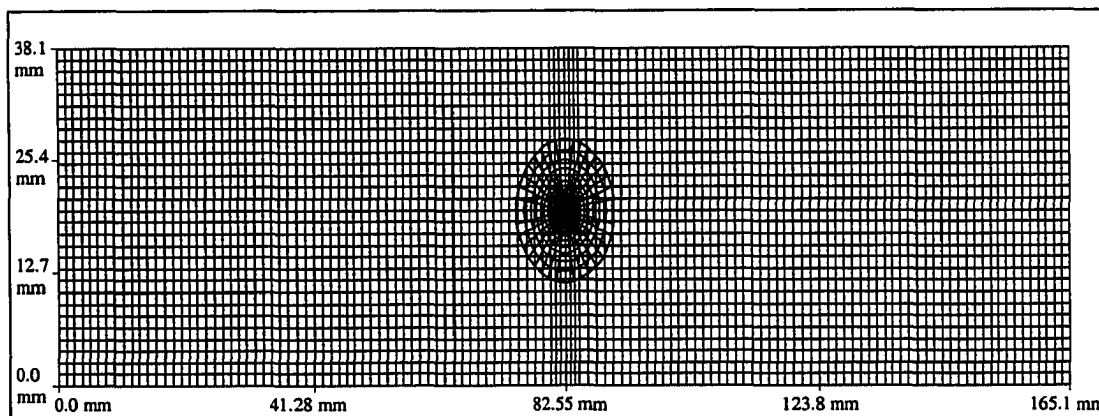


Figure C.6: Typical D-18 thin specimens. The 45 degree shear lips that extend through the crack surface significantly alter the appearance of the crack path. Dashed line shows apparent crack path.

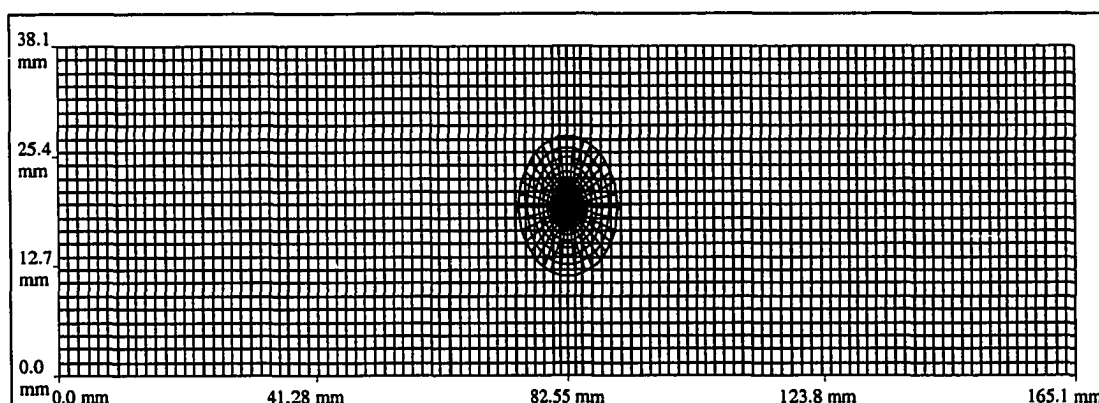
Appendix D – Inconel 718, Comparison of Mesh Size

Figure D.1 – Comparison of fine, standard and coarse meshes for Inconel 718 finite element mesh refinement verification.....118



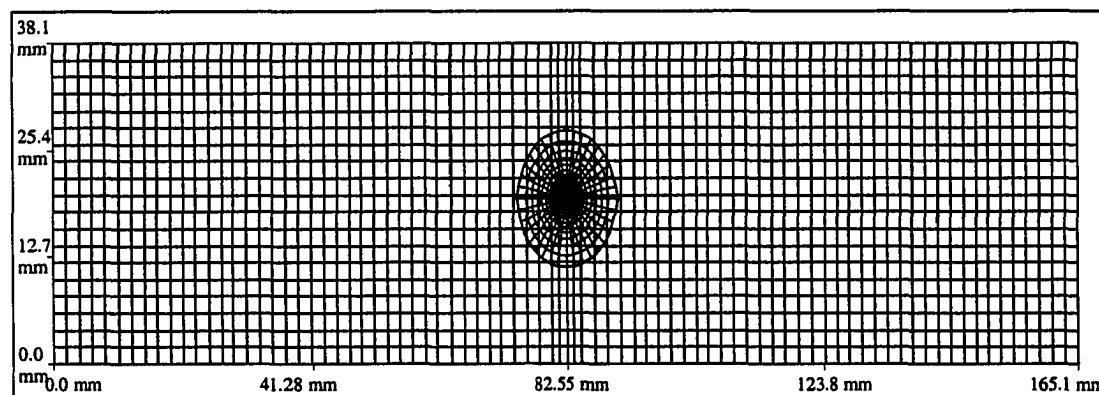
Fine Mesh: Background and patch mesh for Inconel 718 finite element model with 4224 nodes and 4389 elements.

(a)



Standard Mesh: Background and patch mesh for Inconel 718 finite element model with 2834 nodes and 2700 elements.

(b)



Coarse Mesh: Background and patch mesh for Inconel 718 finite element model with 1660 nodes and 1558 elements.

(c)

Figure D.1: Comparison of fine, standard and coarse meshes for Inconel 718 finite element mesh refinement verification.